Chapter 2
Figures

98Φ917Φ111
Part 2

Climate

- *Three discrete climate states*
  - *Dry (present day)*
  - *Long-term average*
  - *Superpluvial*
- *Modern-day analog defined for each*

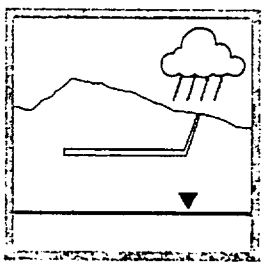

Outputs

- Paleoclimate data
- Paleospring elevations
- Regional-scale saturated zone model

odel Confidence Foundati

Infiltration (unsaturated zone flow subcomponent)
- Precipitation rates for future climates

Mountain-Scale Flow (unsaturated zone flow subcomponent)
- Water table elevation for future climates

Saturated Zone Flow and Transport
- Saturated zone groundwater flux for future climates

Biosphere
- Precipitation rates for future climates

Total System
- Climate-state durations

snFlow abq 42 eps

Figure 2-1. Coupling of the climate subcomponent to other UZ-flow subcomponents and to other TSPA-VA components.

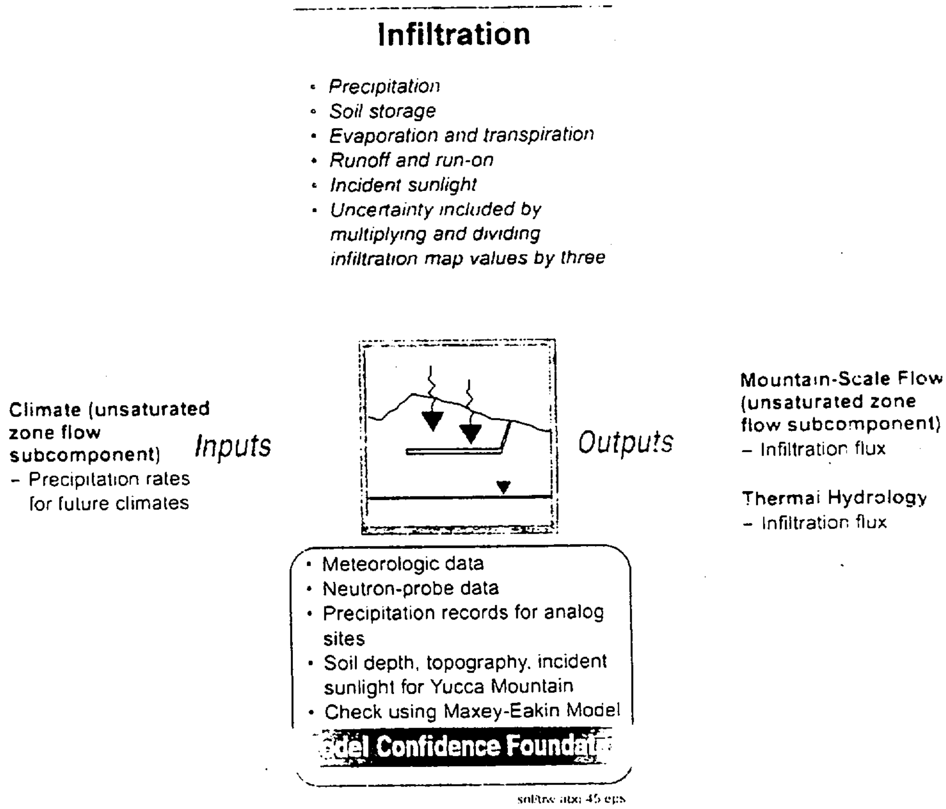

Figure 2-2. Coupling of the infiltration subcomponent to other UZ-flow subcomponents and to other TSPA-VA components.

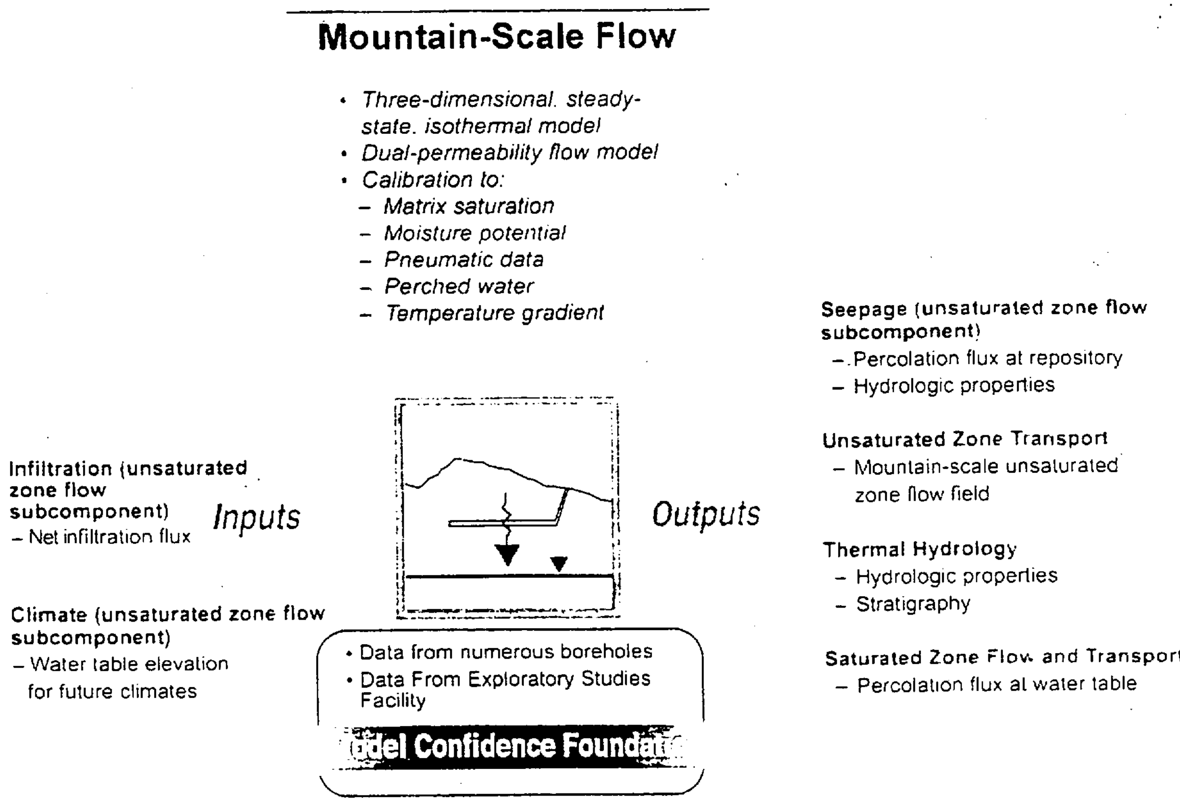

Figure 2-3. Coupling of the mountain-scale UZ-flow subcomponent to other UZ-flow subcomponents and to other TSPA-VA components.

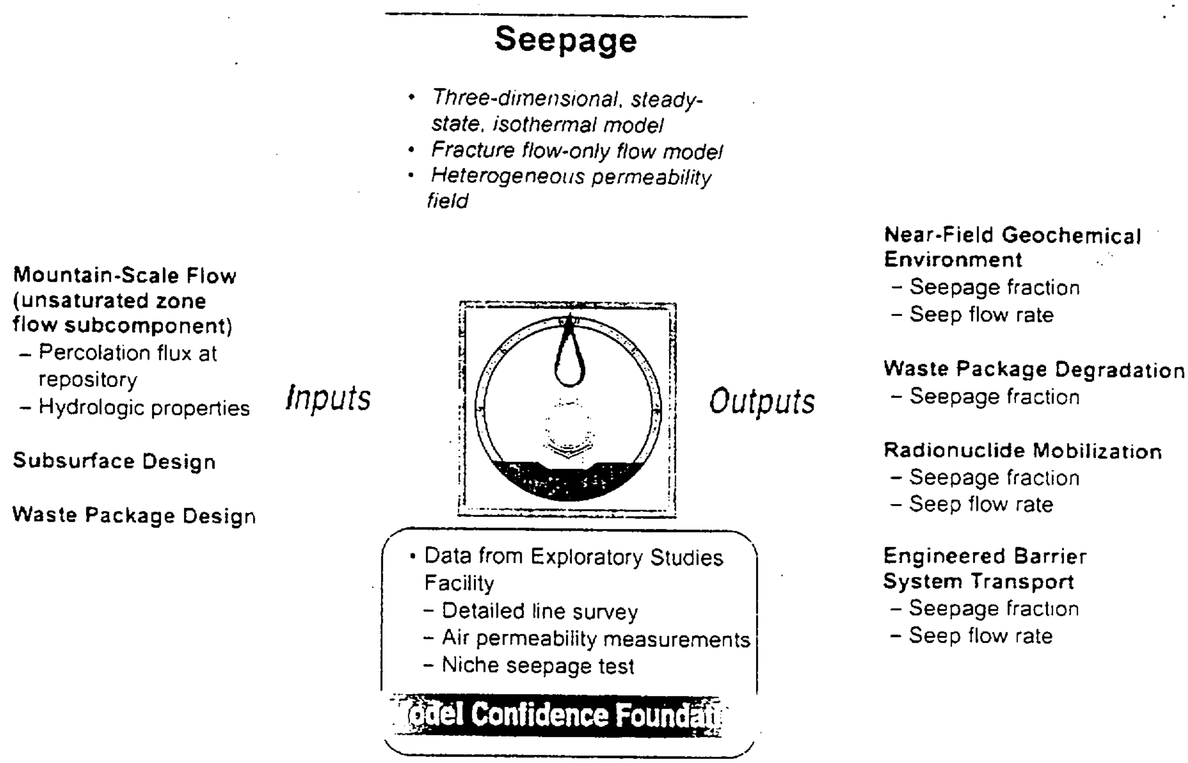

Figure 2-4. Coupling of the seepage subcomponent to other UZ-flow subcomponents and to other TSPA-VA components.

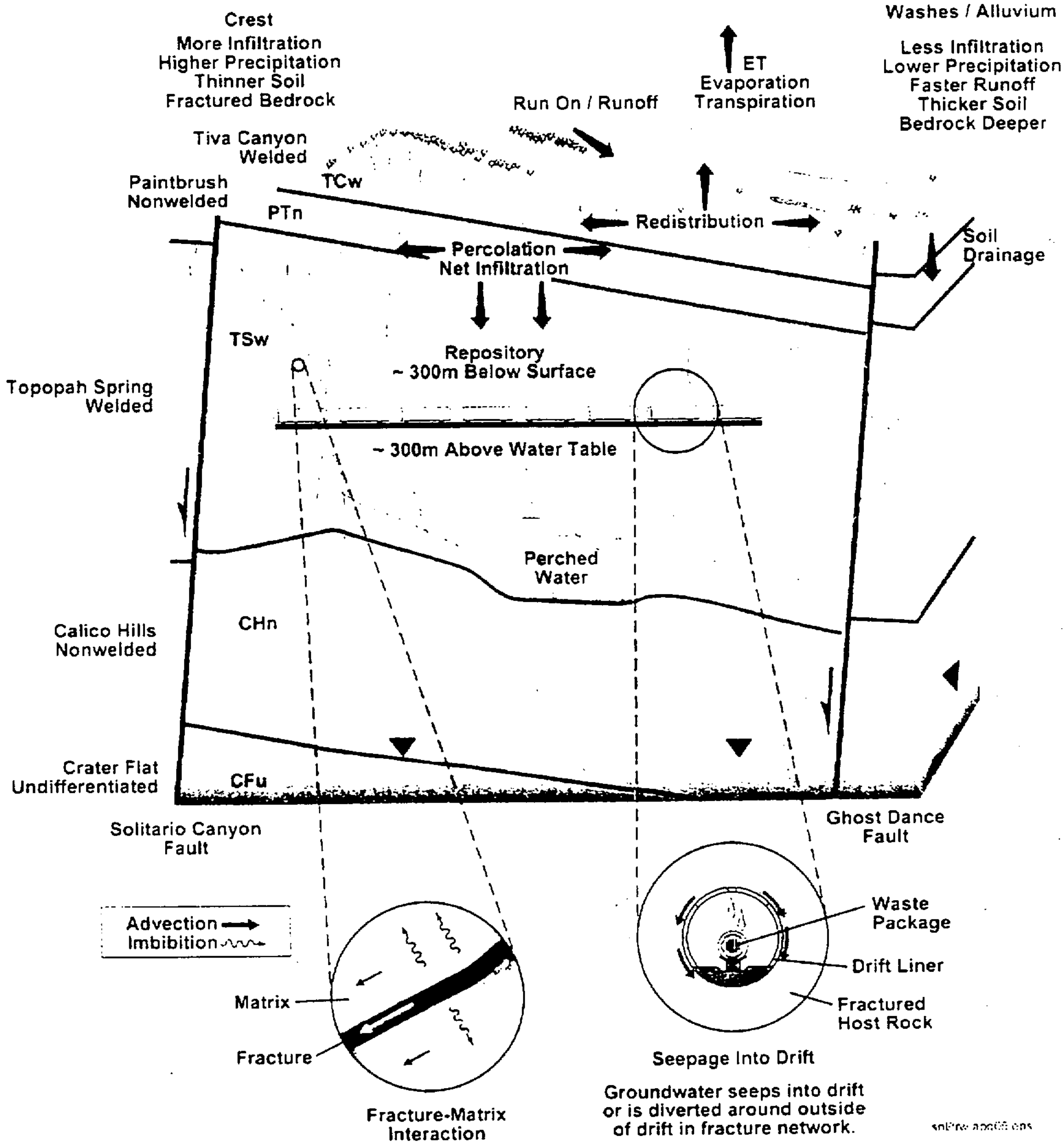

Figure 2-5. Conceptual models of processes associated with components of UZ flow.

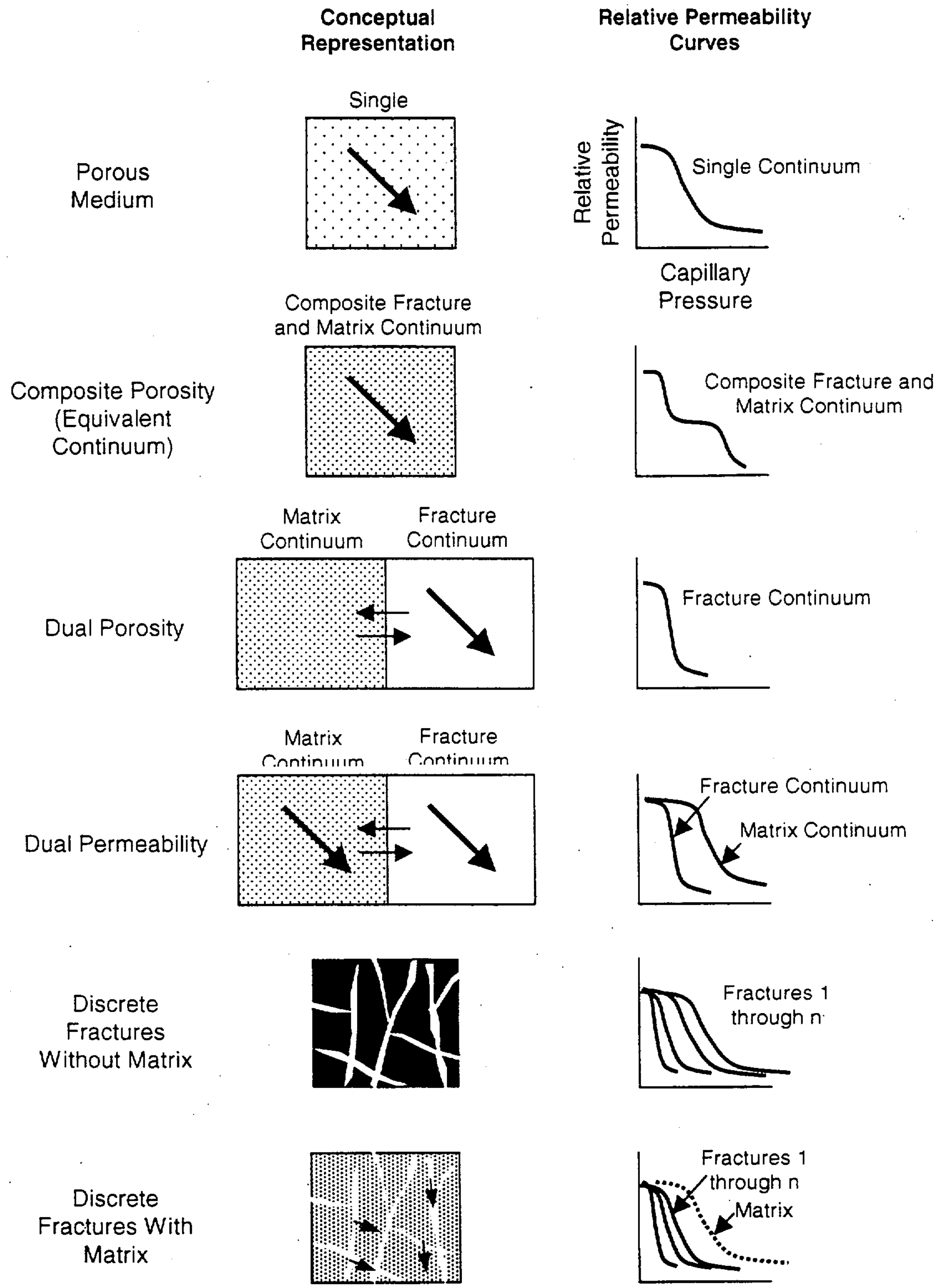

Figure 2-6. Alternative conceptual models and corresponding relative-permeability curves for flow through fractured rock.

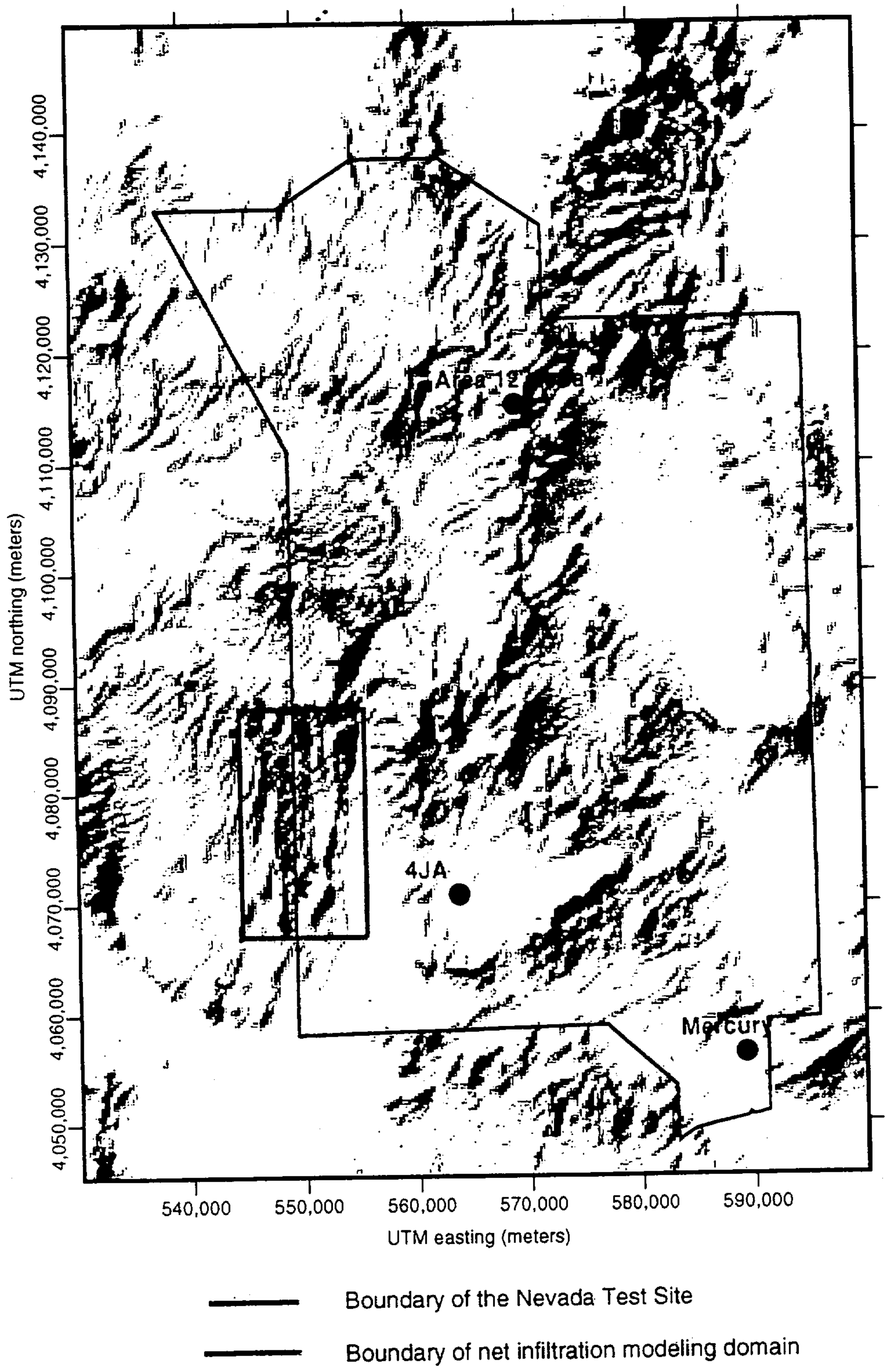

Figure 2-7. Location of net infiltration modeling domain relative to regional topography and the boundaries of the Nevada Test Site.

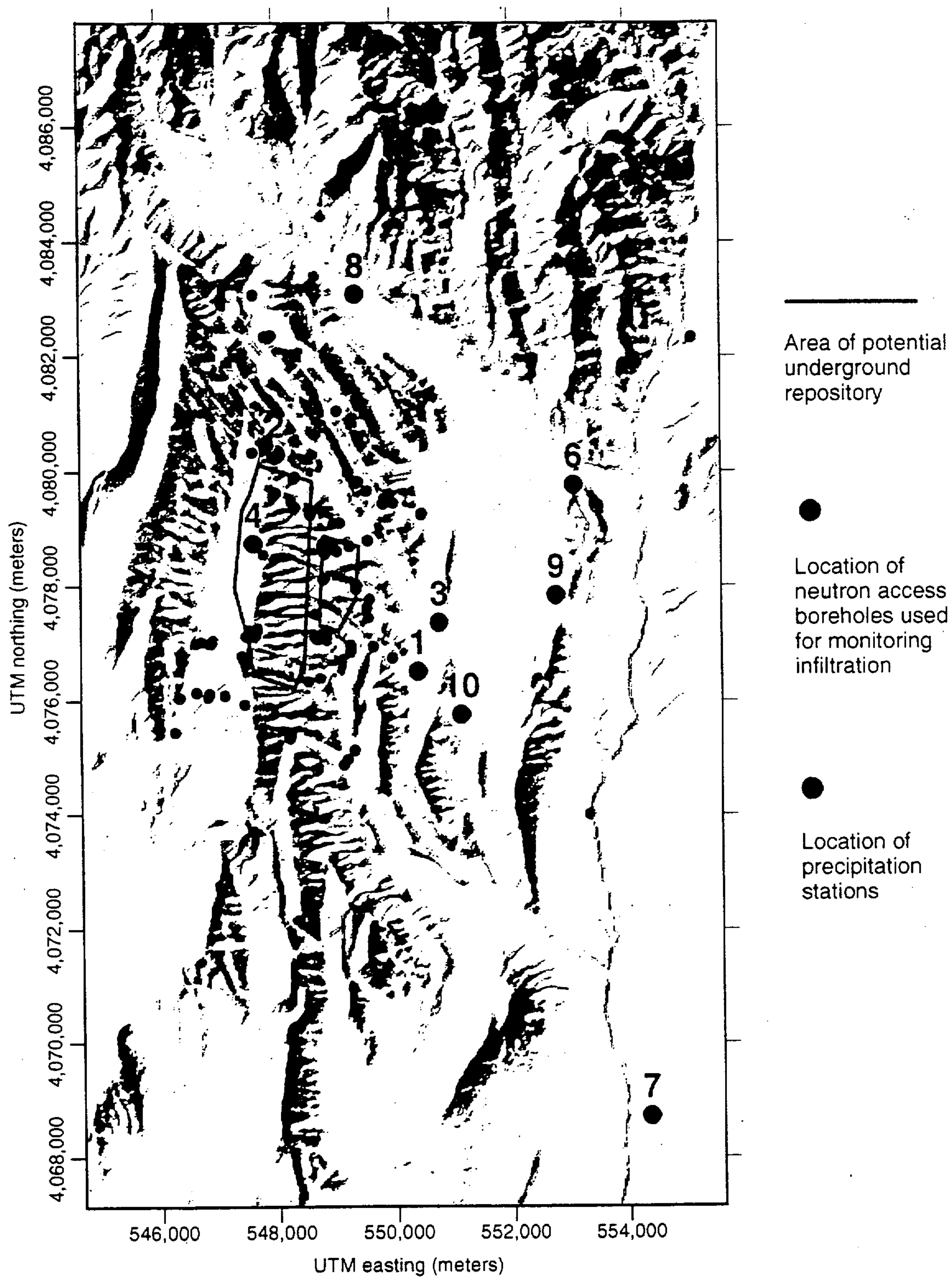

Figure 2-8. Infiltration modeling domain, showing shaded relief generated from digital elevation data used for model input.

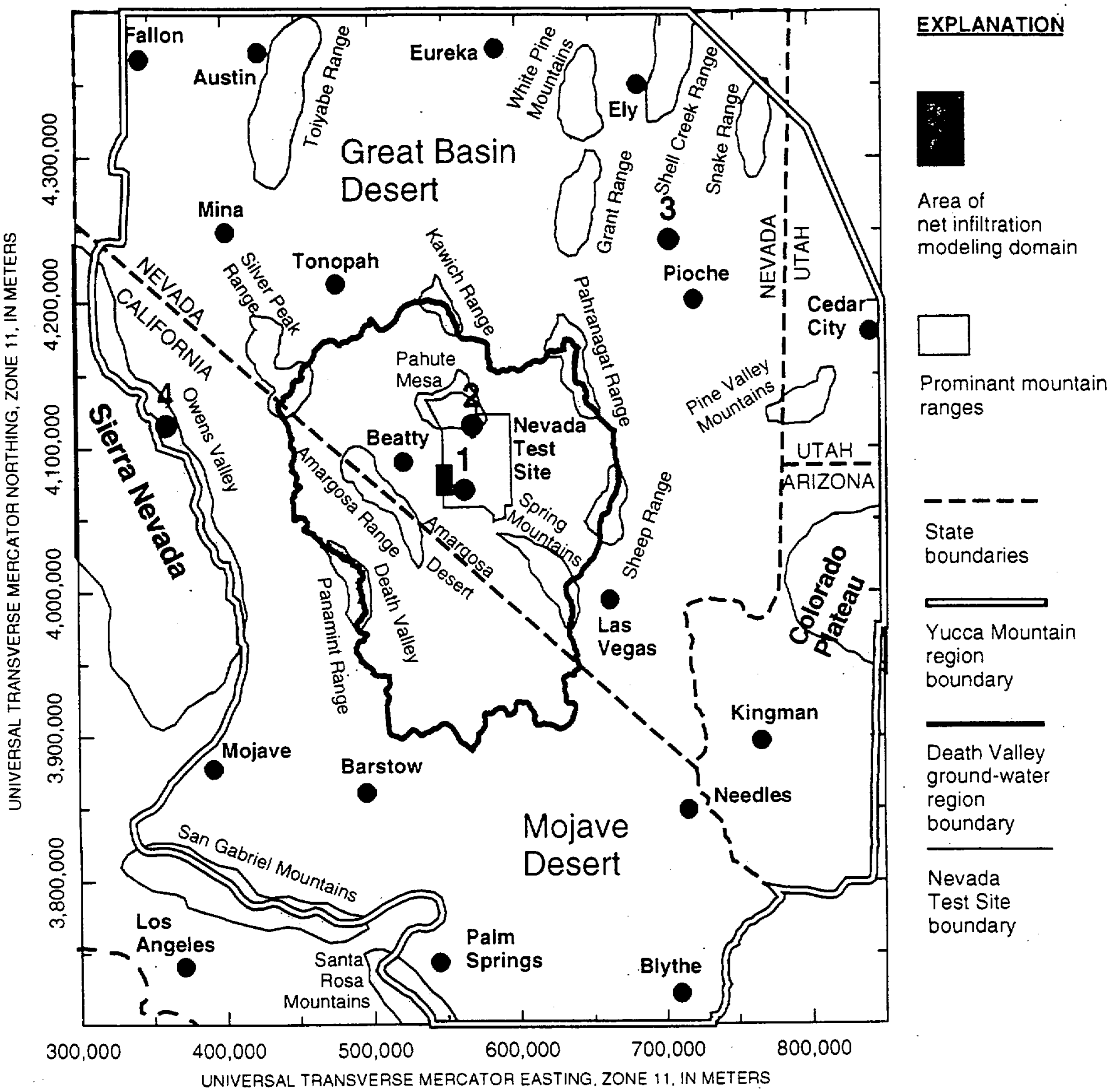

● Precipitation stations.

1 4JA (current climate analog)
2 Area 12 Mesa (wetter future climate analog)
3 Lake Valley - Steward (wetter future climate analog)
4 South Lake (wetter future climate analog)

Figure 2-9. Location of precipitation stations in the Yucca Mountain region used for developing daily precipitation models of analog climates.

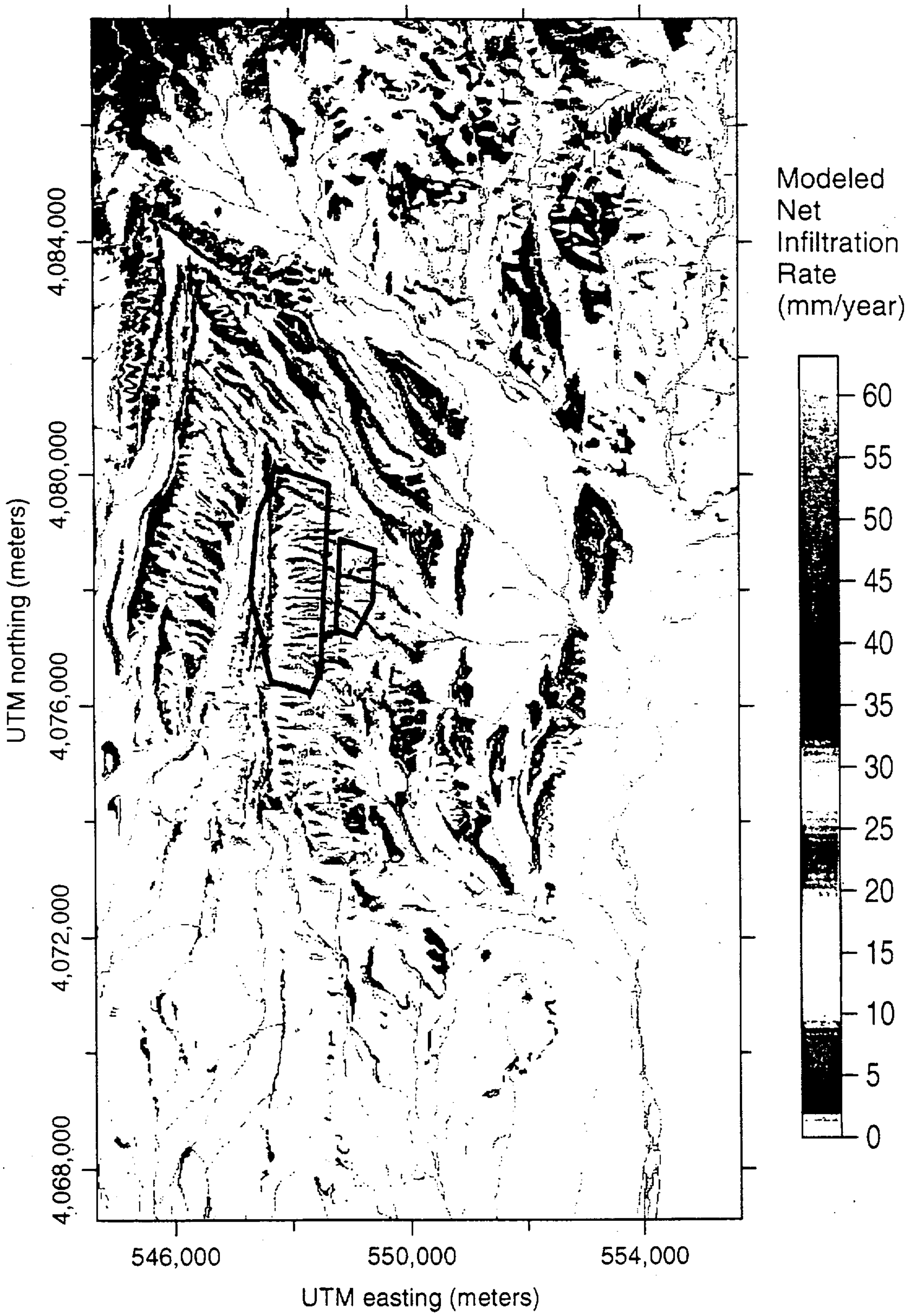

Figure 2-10. Modeled net infiltration rates for Yucca Mountain using the scaled 4JA analog current-climate, 100-year stochastic simulation.

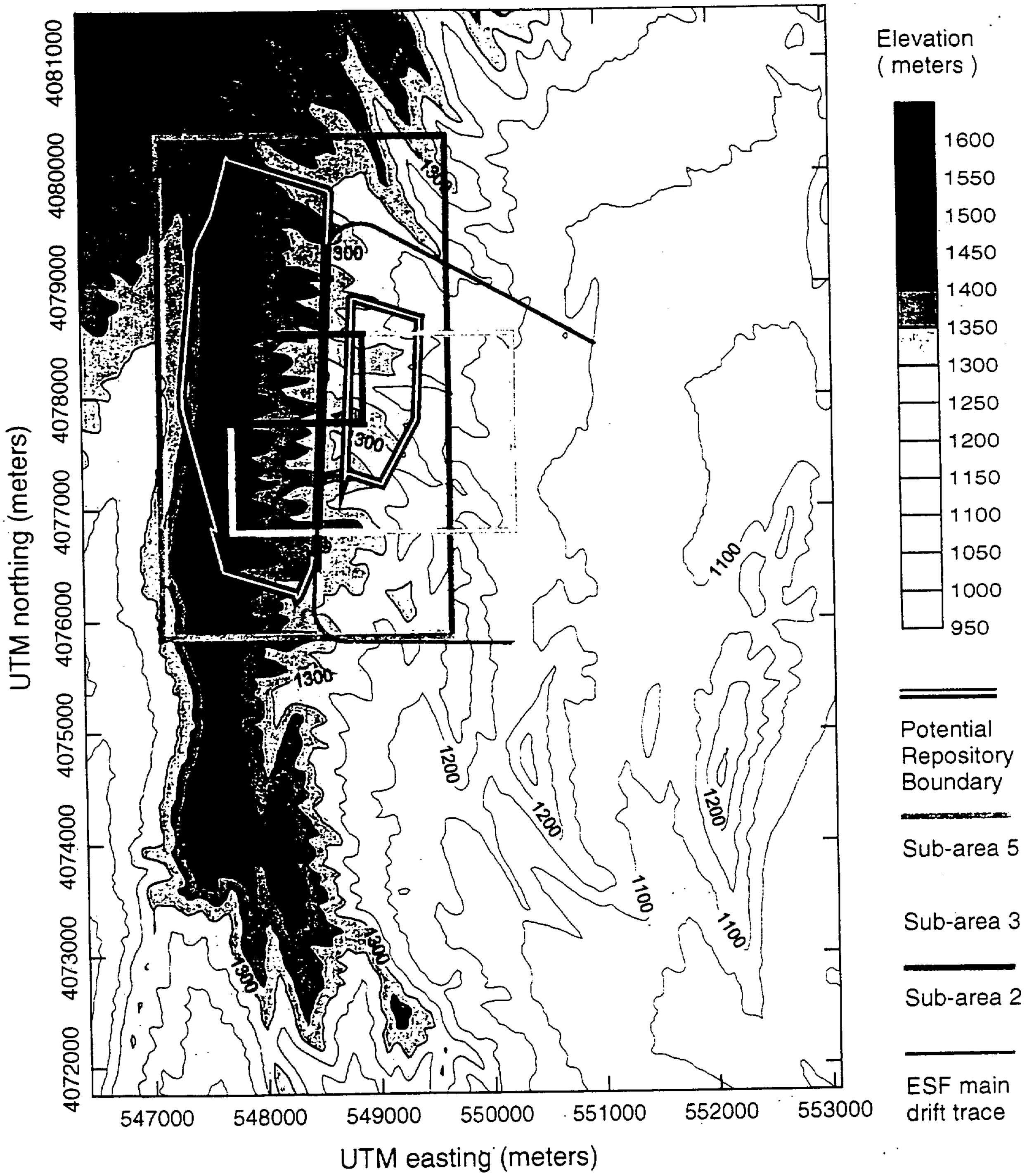

Figure 2-11. Location of sub-areas within the net-infiltration modeling domain.

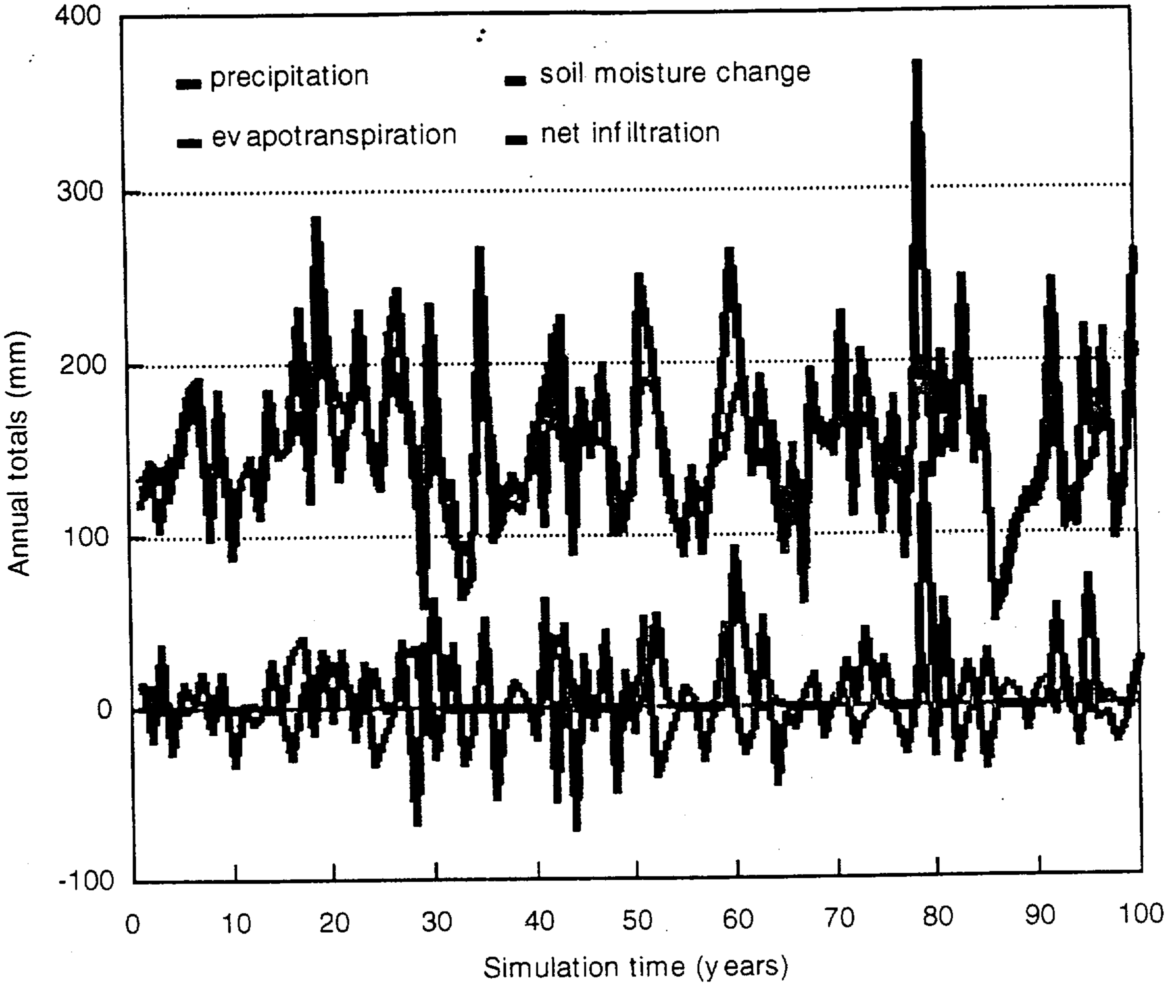

Figure 2-12. Annual simulation results for the location of borehole SD-9 using the 100-year current-climate simulation for Yucca Mountain.

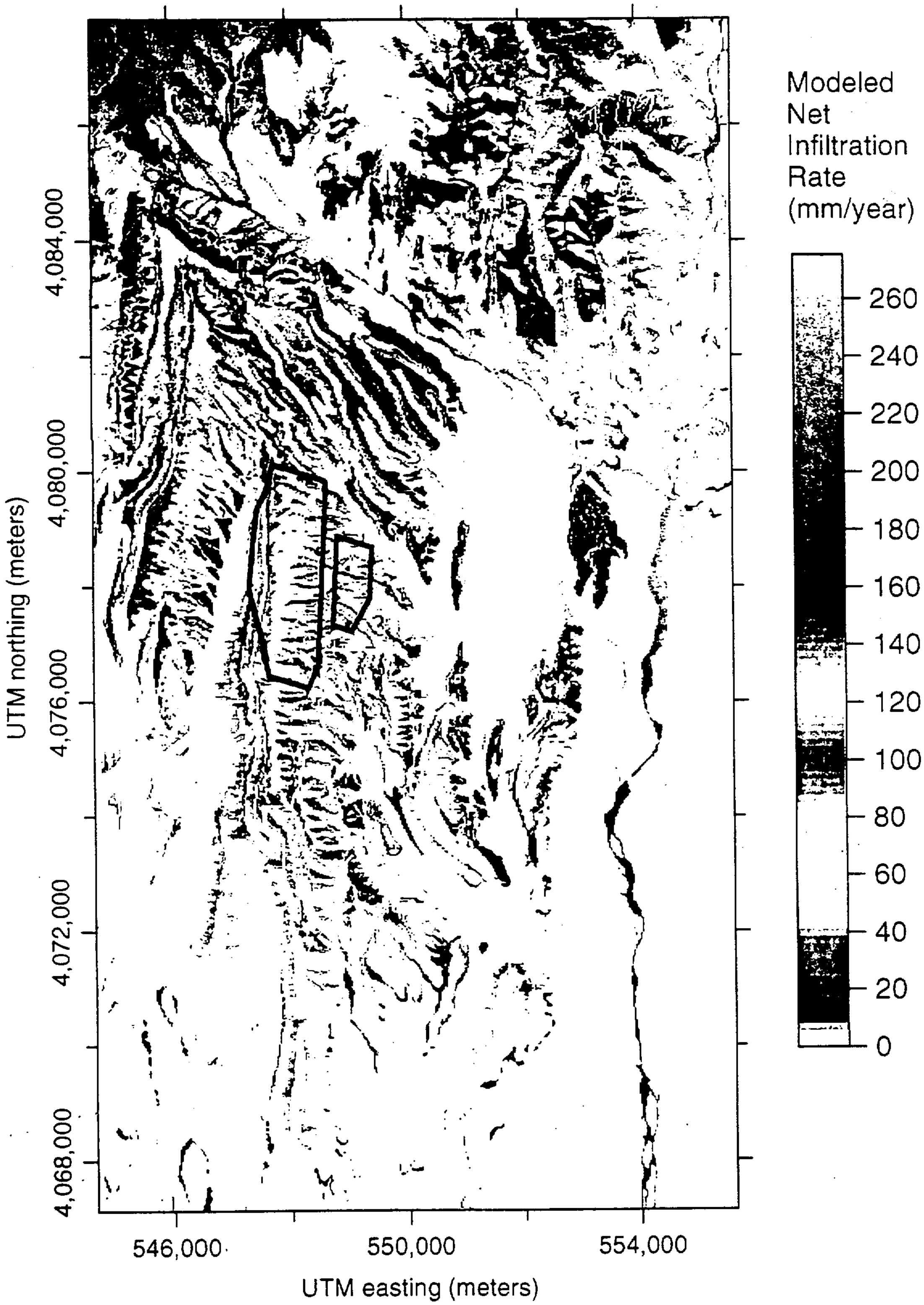

Figure 2-13. Modeled net infiltration rates for Yucca Mountain using the Area 12 analog potential-future-climate, 100-year simulation.

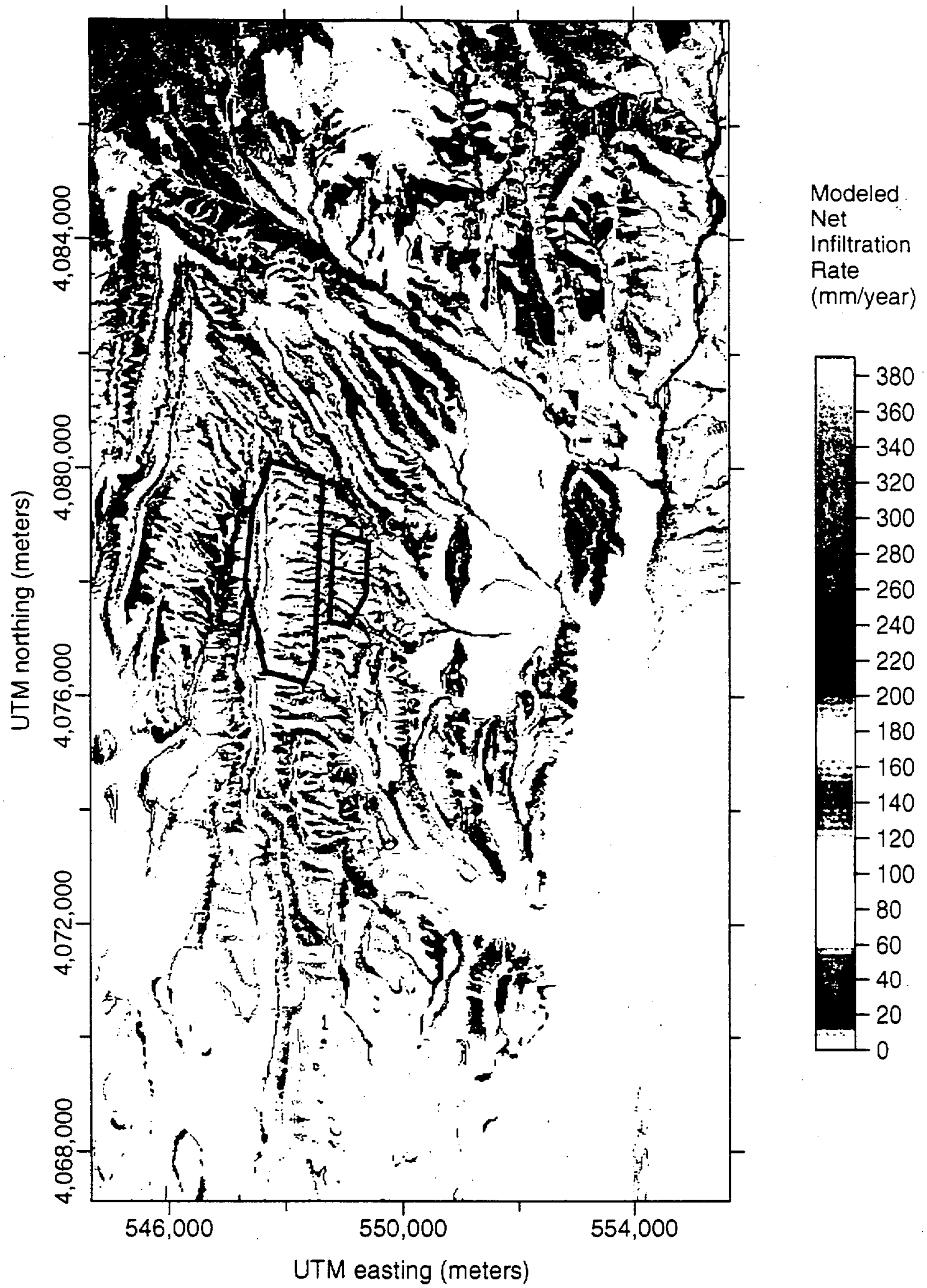

Figure 2-14. Modeled net infiltration for Yucca Mountain using the Lake Valley – Steward analog potential-future-climate, 100-year simulation.

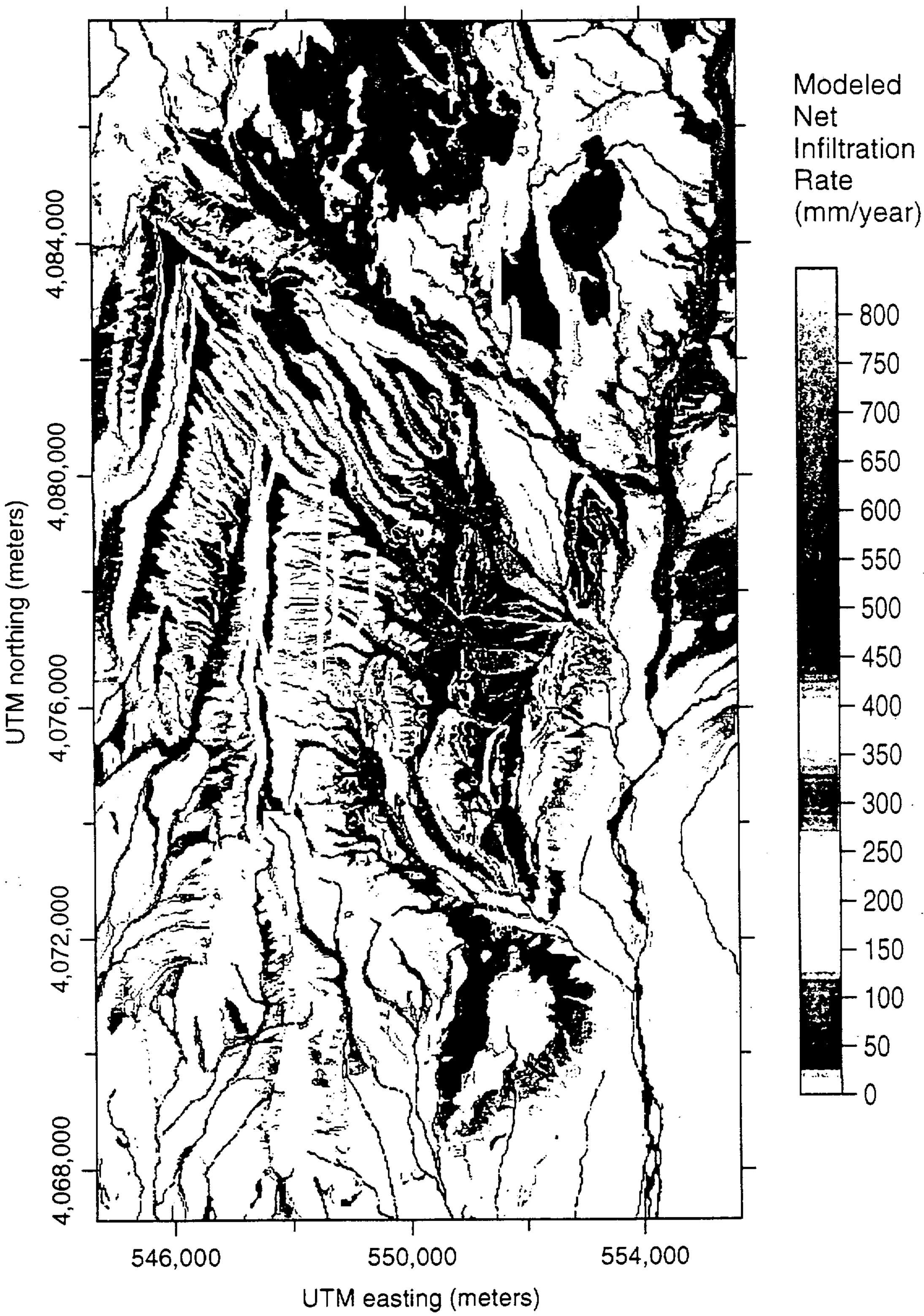

Figure 2-15. Modeled net infiltration rates for Yucca Mountain using the South Lake analog potential-future-climate, 100-year simulation.

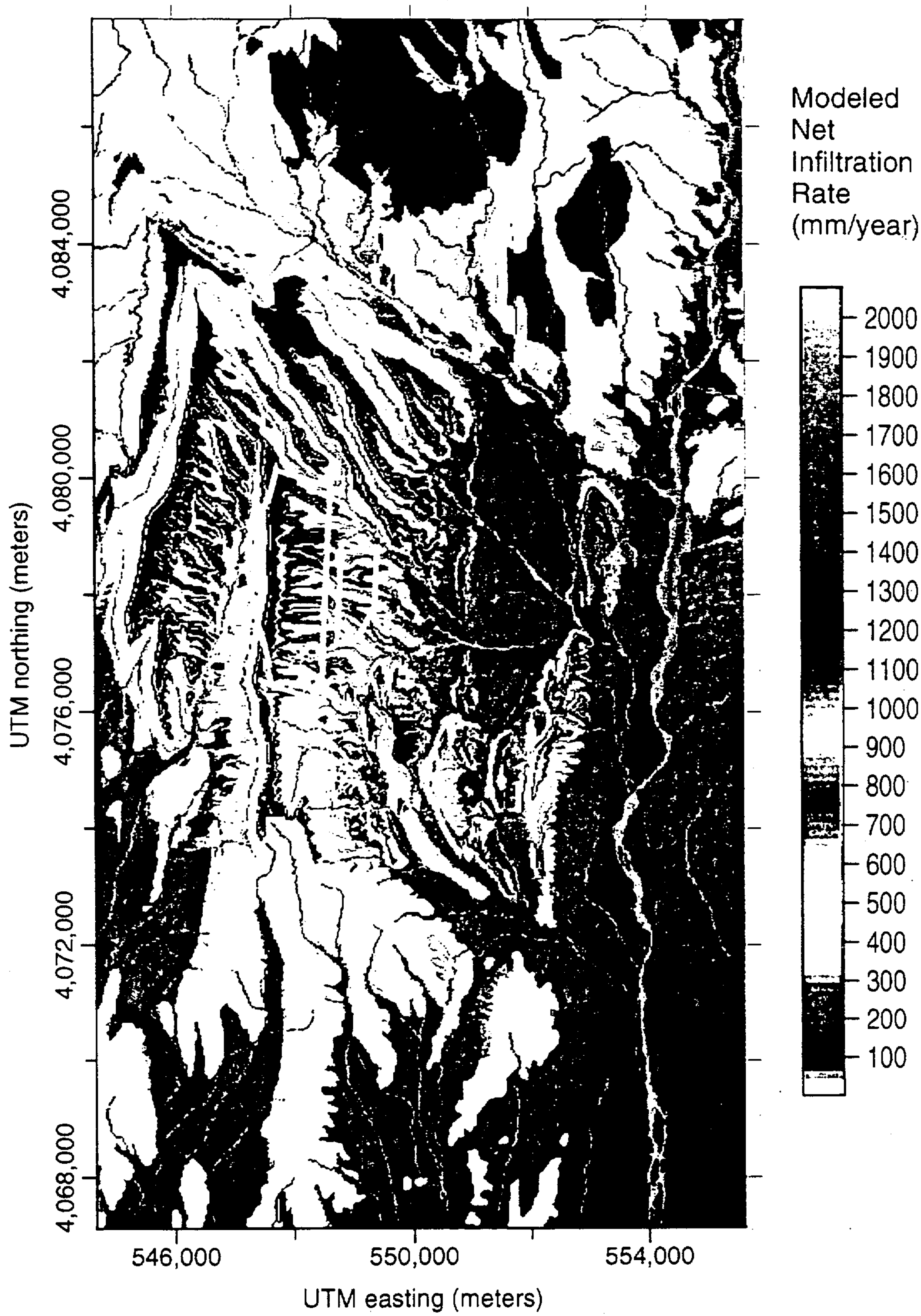

Figure 2-16. Modeled net infiltration rates for Yucca Mountain using the scaled South Lake analog potential-future-climate, 100-year simulation.

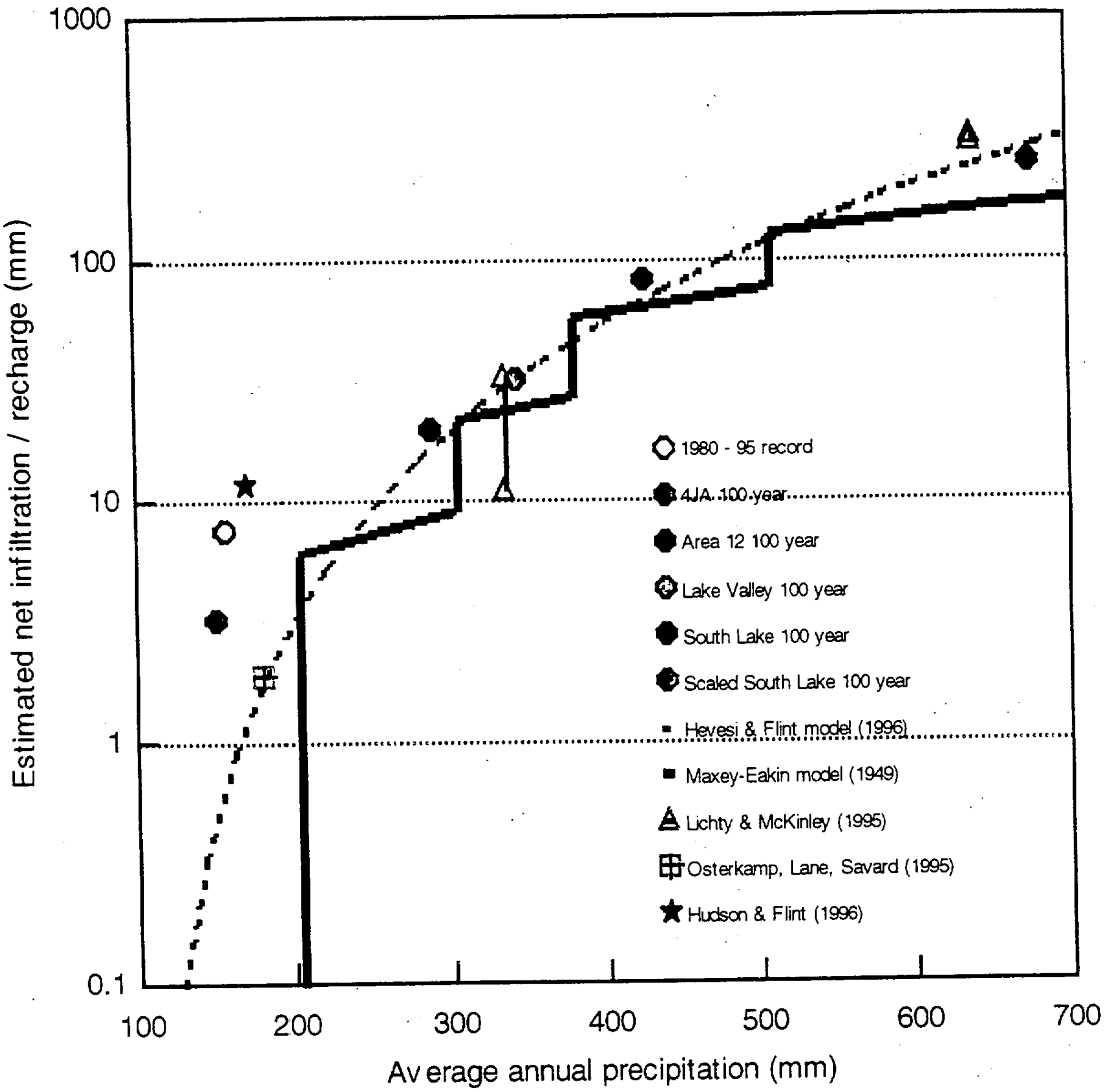

Figure 2-17. Comparison of net-infiltration and recharge estimates as a function of estimated average annual precipitation.

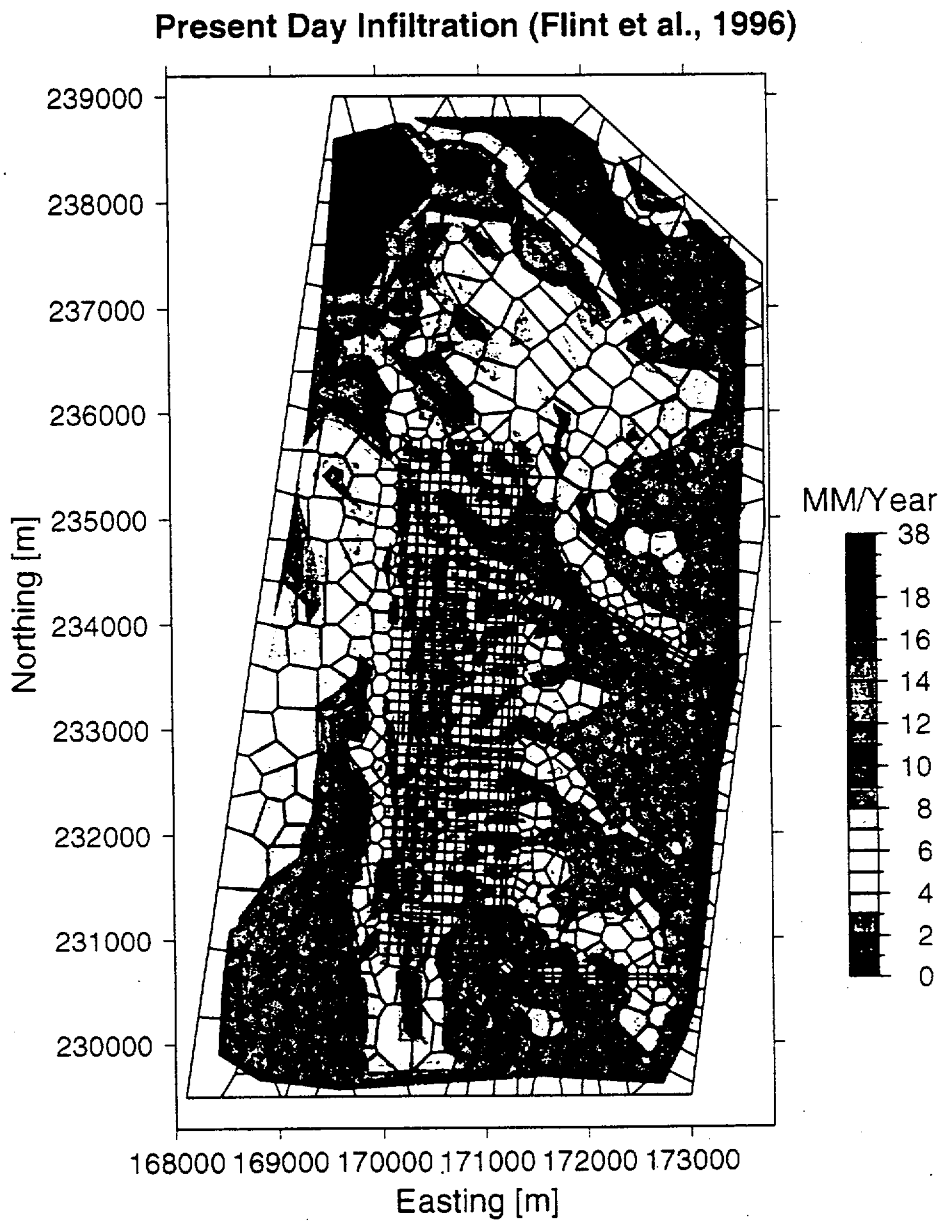

Figure 2-18. Present-day net infiltration map over the LBNL UZ-flow model with an average of 4.9 mm/year. (LB971100001254.002)

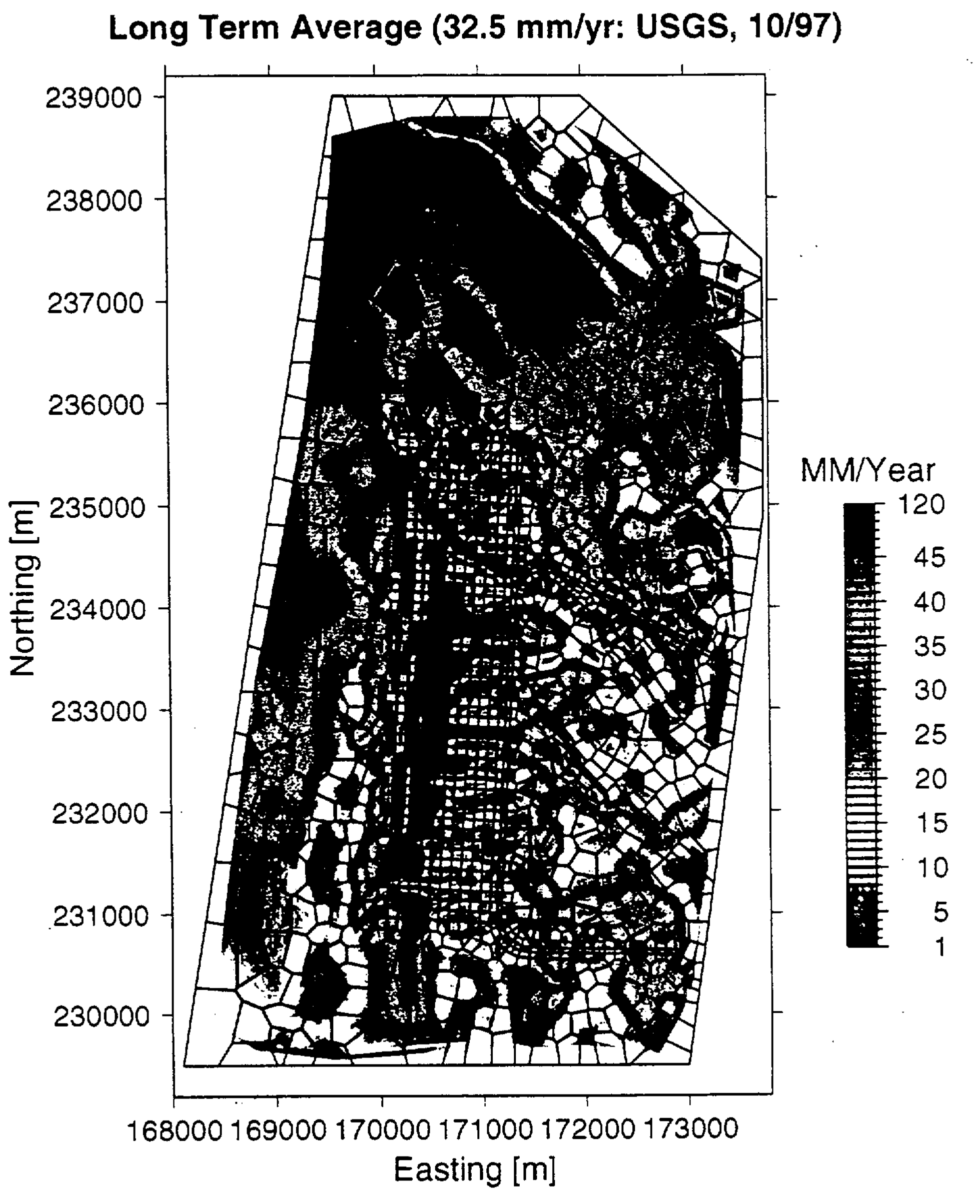

Figure 2-19. Long-term average net infiltration map over the LBNL UZ-flow model with an average of 32.5 mm/year (from Area 12 Mesa analog). (LB971100001254.002)

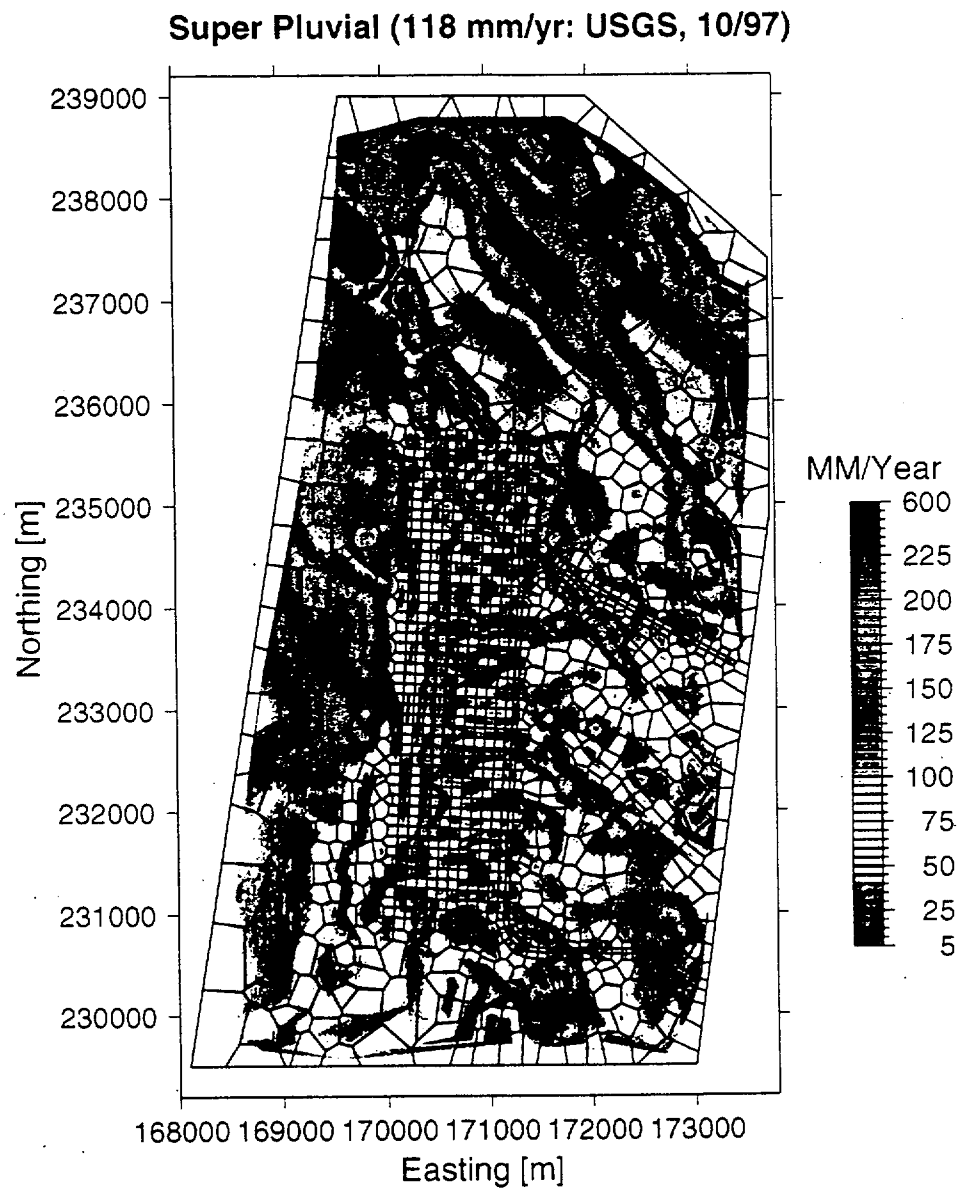

Figure 2-20. Superpluvial net infiltration map over the LBNL UZ-flow model with an average of 118 mm/year (from South Lake analog). (LB971100001254.002)

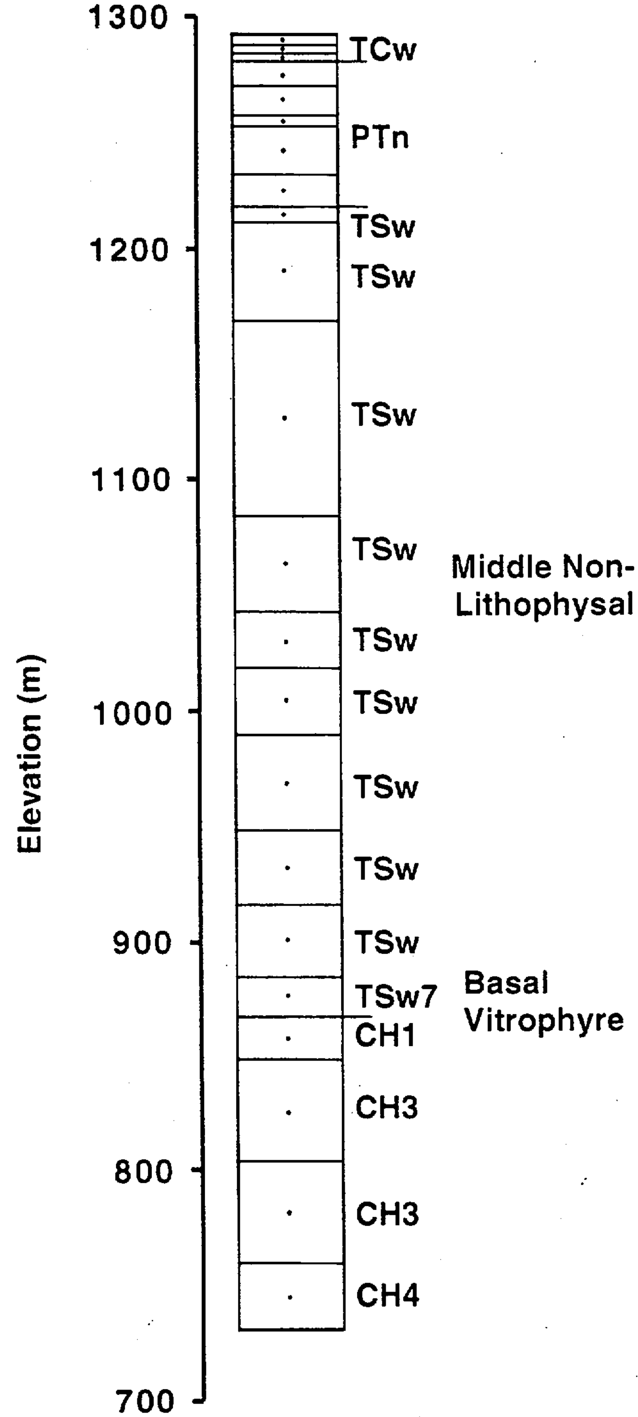

Figure 2-21. 1-D TOUGH2 mesh used in sensitivity analyses.

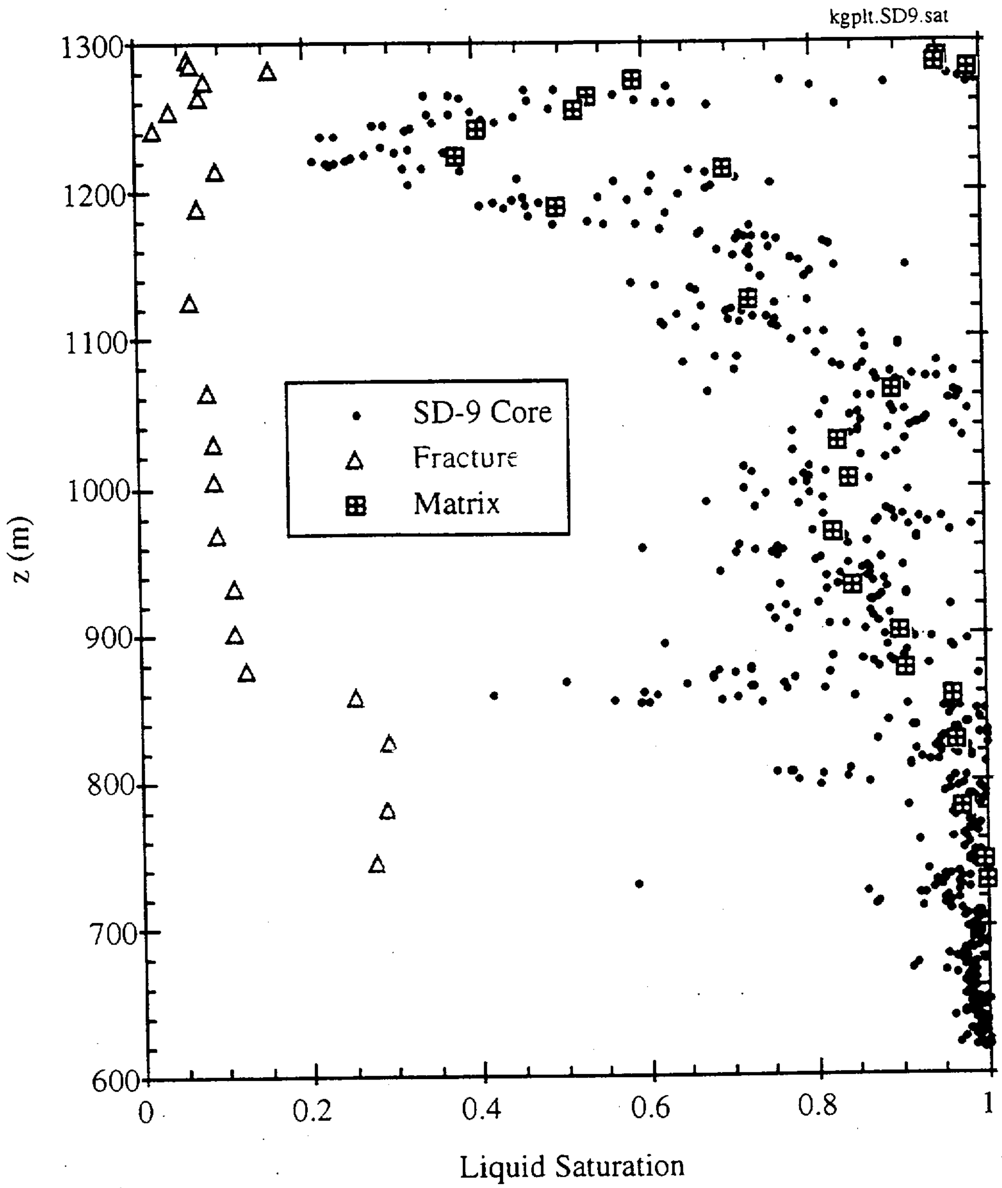

Figure 2-22. Equilibrium-simulation results: saturation vs. elevation for core, fracture, and matrix.

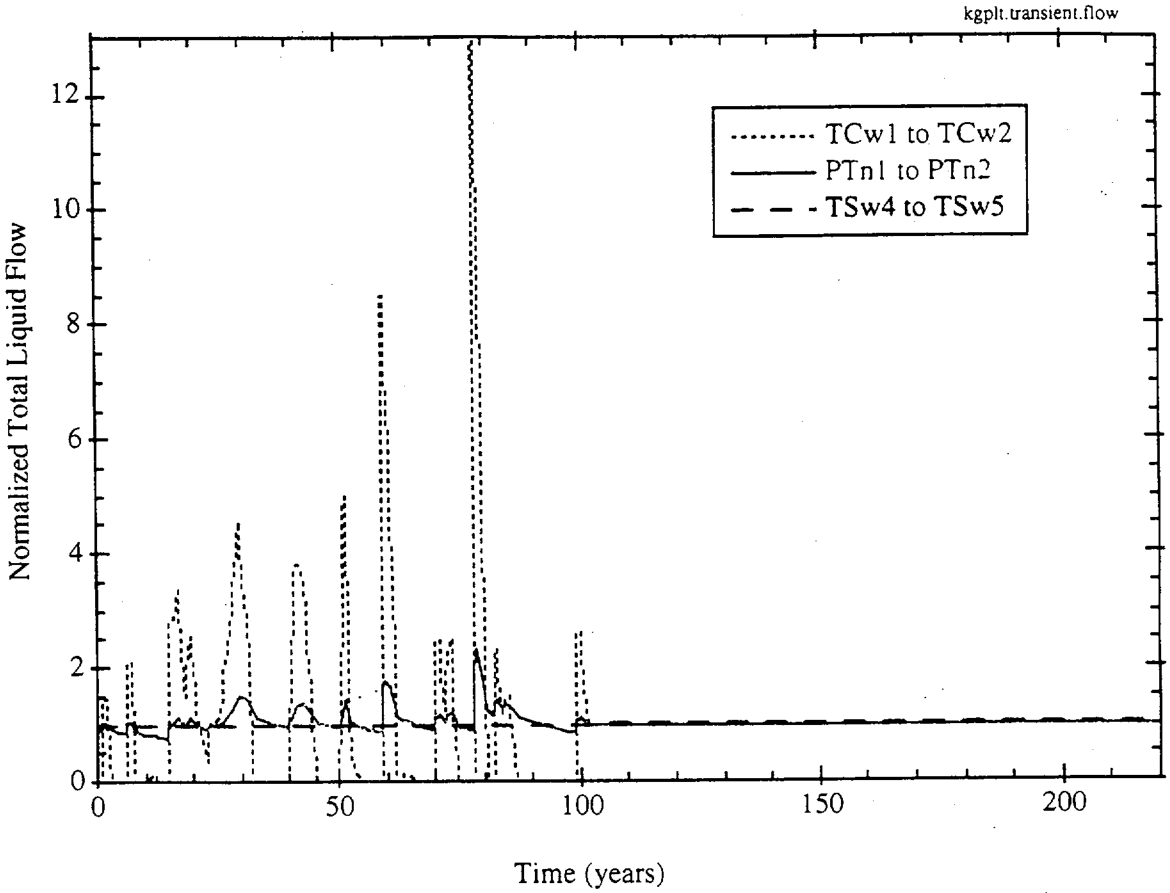

Figure 2-23. Transient simulation: normalized total liquid flow (includes both fracture and matrix). The normalized value of 1 equals steady-state liquid flow of 3.6 mm/yr or 7.76x10-4 kg/s.

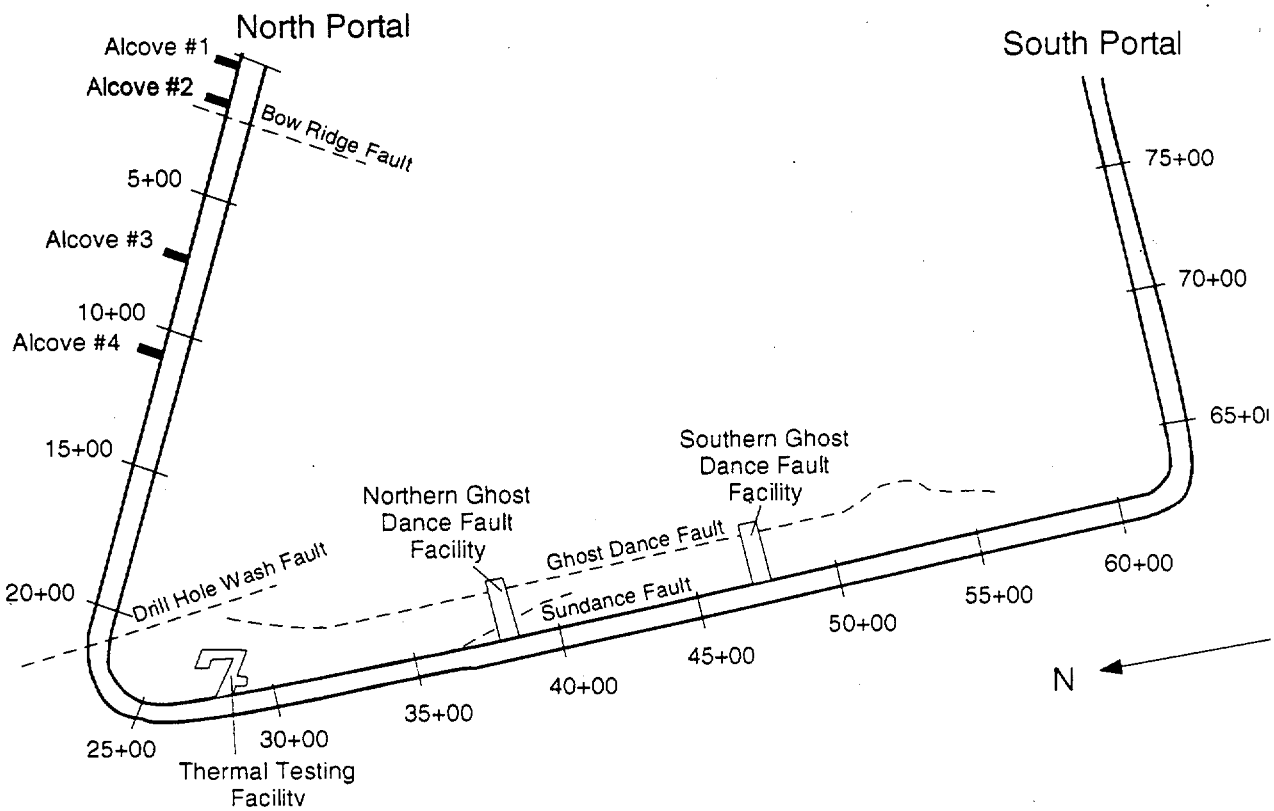

Figure 2-24. Sketch of monitoring stations, alcoves, and test facilities in the Exploratory Studies Facility.

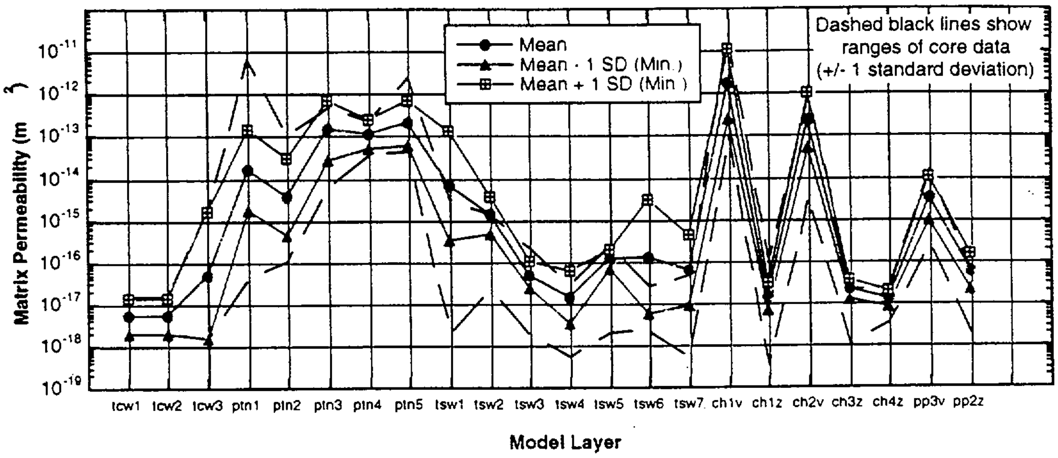

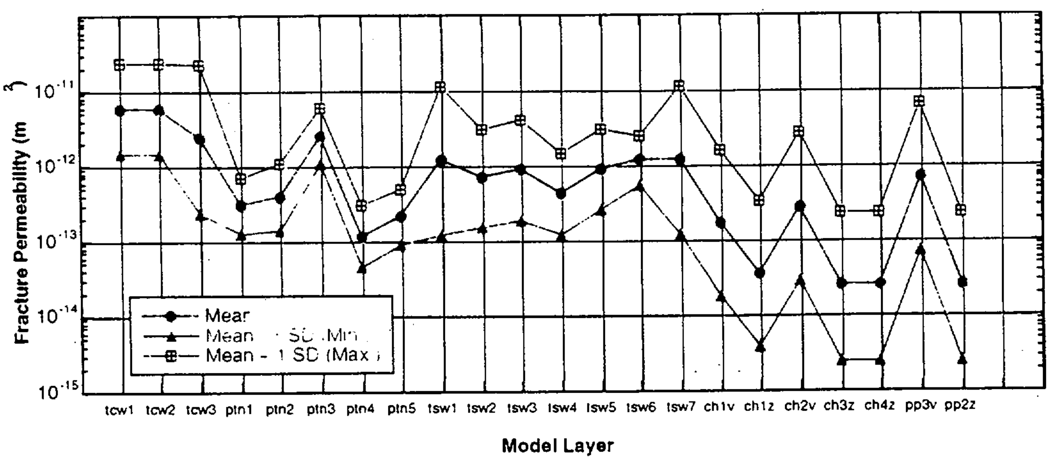

Figure 2-25. Ranges of fracture and matrix permeabilities used in simulations.

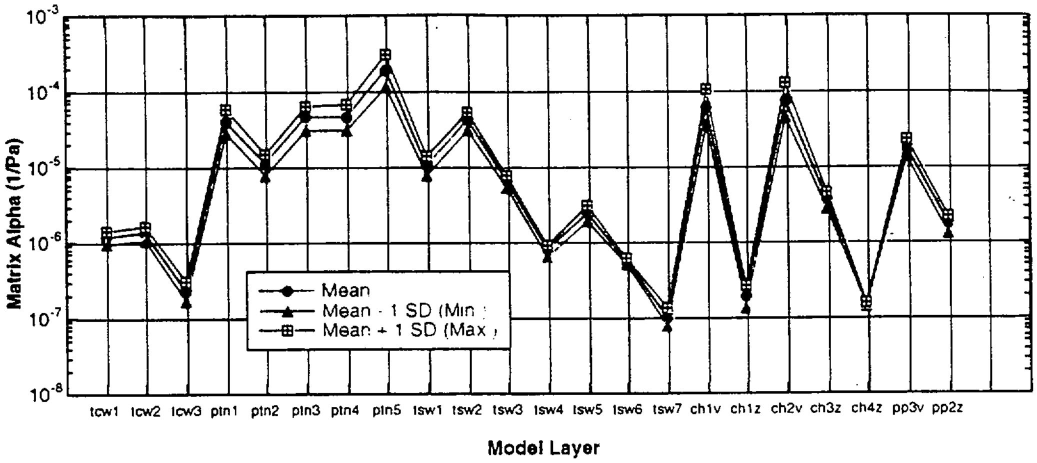

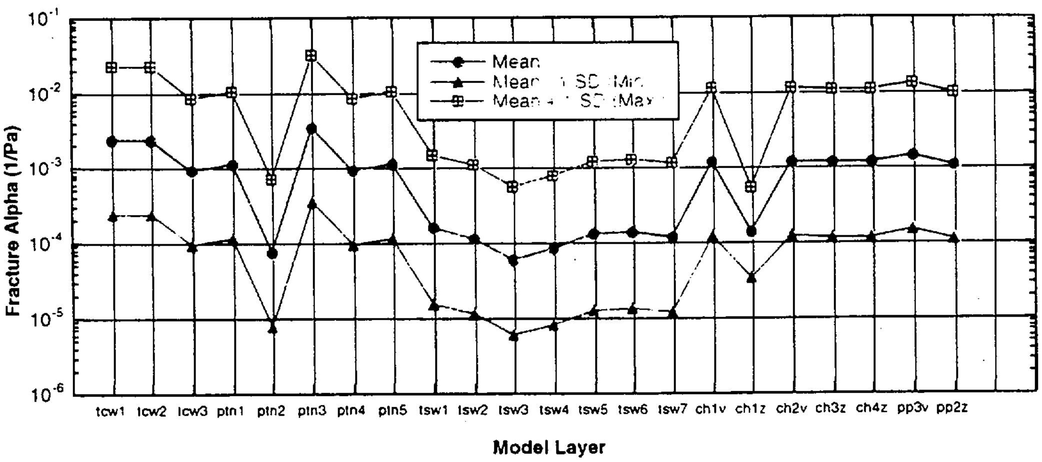

Figure 2-26. Ranges of fracture and matrix alpha used in simulations.

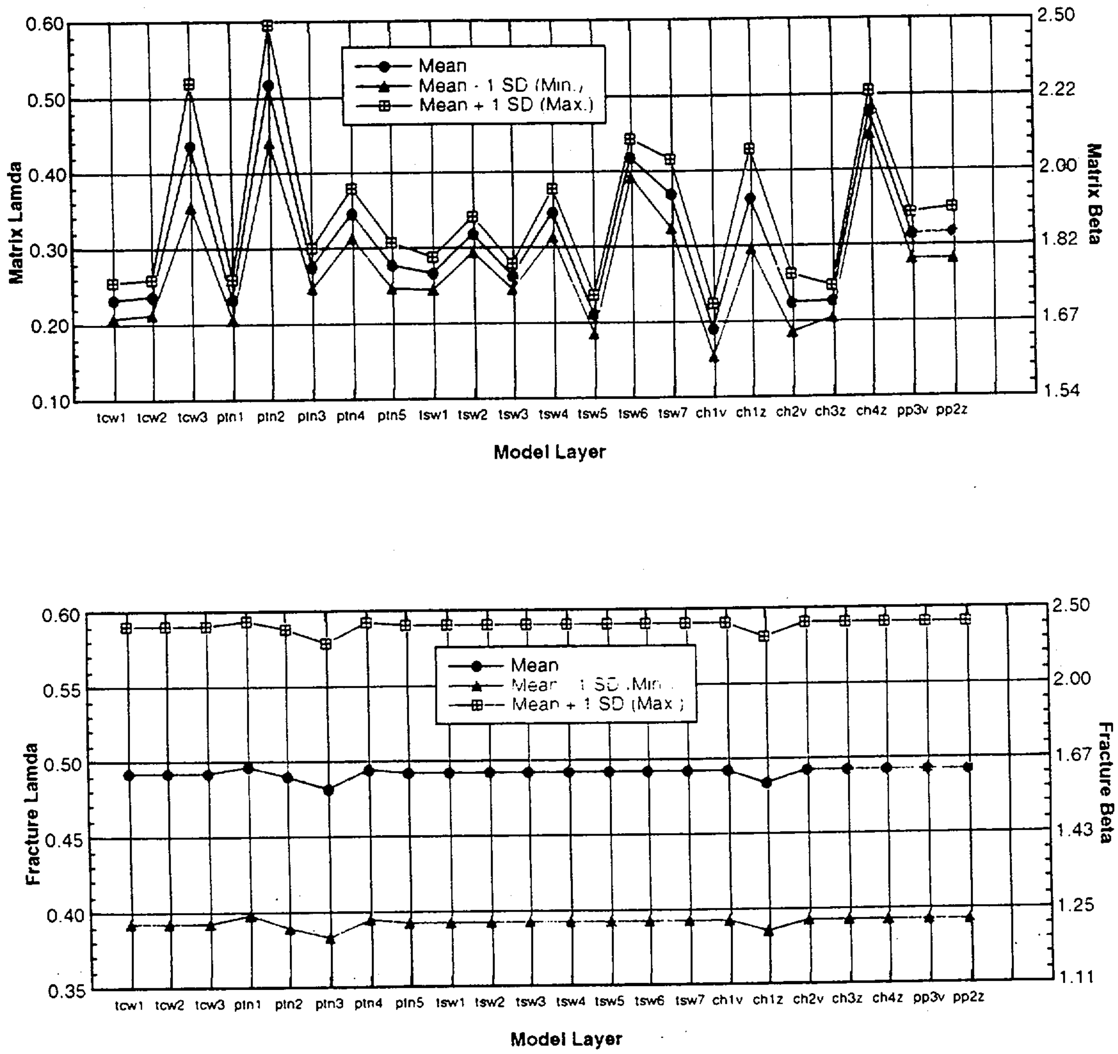

Figure 2-27. Ranges of fracture and matrix lambda (1-1/β; also m) used in simulations.

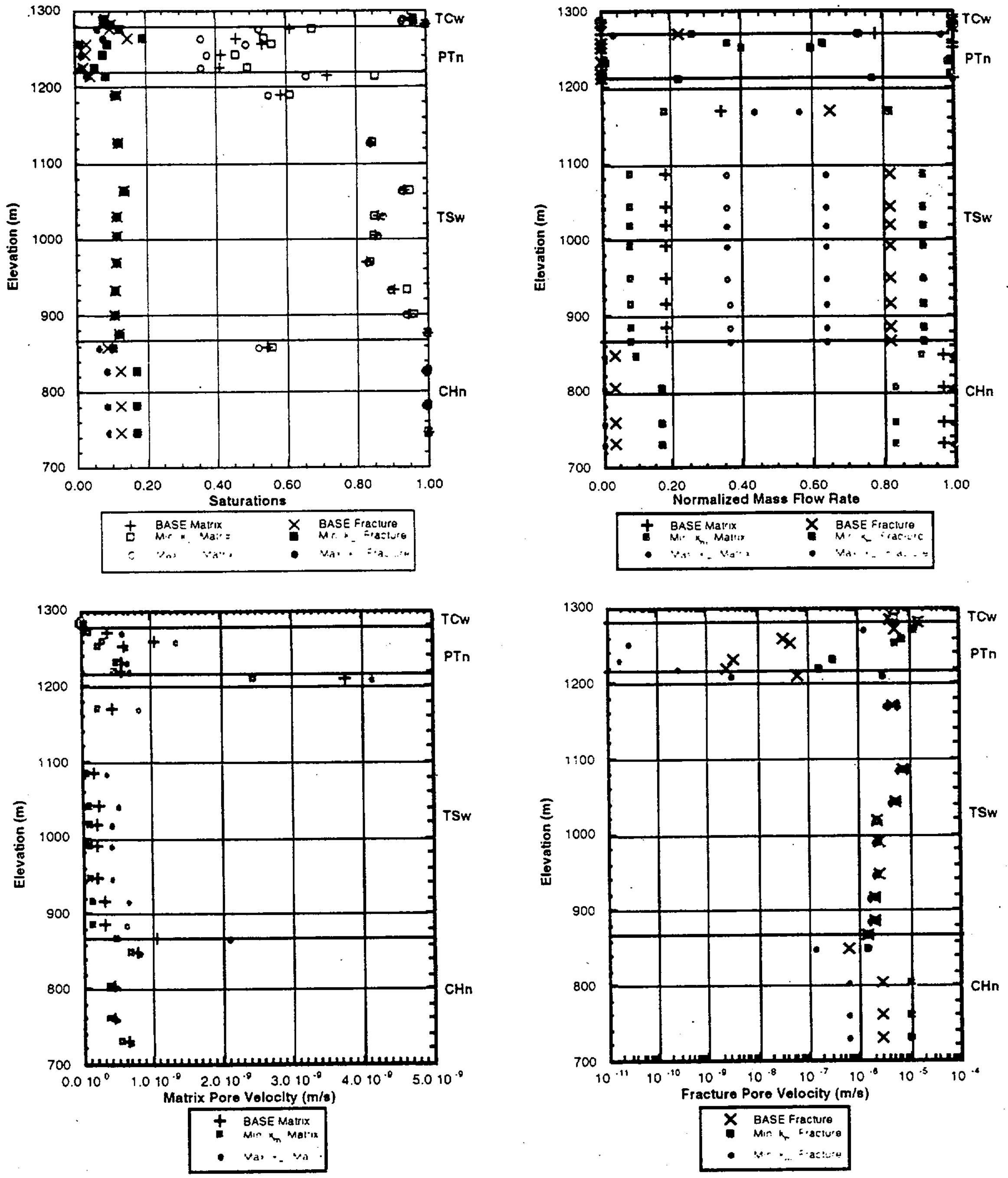

Figure 2-28. Simulated saturations, normalized, mass flow rates (to infiltration), and pore-water velocities from varying matrix permeability by one standard deviation from the mean for all layers. Note that minimum matrix permeability for the upper 3 CHn layers is the mean minus one-half the standard deviation.

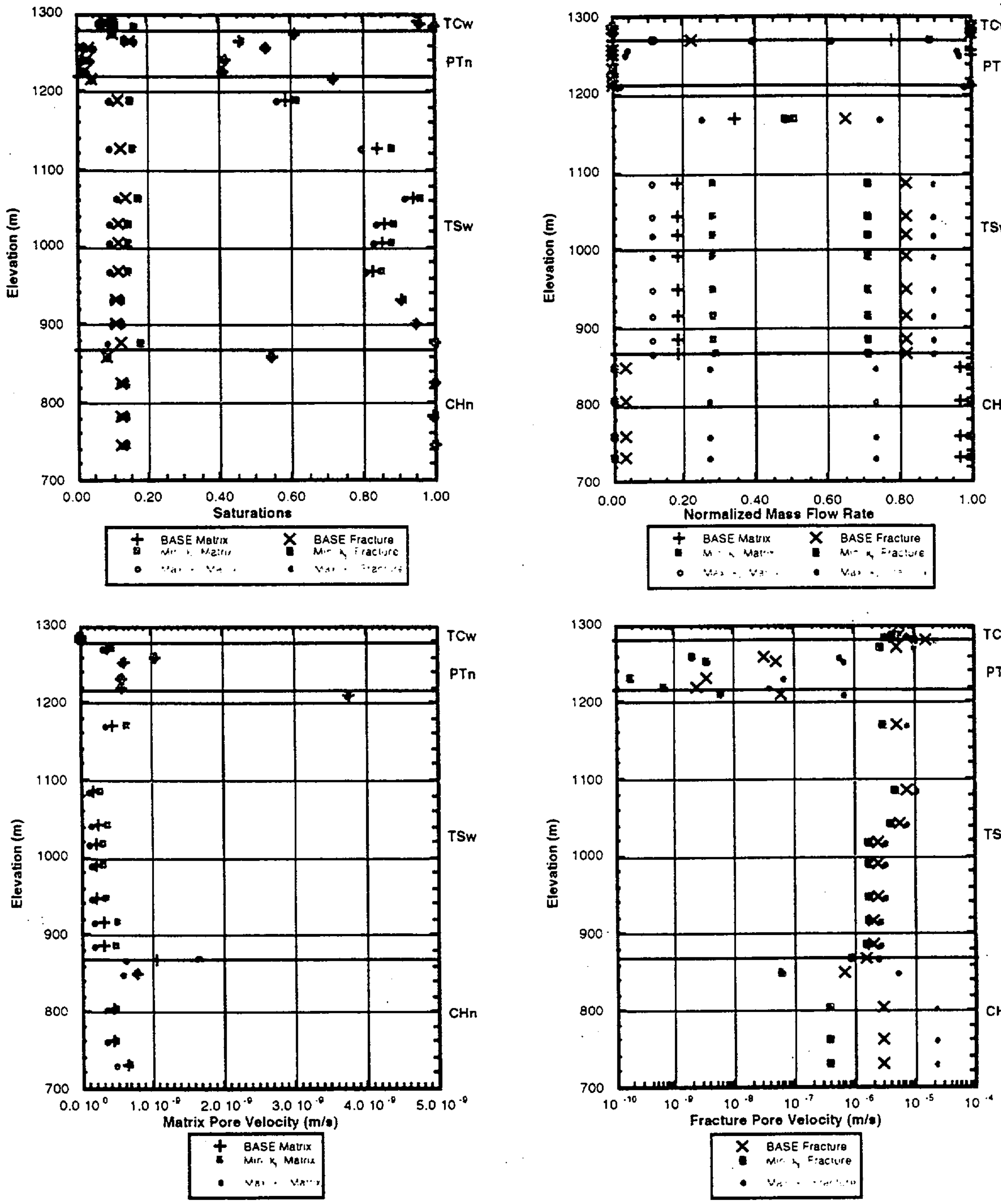

Figure 2-29. Simulated saturations, normalized, mass flow rates (to infiltration), and pore-water velocities from varying fracture permeability by one standard deviation from the mean for all layers.

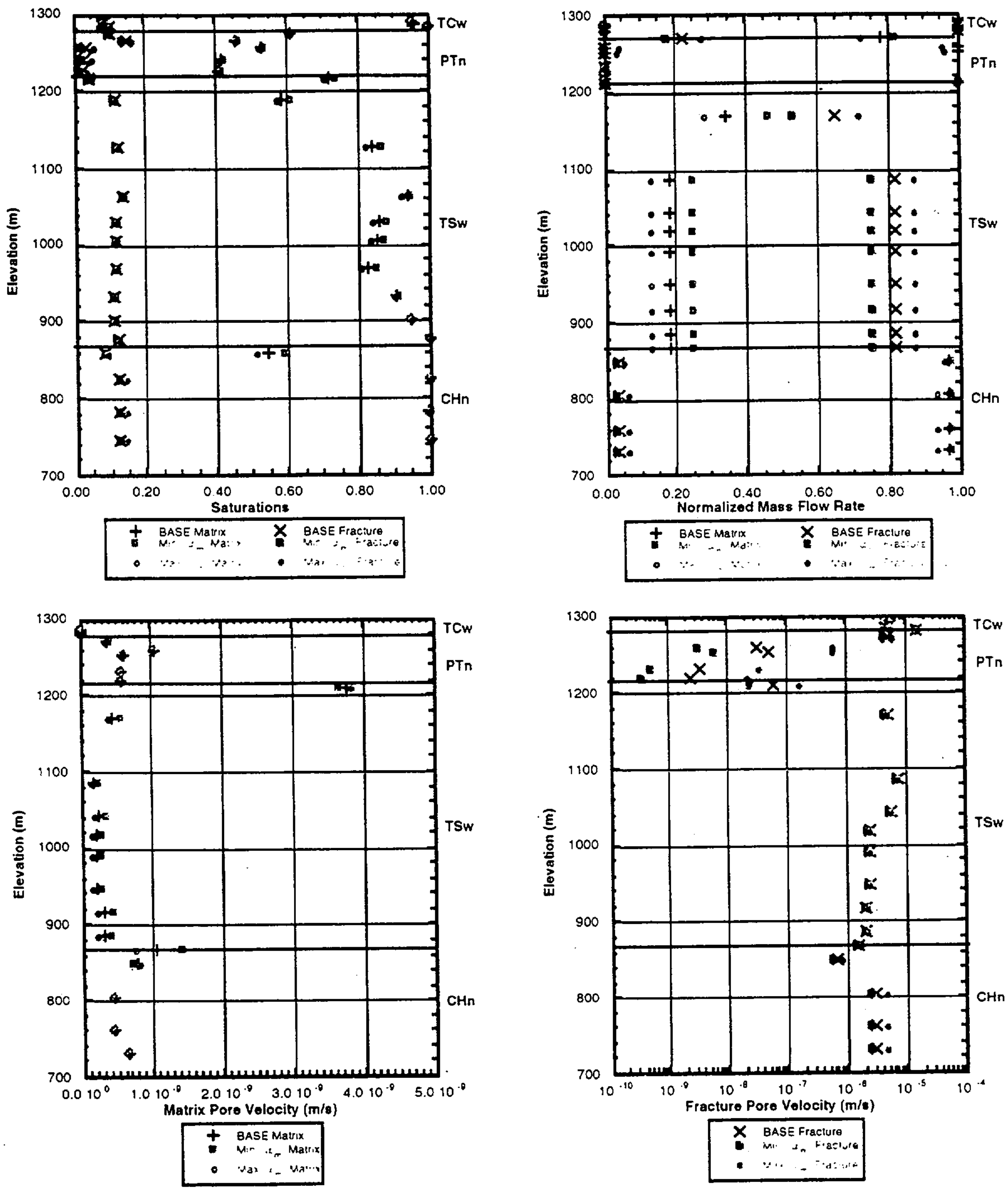

Figure 2-30. Simulated saturations, normalized mass flow rates (to infiltration), and pore-water velocities from varying matrix alpha by one standard deviation from the mean for all layers.

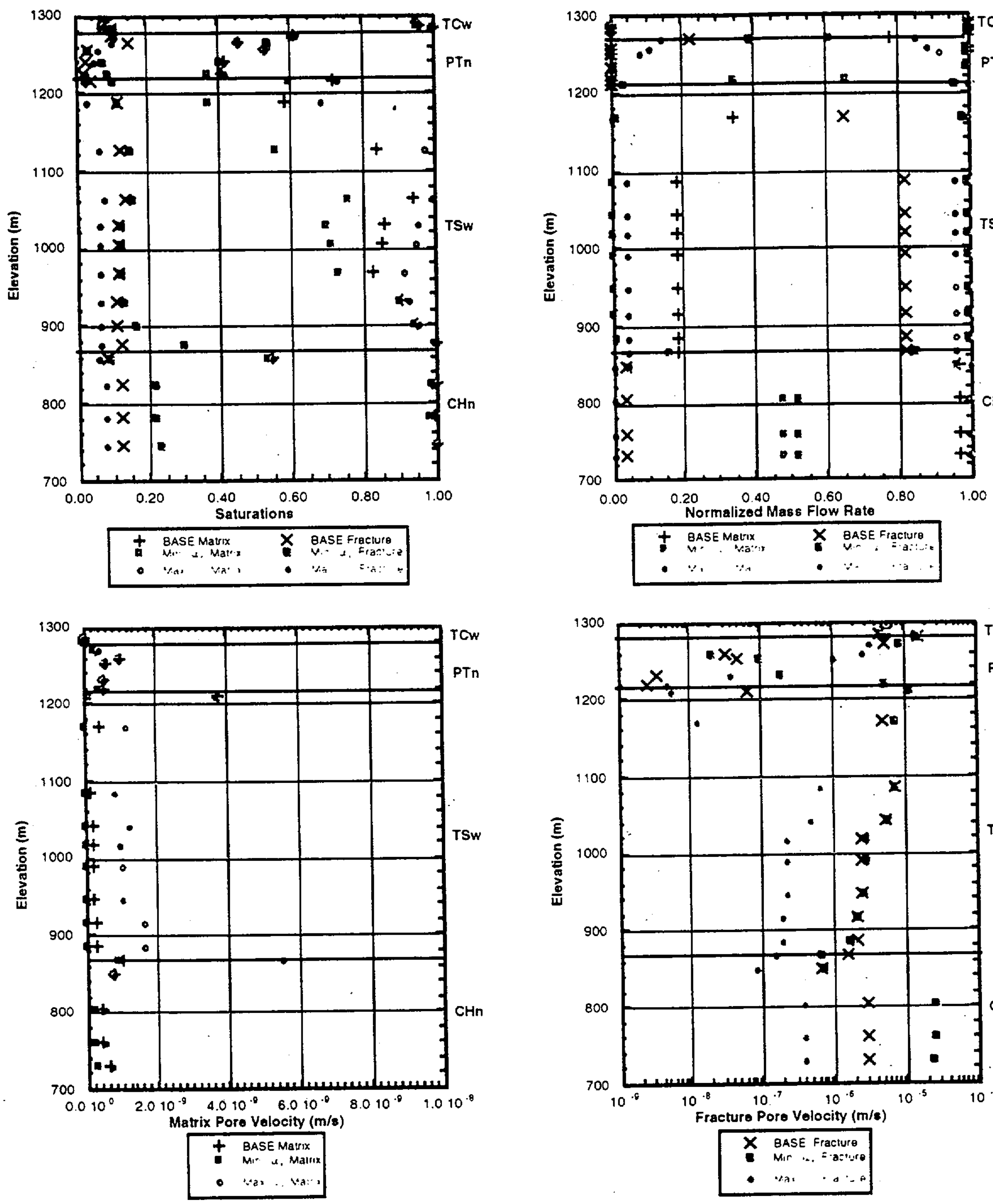

Figure 2-31. Simulated saturations, normalized mass flow rates (to infiltration), and pore-water velocities from varying fracture alpha by one standard deviation from the mean for all layers.

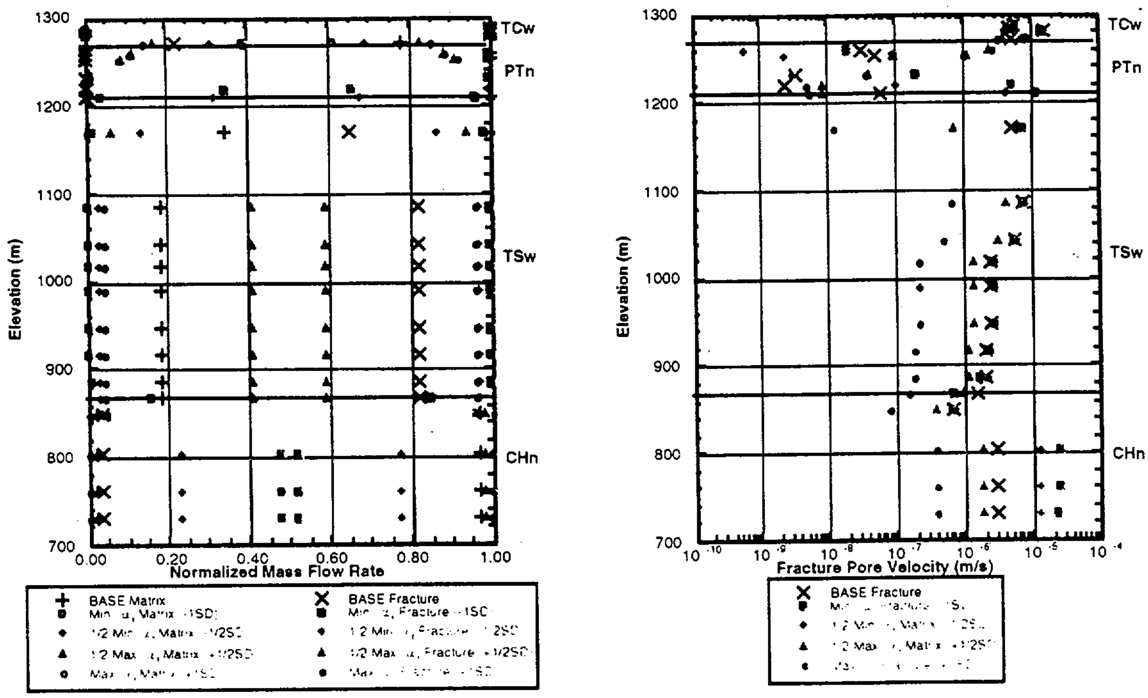

Figure 2-32. Simulated normalized (to infiltration), mass flow rates, and pore-water velocities from varying fracture alpha by one standard deviation and one-half a standard deviation from the mean for all layers.

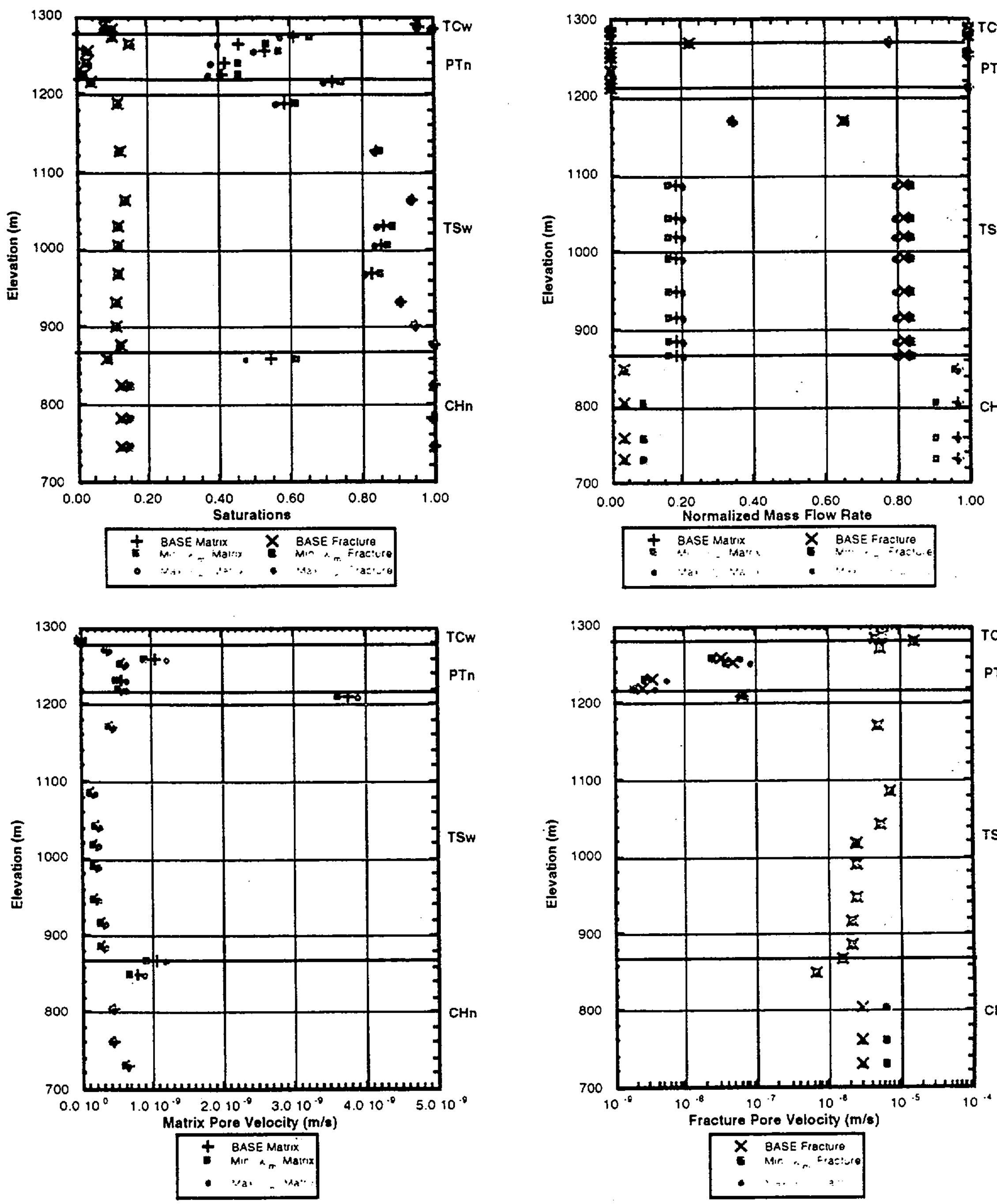

Figure 2-33. Simulated saturations, normalized (to infiltration), mass flow rates, and pore-water velocities from varying matrix lambda by one standard deviation from the mean for all layers.

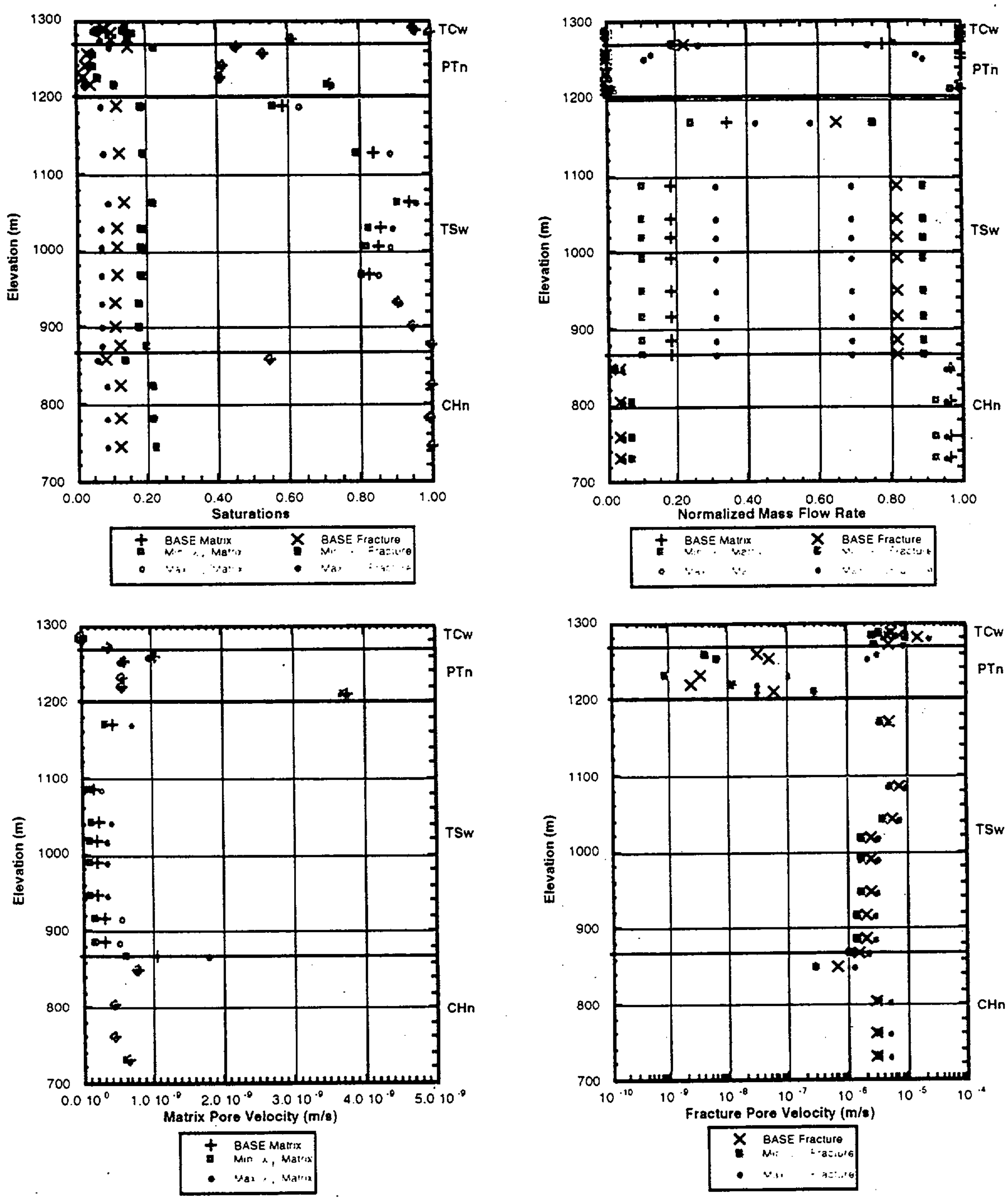

Figure 2-34. Simulated saturations, normalized (to infiltration), mass flow rates, and pore-water velocities from varying fracture lambda by one standard deviation from the mean for all layers.

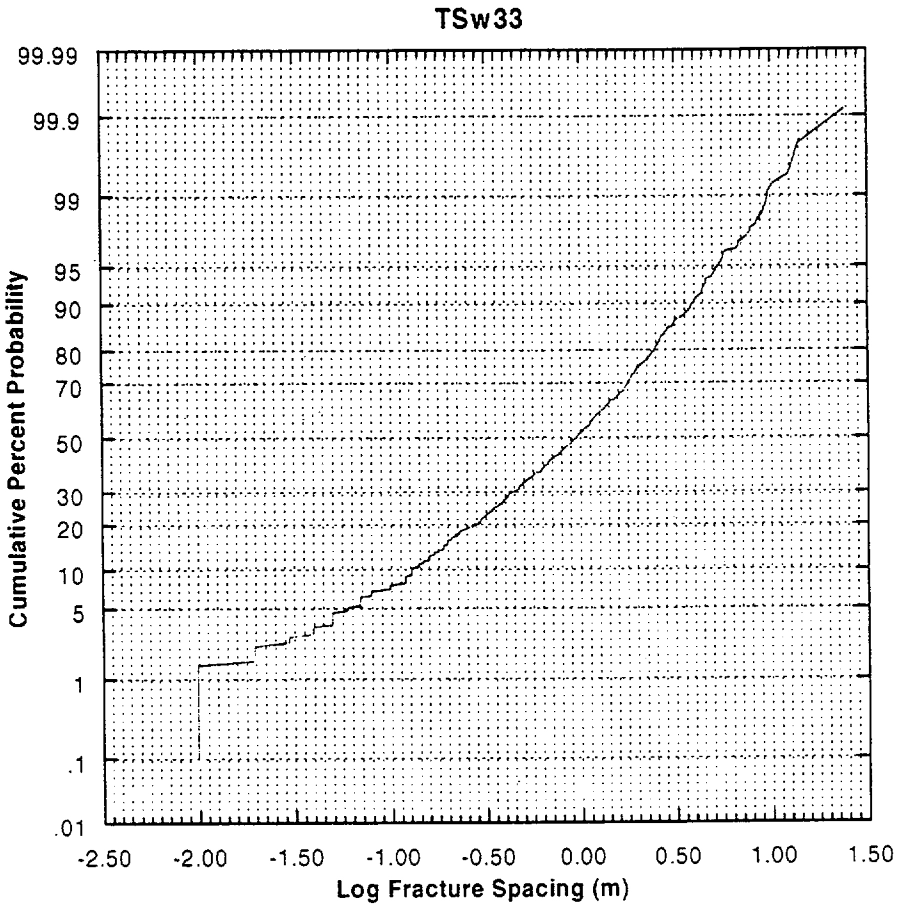

Figure 2-35. Percent probability curve for fracture spacing in the TSw33 layer. This distribution approximates a lognormal distribution (which would yield a straight line).

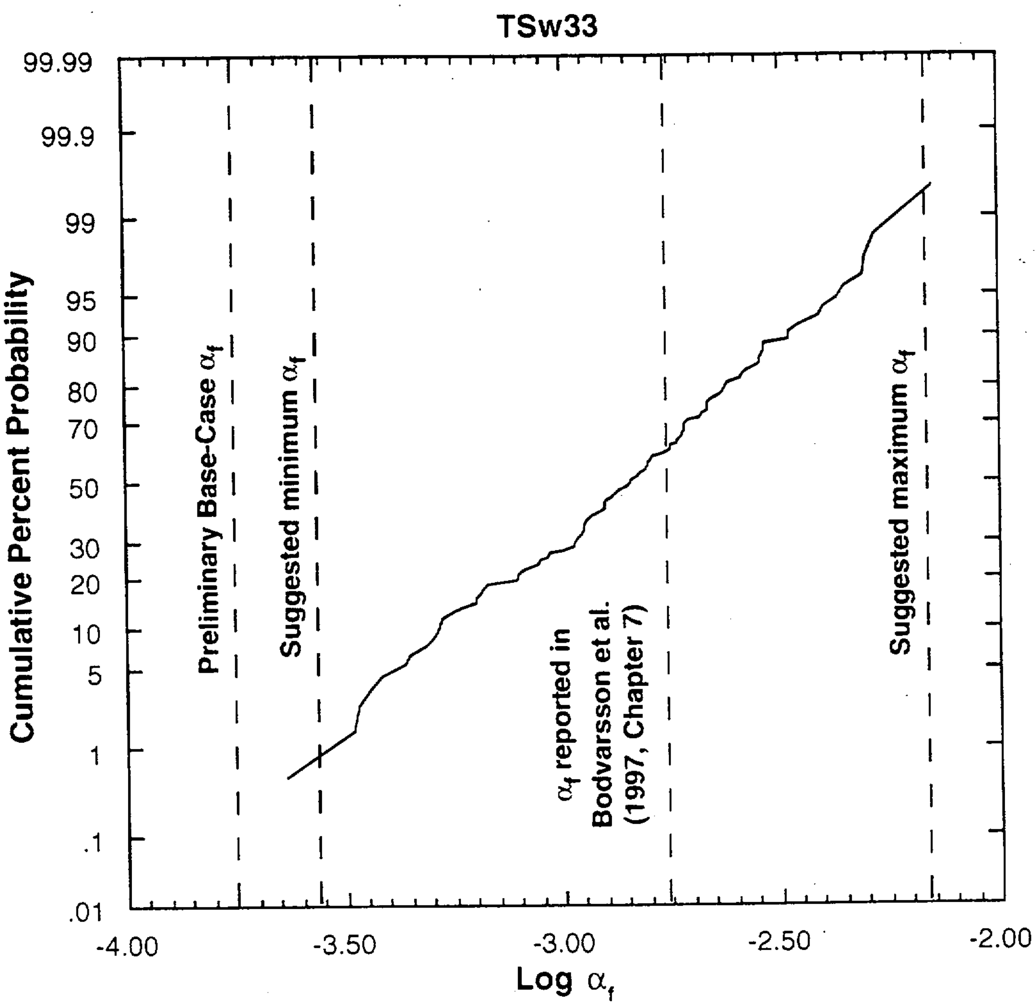

Figure 2-36. Comparison of sampled α_f distribution to the ranges suggested in this section and other reported α_f values for the TSw33 layer.

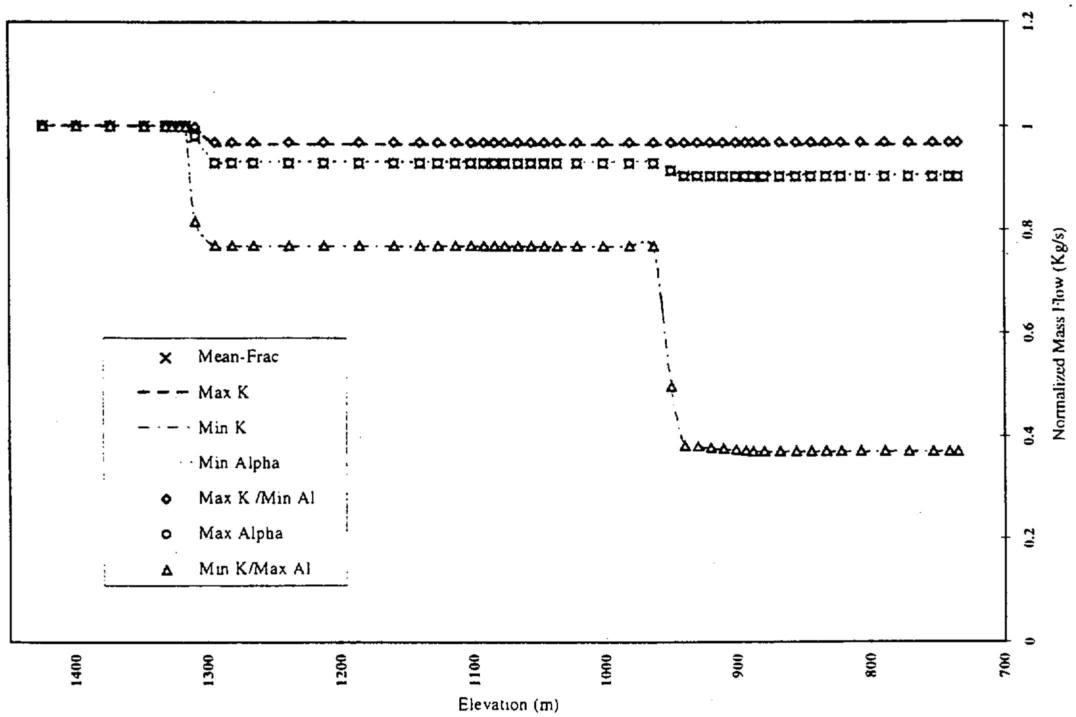

Figure 2-37. Variation of fracture mass flow (normalized to infiltration) with elevation.

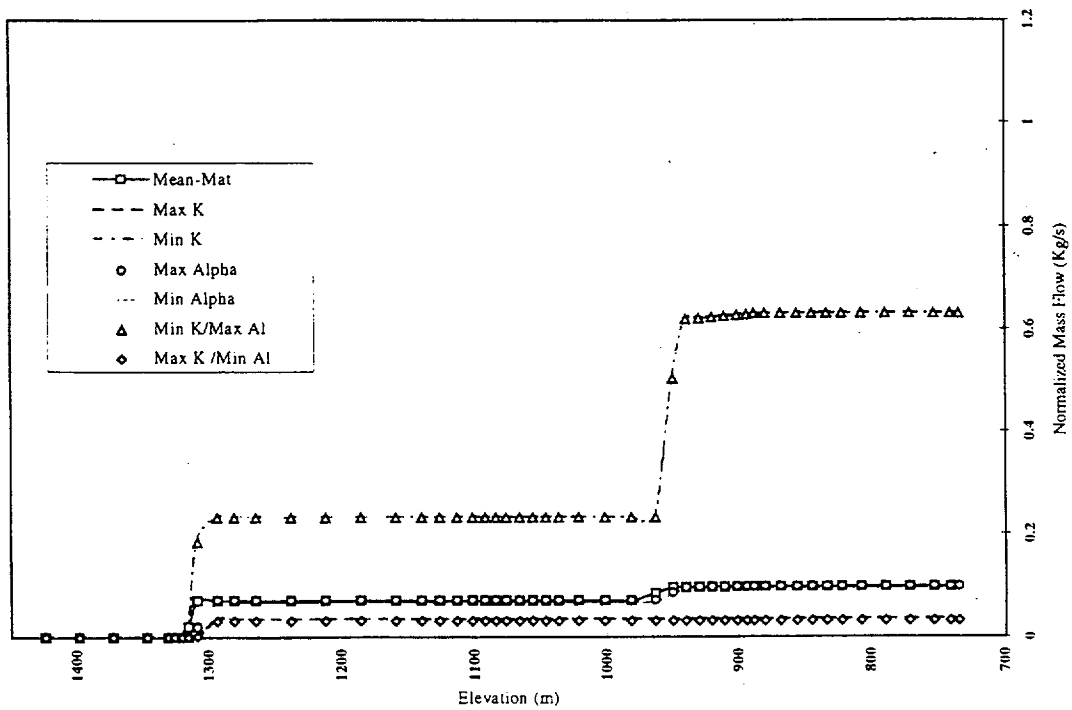

Figure 2-38. Variation of matrix mass flow (normalized to infiltration) with elevation.

Figure 3. Variation of Fracture Pore Water Velocity with Elevation

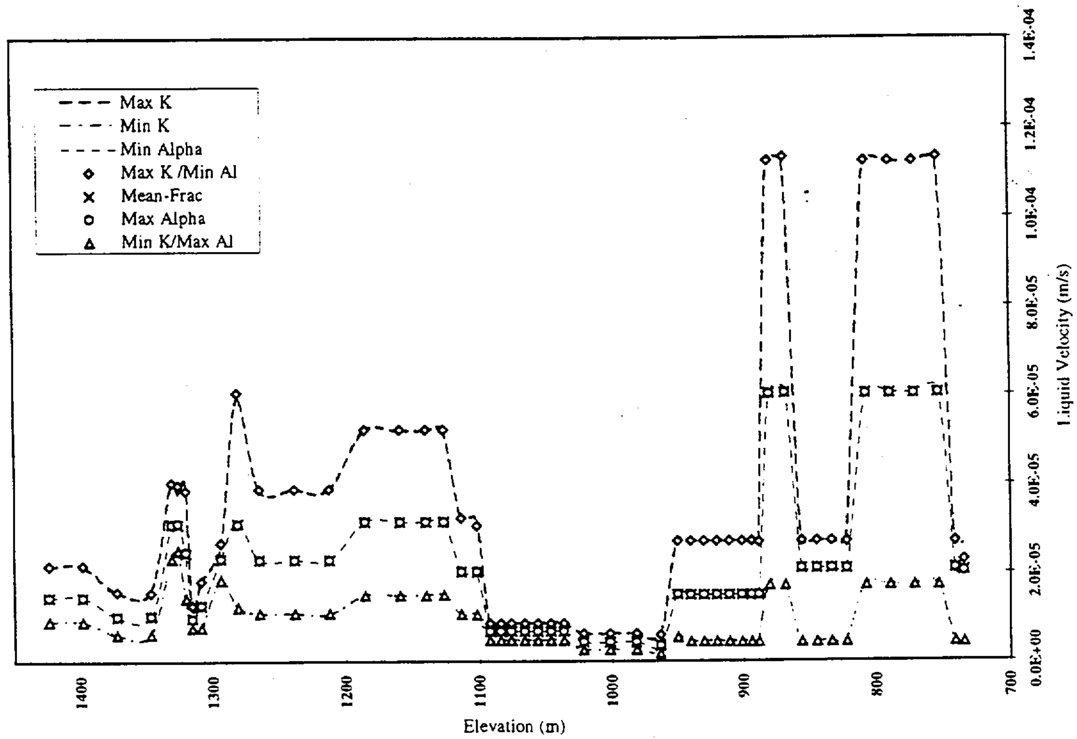

Figure 2-39. Variation of fracture-liquid pore velocity with elevation.

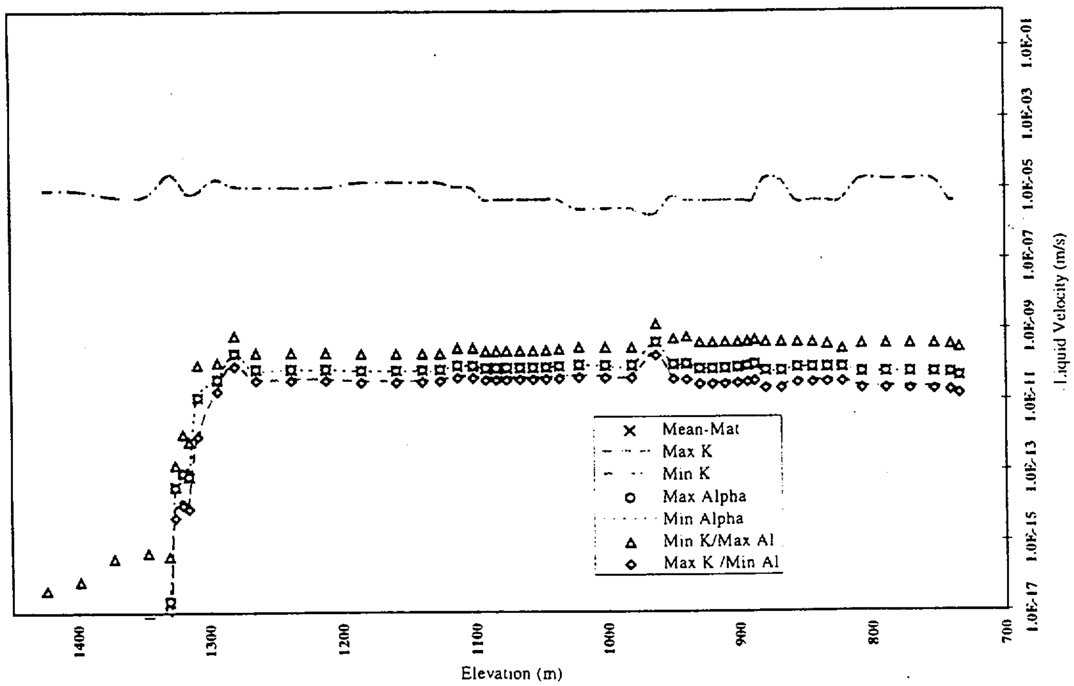

Figure 2-40. Variation of matrix-liquid pore velocity with elevation.

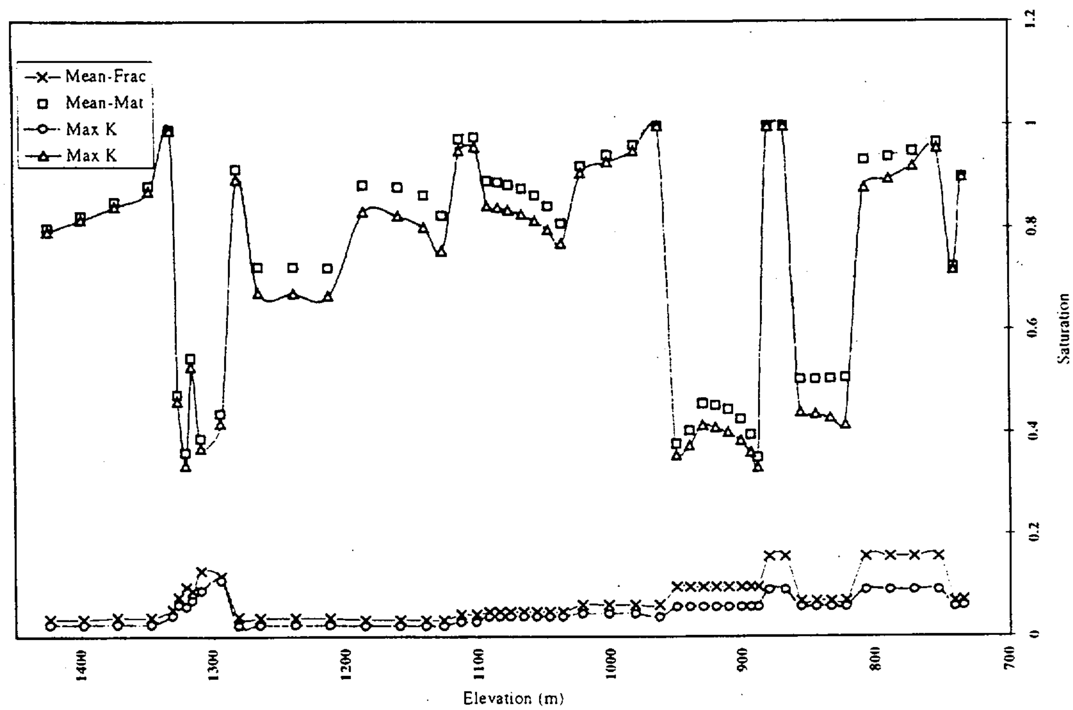

Figure 2-41. Variation of matrix and fracture saturation with elevation for the maximum fracture-permeability case and mean DKM/Weeps case.

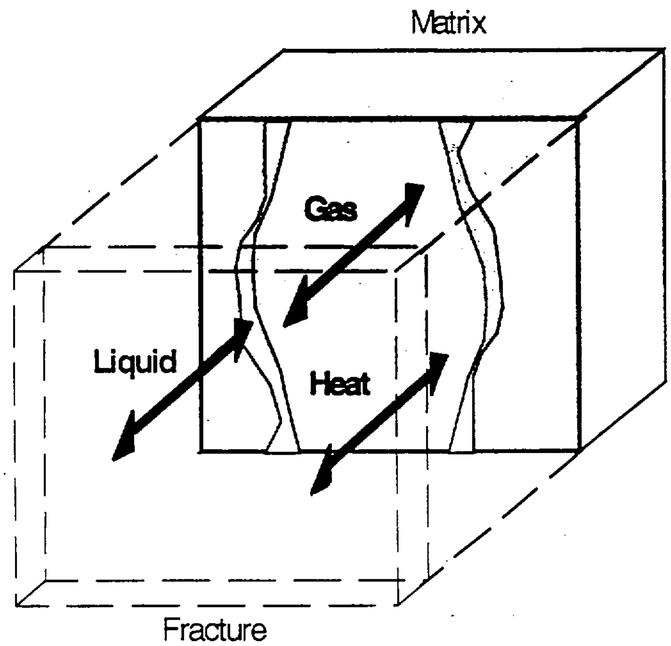

Figure 2-42. Liquid, gas, and heat fluxes between a fracture and a matrix in a DKM.

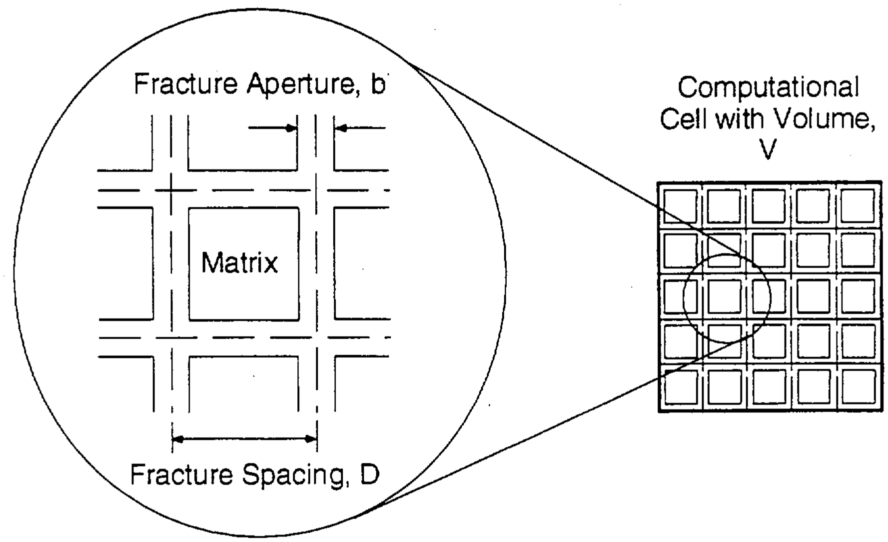

Figure 2-43. Conceptual sketch of fractures and matrix blocks lumped into a computational cell for calculation of the connection area between the fracture and matrix elements in the DKM

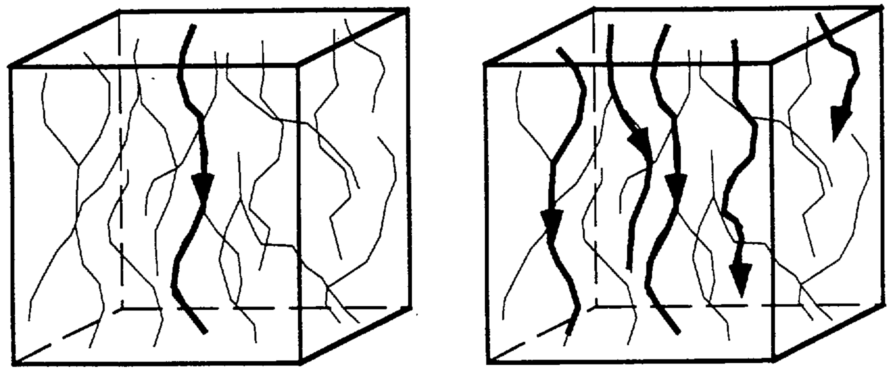

Figure 2-44. Conceptual model of liquid flux through fractures and available wetted area for fracture/matrix liquid flow within a grid block at low-and high-infiltration rates.

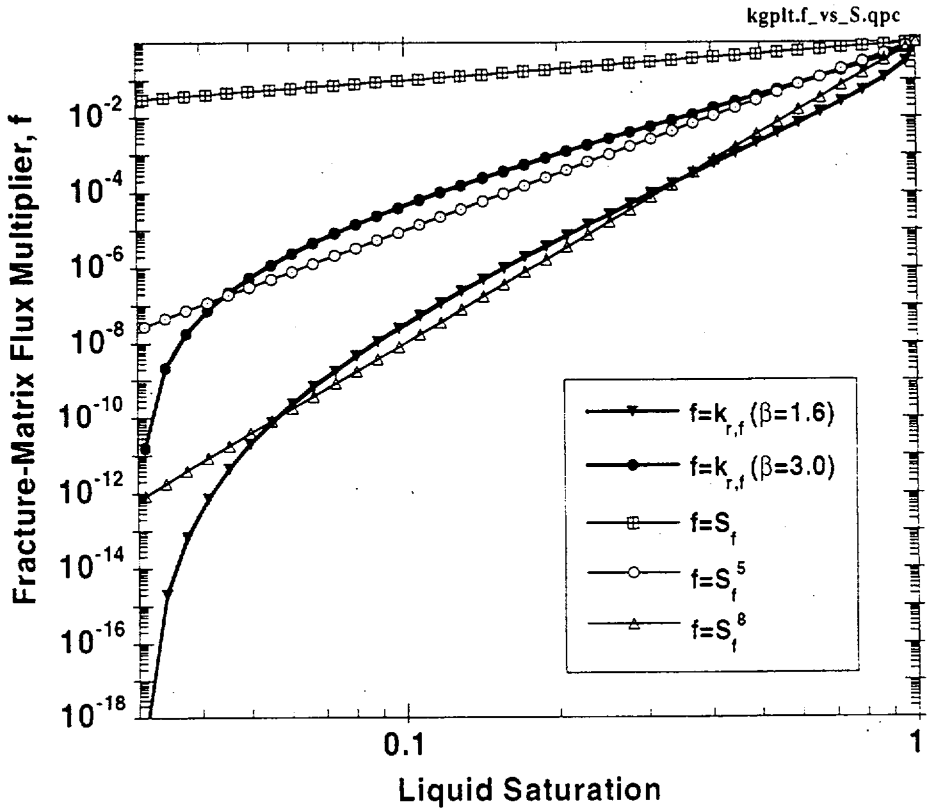

Figure 2-45. Dependence of various fracture-matrix flux multipliers, f, on fracture saturation. The fracture residual liquid saturation is assumed to be 0.03.

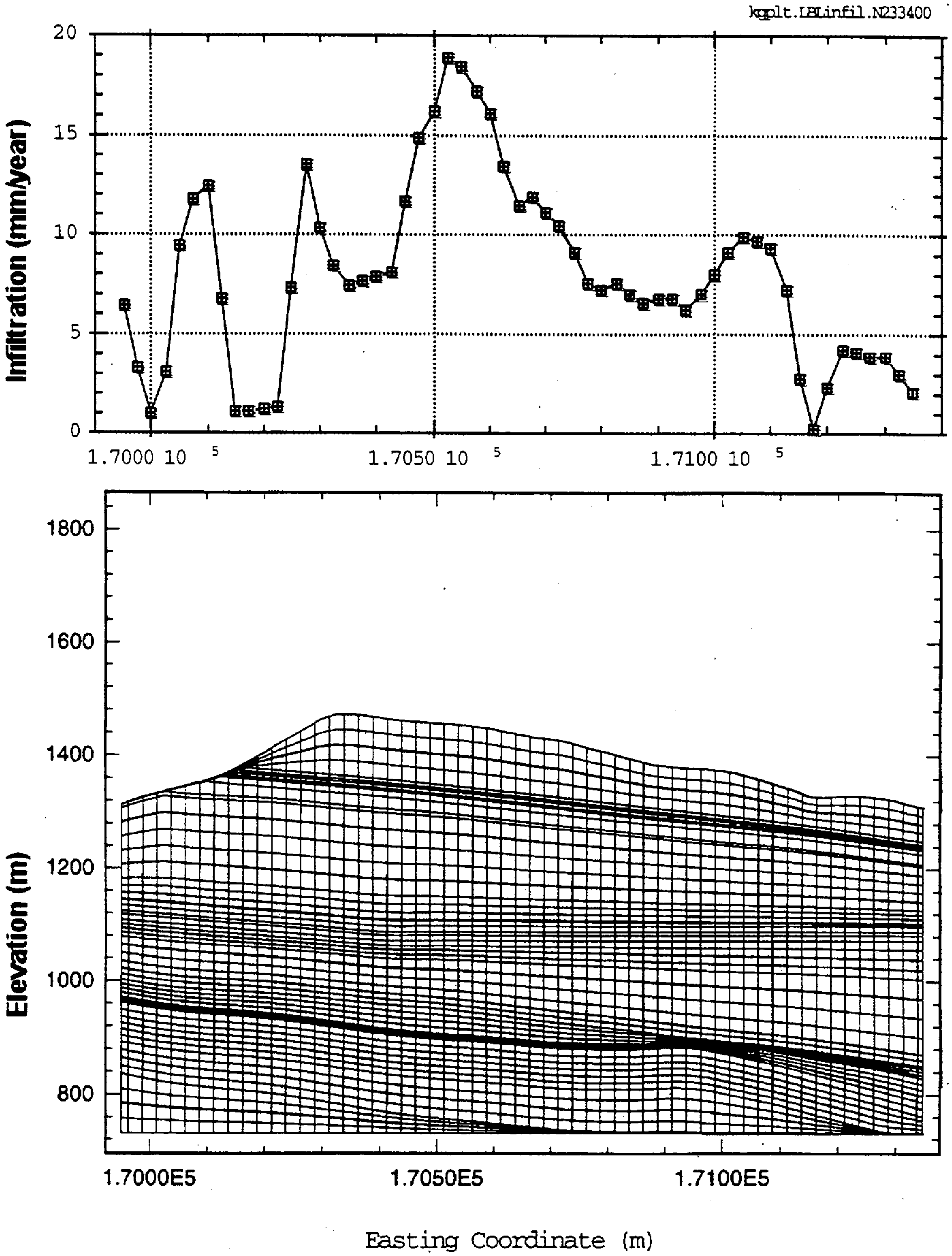

Figure 2-46. Two-dimensional TOUGH2 mesh used in flow simulations with corresponding infiltration distribution. The east-west cross-section has a northing coordinate of 233,400 m. The potential repository is located at an elevation of approximately 1,100 m and bounded by easting coordinates of 170,150 m and 171,200 m.

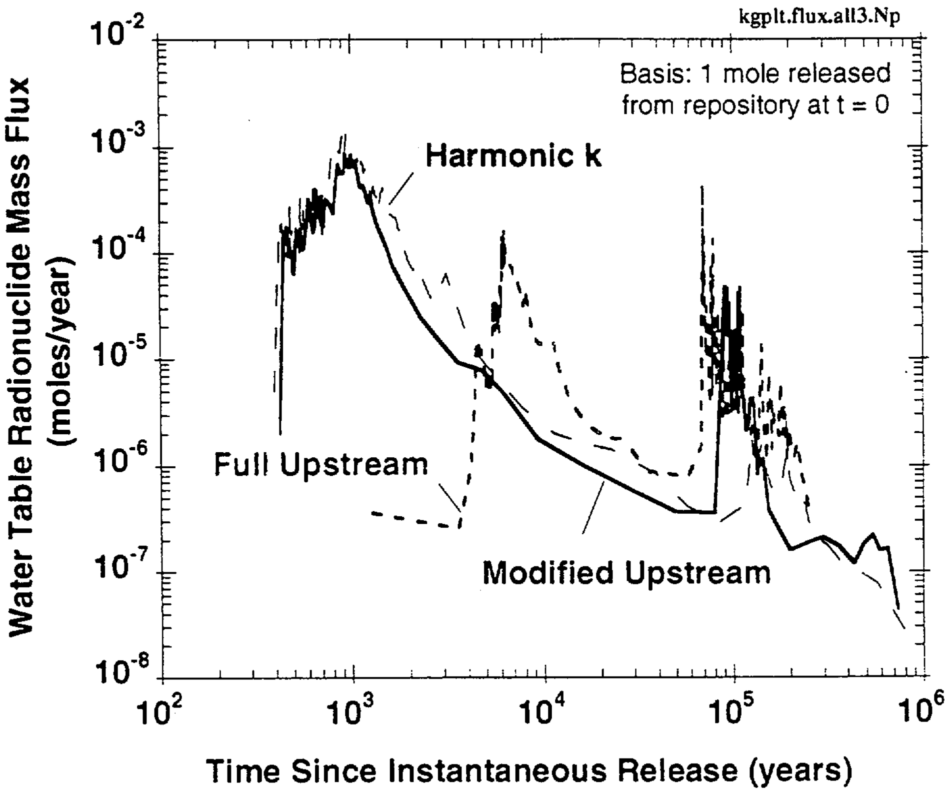

Figure 2-47. Mass flux of ^{237}Np at the water table using different weighting schemes for hydraulic conductivities. TOUGH2 is used to simulate flow fields, and FEHM is used to simulate radionuclide transport.

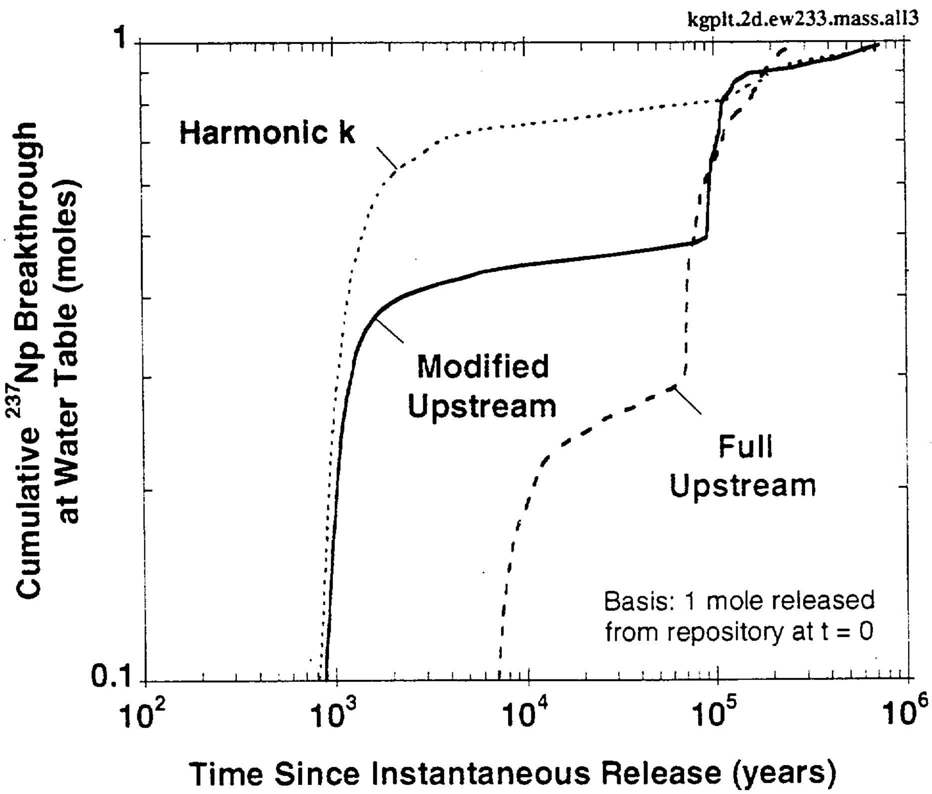

Figure 2-48. Cumulative breakthrough of ^{237}Np at the water table using different weighting schemes for hydraulic conductivities. TOUGH2 is used to simulate flow fields, and FEHM is used to simulate radionuclide transport.

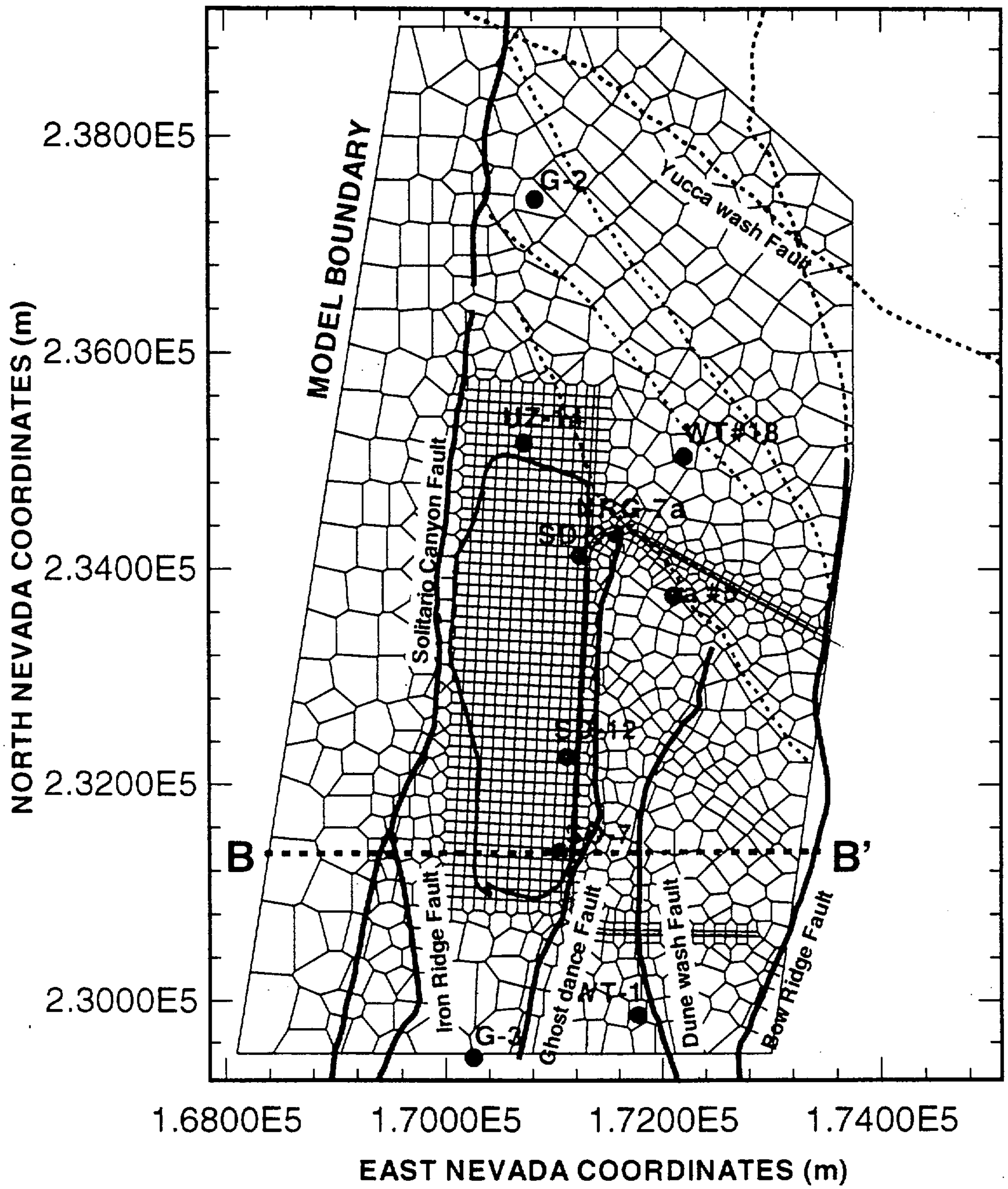

Figure 2-49. A plan view of the 3-D, site-scale, UZ-flow model domain, grid, incorporated faults, and locations of boreholes.

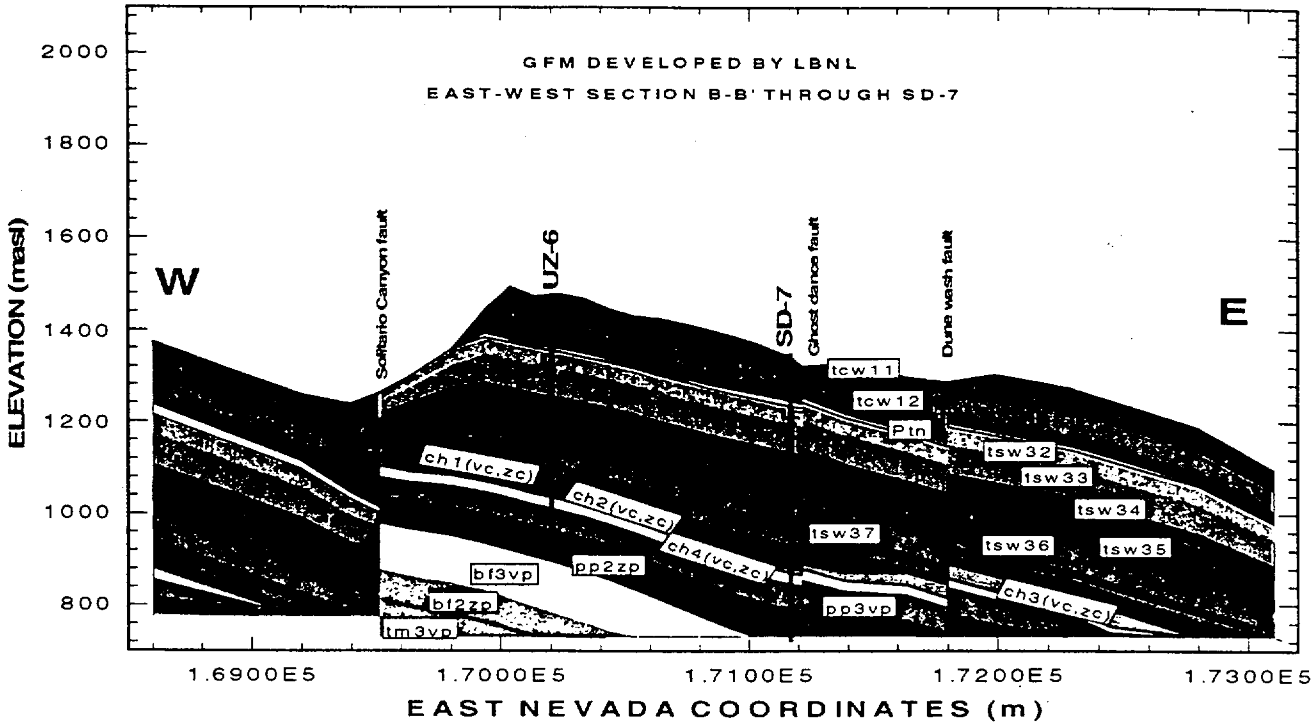

Figure 2-50. East-west vertical cross-section along SD-7 (B-B' in Figure 2-49) showing stratigraphy and faults used in the development of the 3-D, site-scale, UZ-flow model.

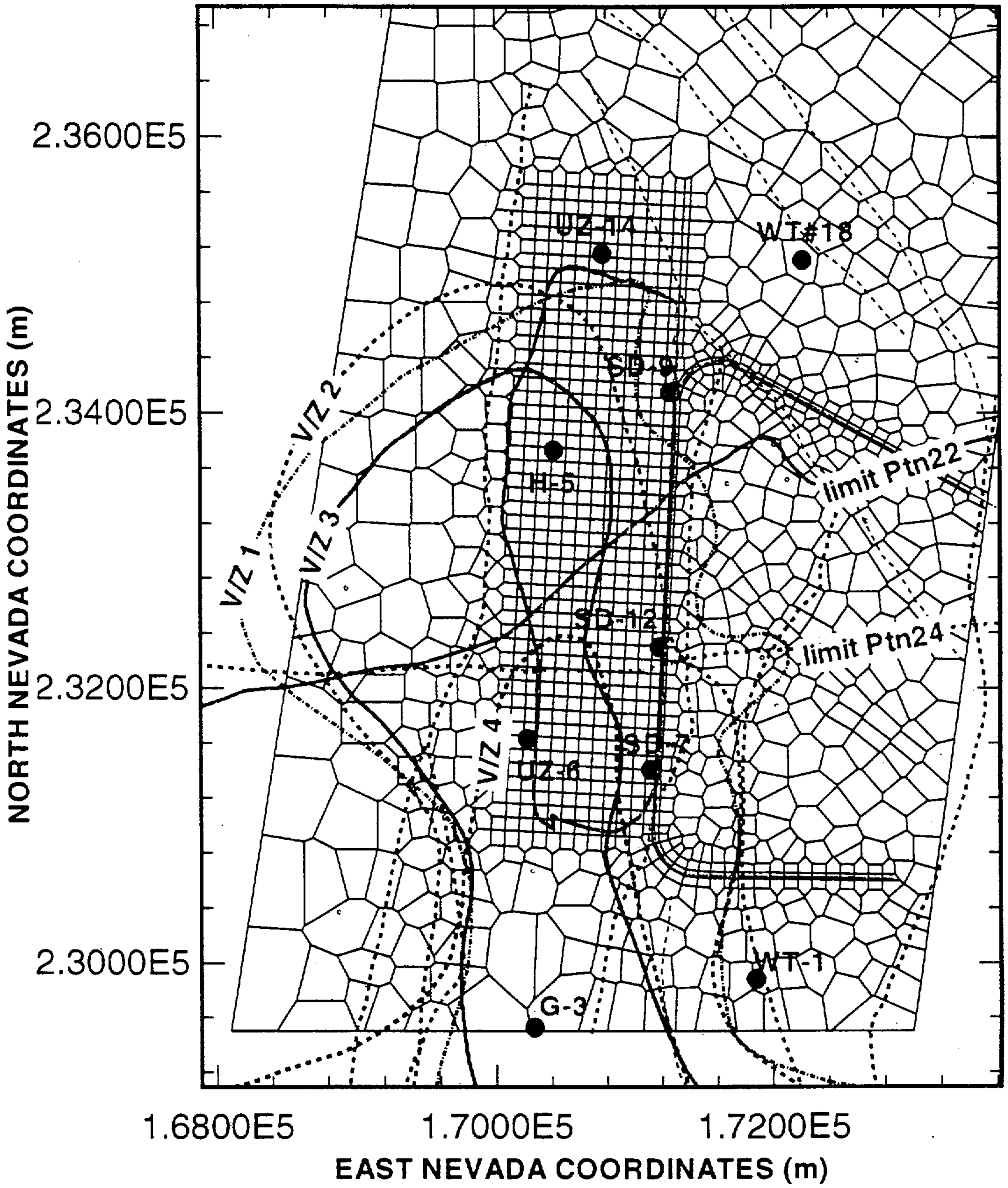

Figure 2-51. Material transition boundaries for the pinchout layers in the Paintbrush and the Vitric/Zeolitic interface in Calico Hills.

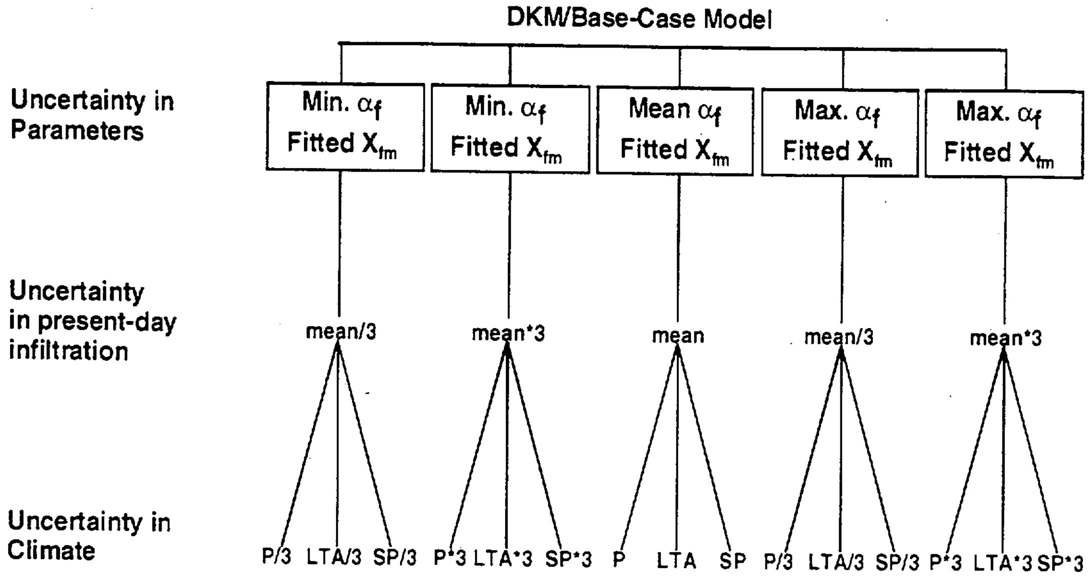

Figure 2-52. Tree-diagram of fifteen base-case, UZ-flow fields generated by LBNL for TSPA-VA. Five different property sets were calibrated for the present-day infiltration scenarios.

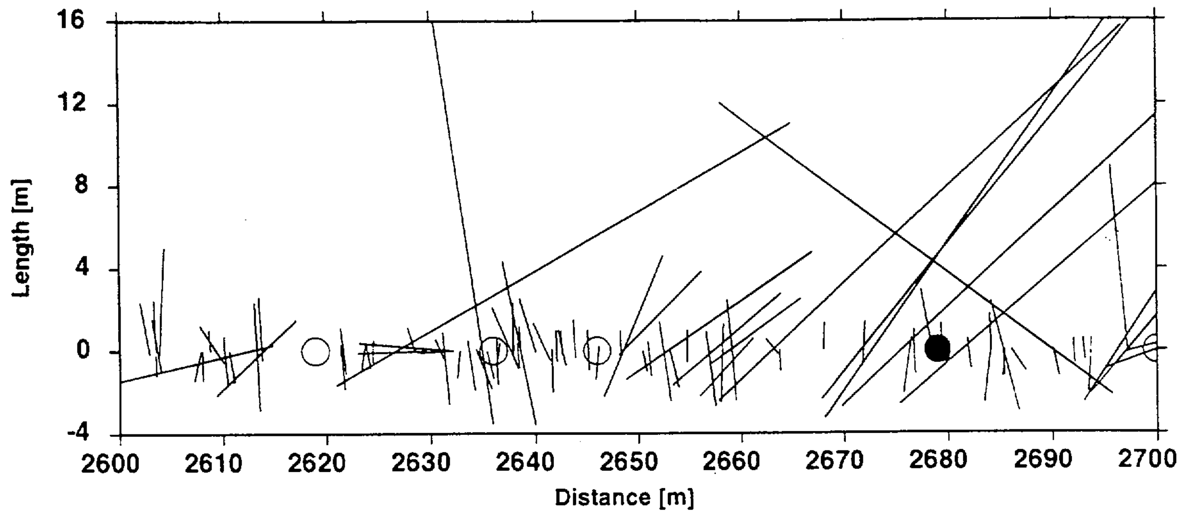

Figure 2-53. Fracture location and dip along the DLS line from 26+00 to 27+00 in the ESF. Closed circles indicate samples that contained bomb pulse (elevated ^{36}Cl) and open circles indicate samples that were below the bomb pulse (taken from Bodvarsson et al., 1997 [Chapter 7]).

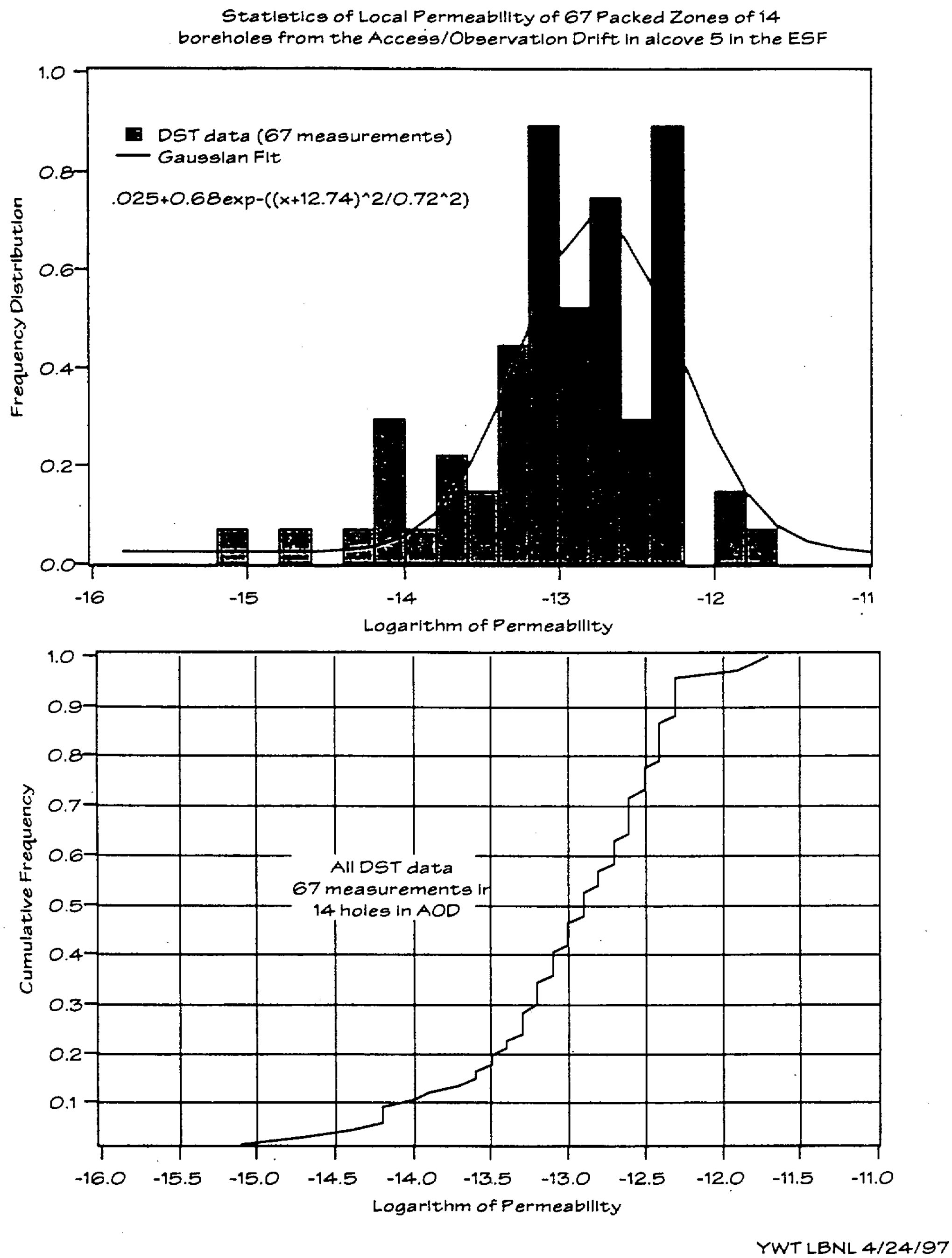

Figure 2-54. Probability distribution of log permeability (m^2) based on air permeability testing in the DST block (Tsang and Cook, 1997). The cumulative distribution is shown in the lower part of the figure.

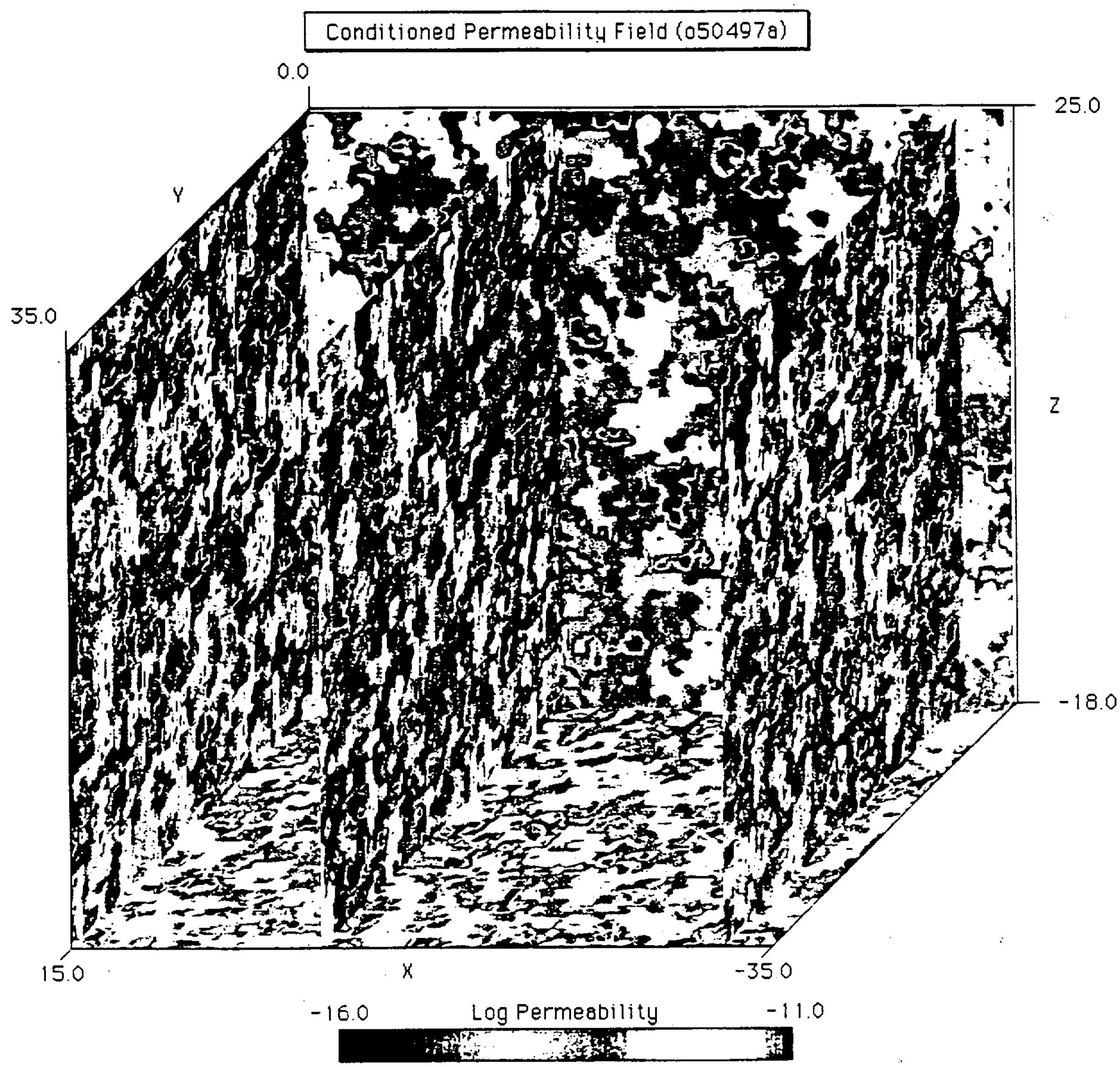

Figure 2-55. Conditioned, stochastic, fracture continuum model. The x-axis corresponds to the NS-direction, and the y-axis corresponds to the EW-direction.

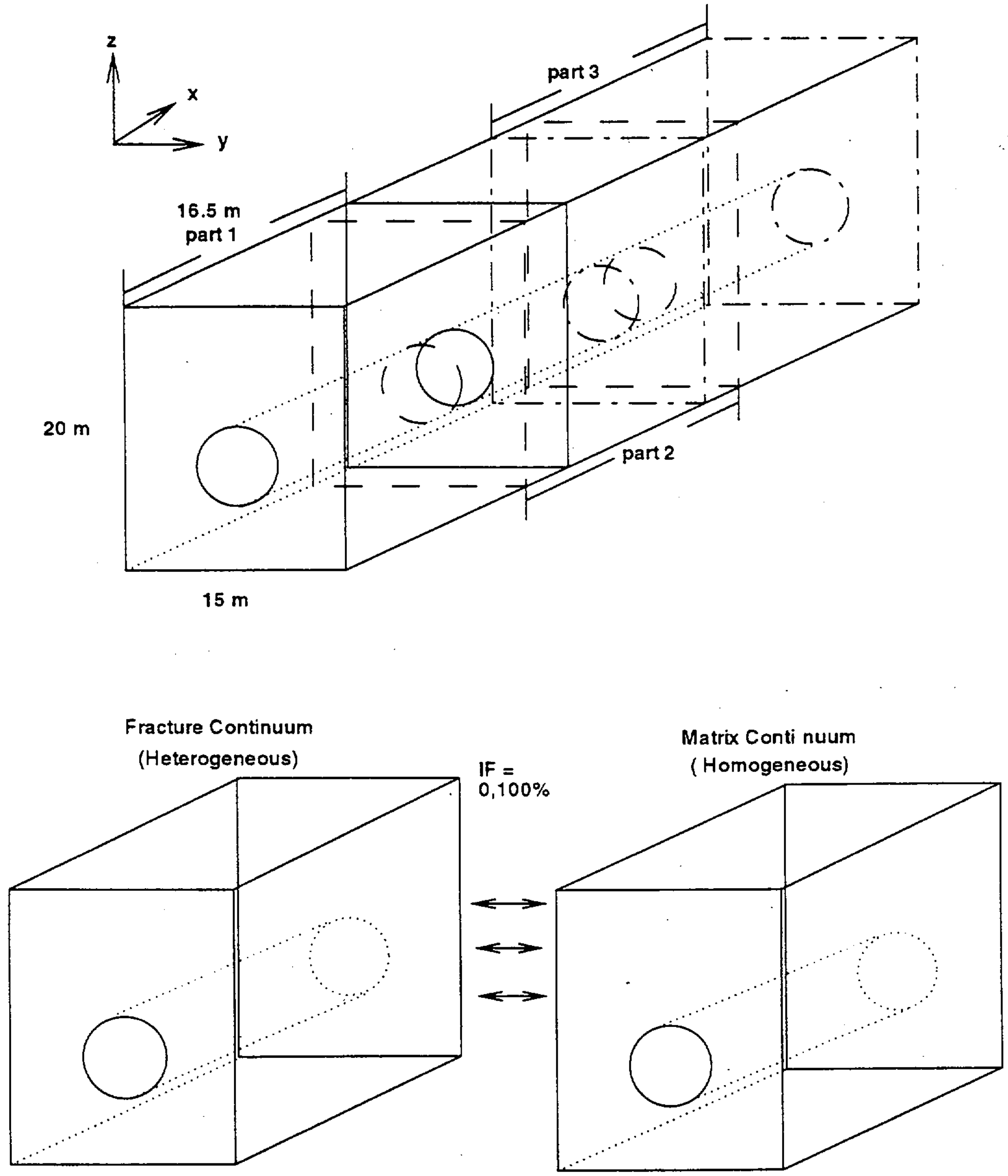

Figure 2-56. Schematic diagram showing three 3-D parts comprising the 3-D block and the DKM conceptualization. The x-axis corresponds to the NS direction, the y-axis to the EW direction, and the z-axis to the vertical direction.

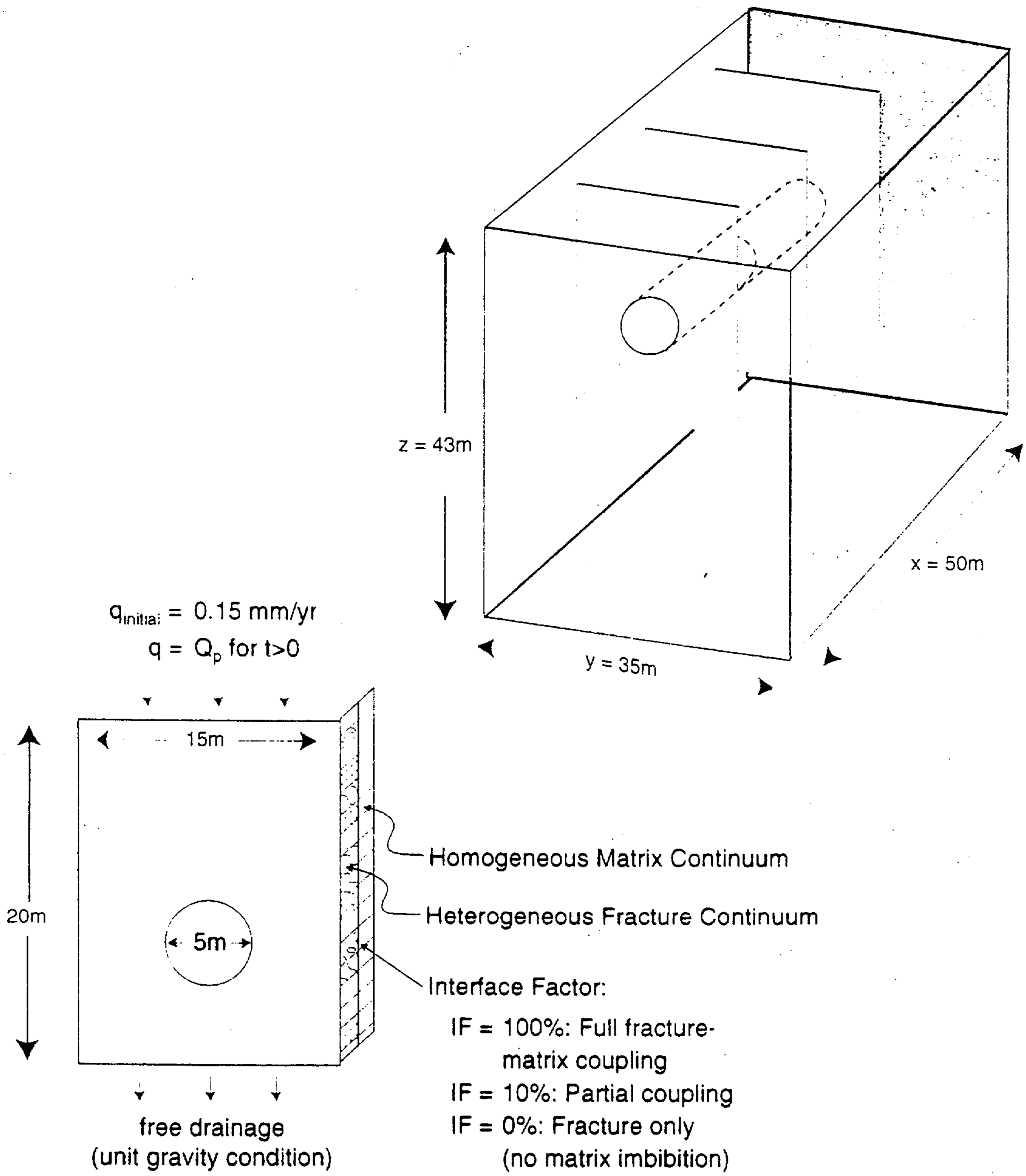

Figure 2-57. Schematic diagram showing the vertical slices and the boundary conditions. The x-axis corresponds to the NS direction, and the y-axis corresponds to the EW direction.

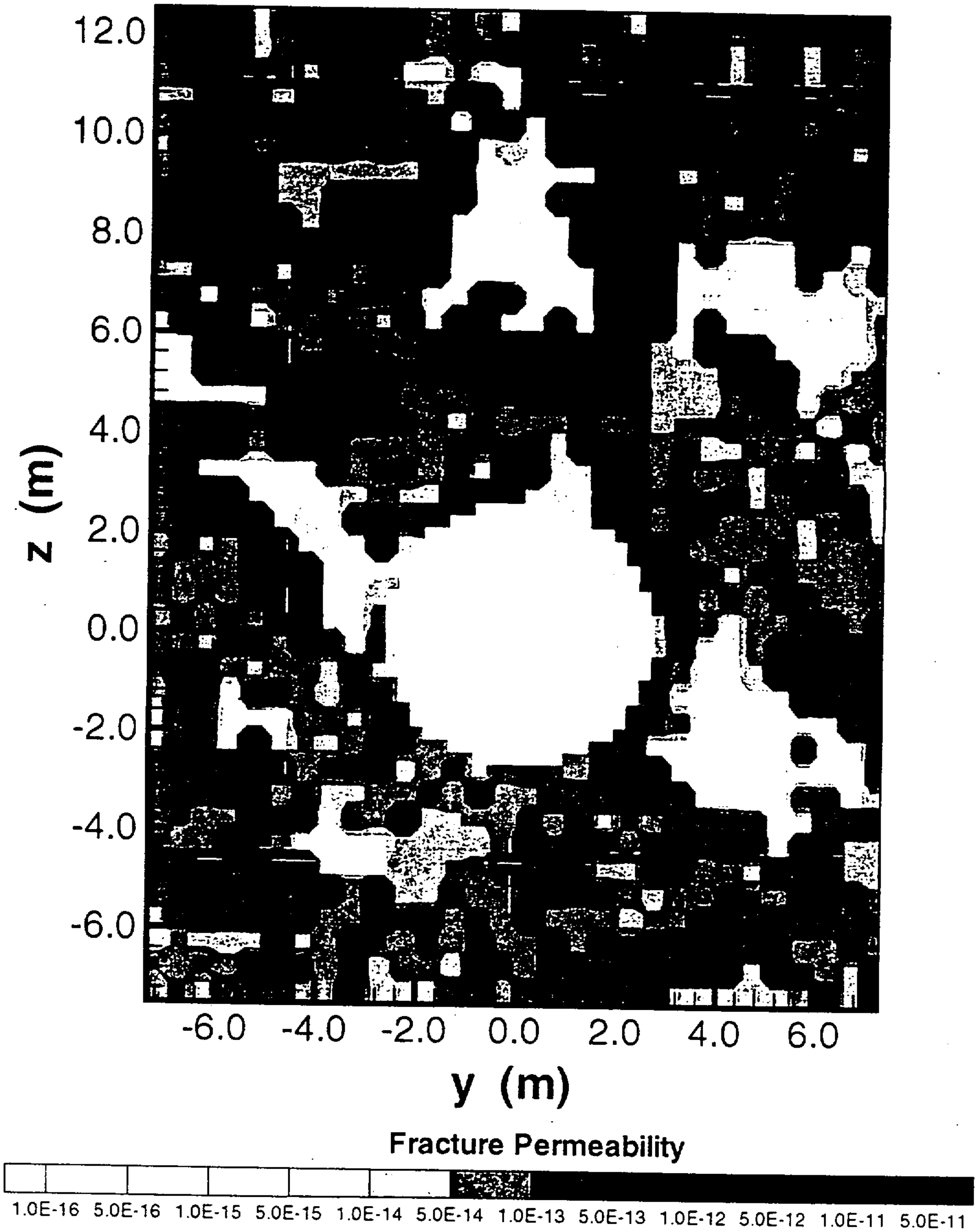

Figure 2-58a. Heterogeneous-permeability field for vertical slice 1 of the 3-D block.

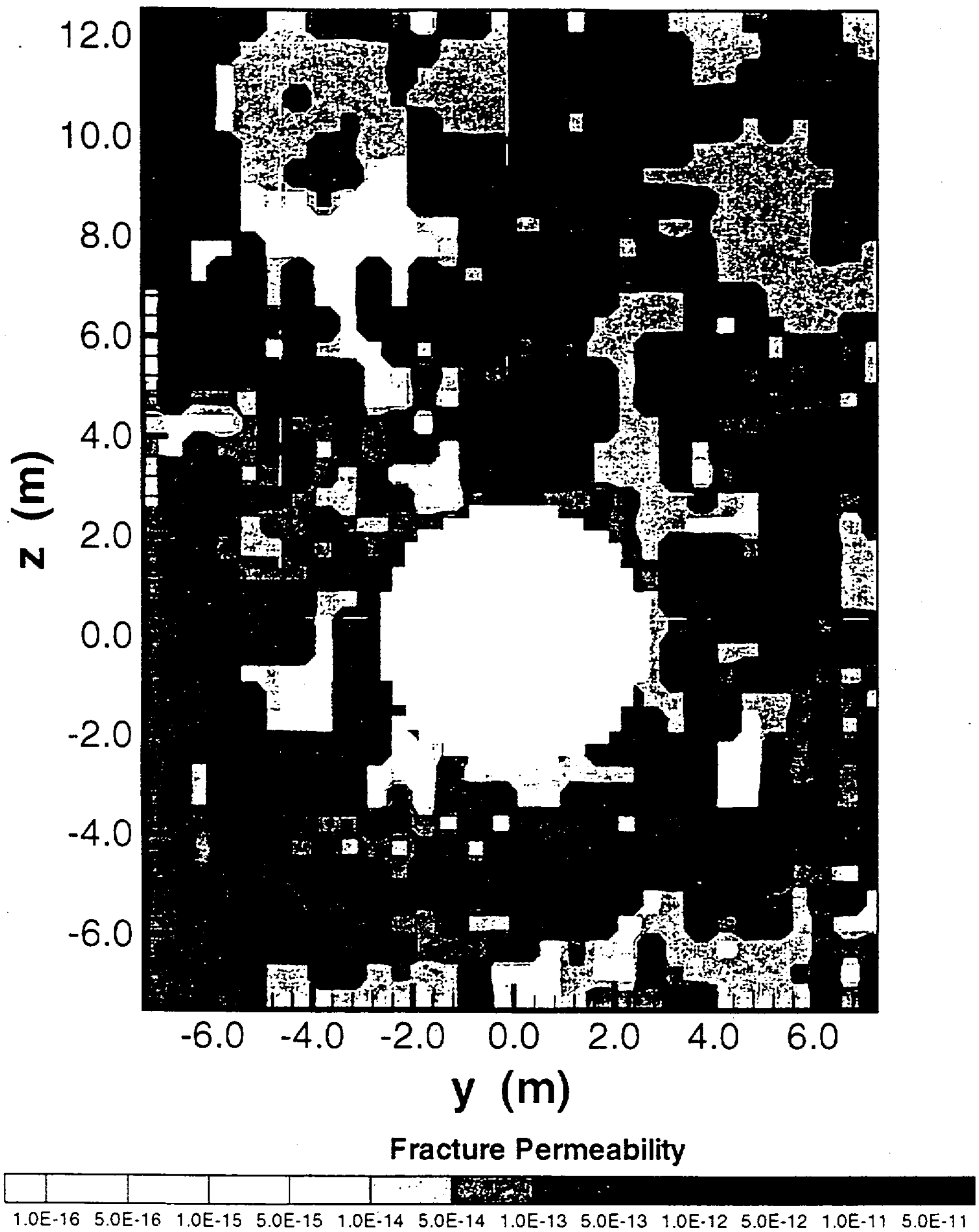

Figure 2-58b. Heterogeneous-permeability field for vertical slice 2 of the 3-D block.

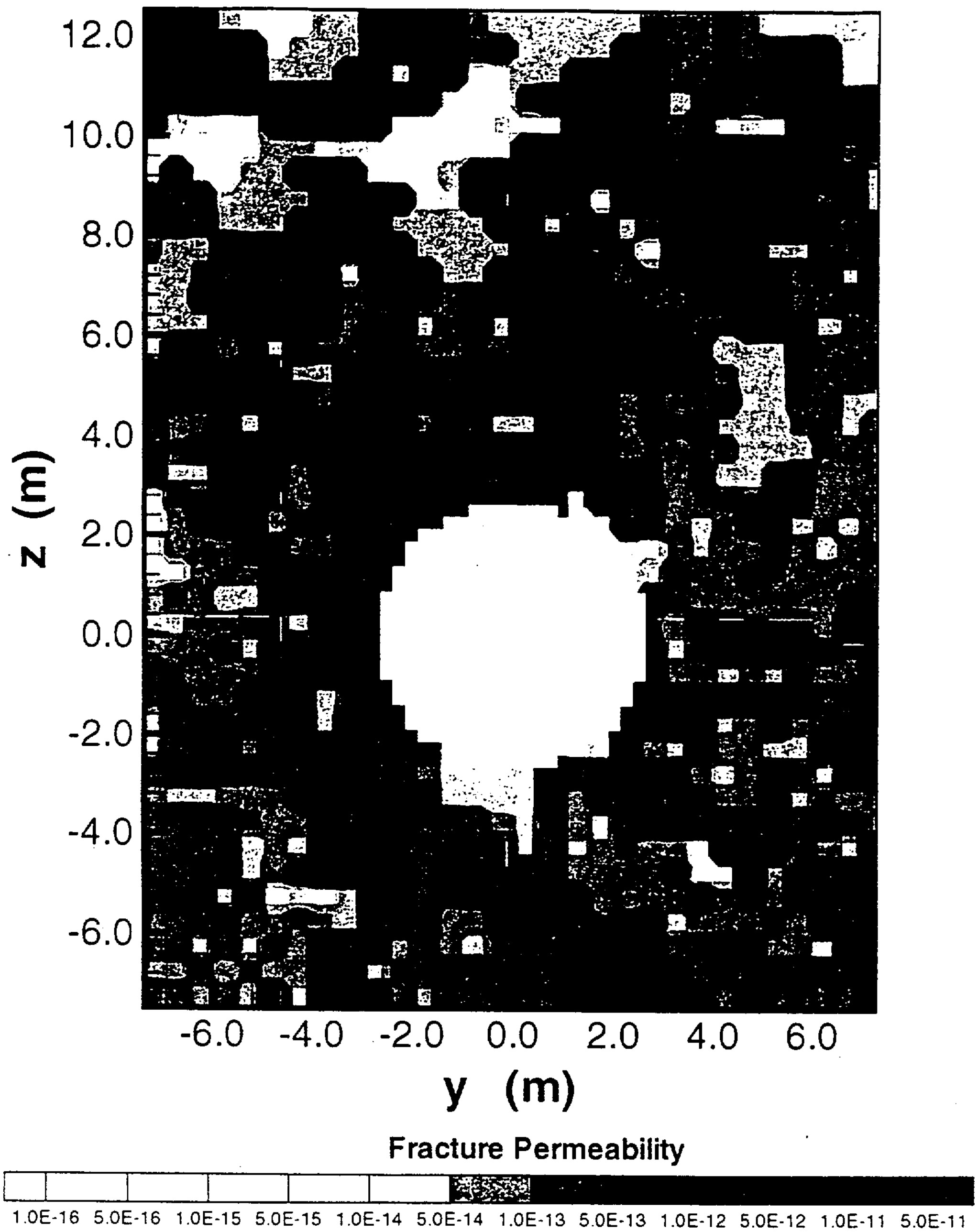

Figure 2-58c. Heterogeneous-permeability field for vertical slice 3 of the 3-D block.

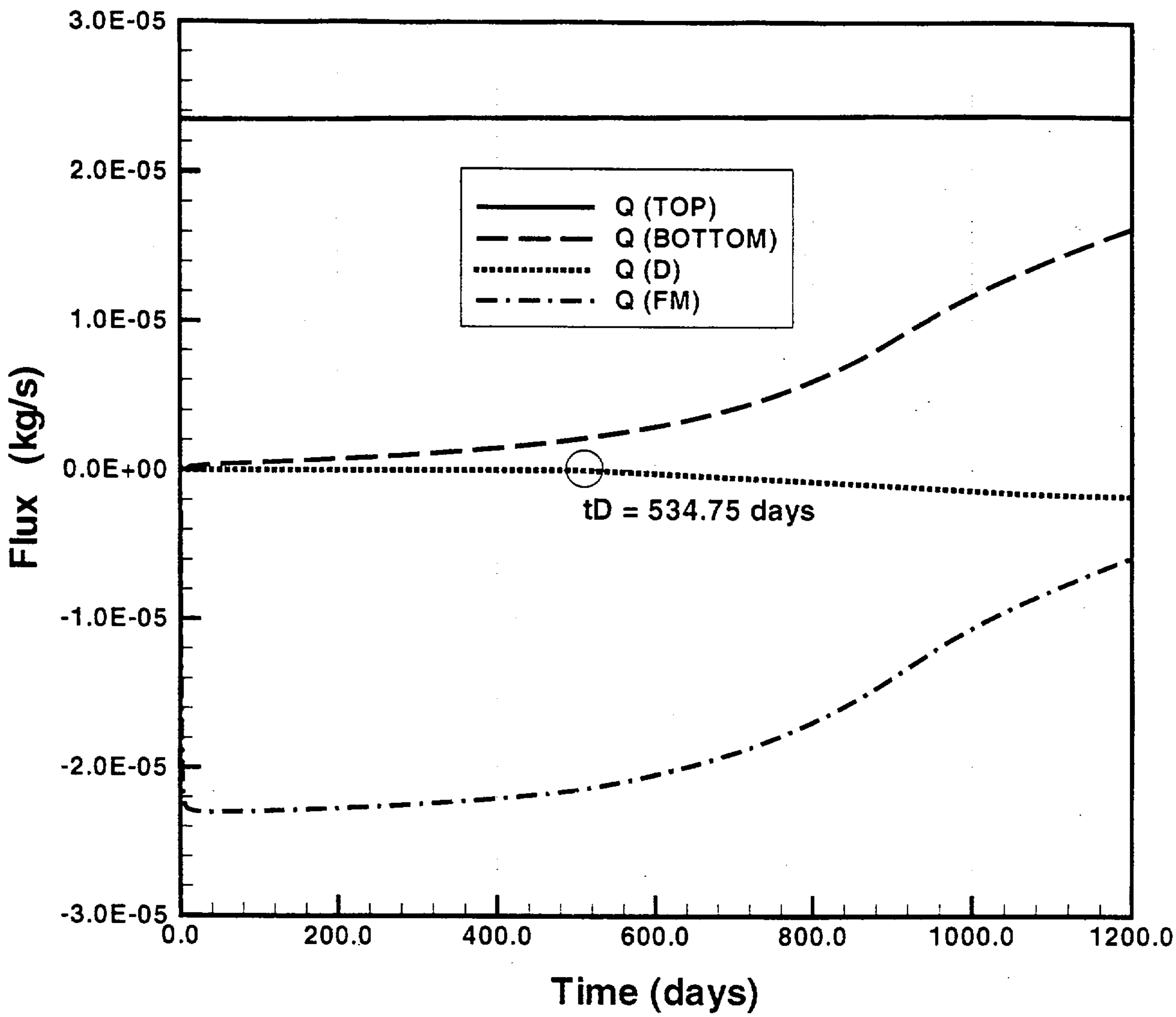

Figure 2-59a. Q_{Top}, Q_{Bottom}, Q_D and Q_{FM} as a function of time for slice 1 of the 3-D block, Q_p = 50 mm/yr and IF = 100%. Q_D and Q_{FM} are plotted as negative values for clarity in presentation.

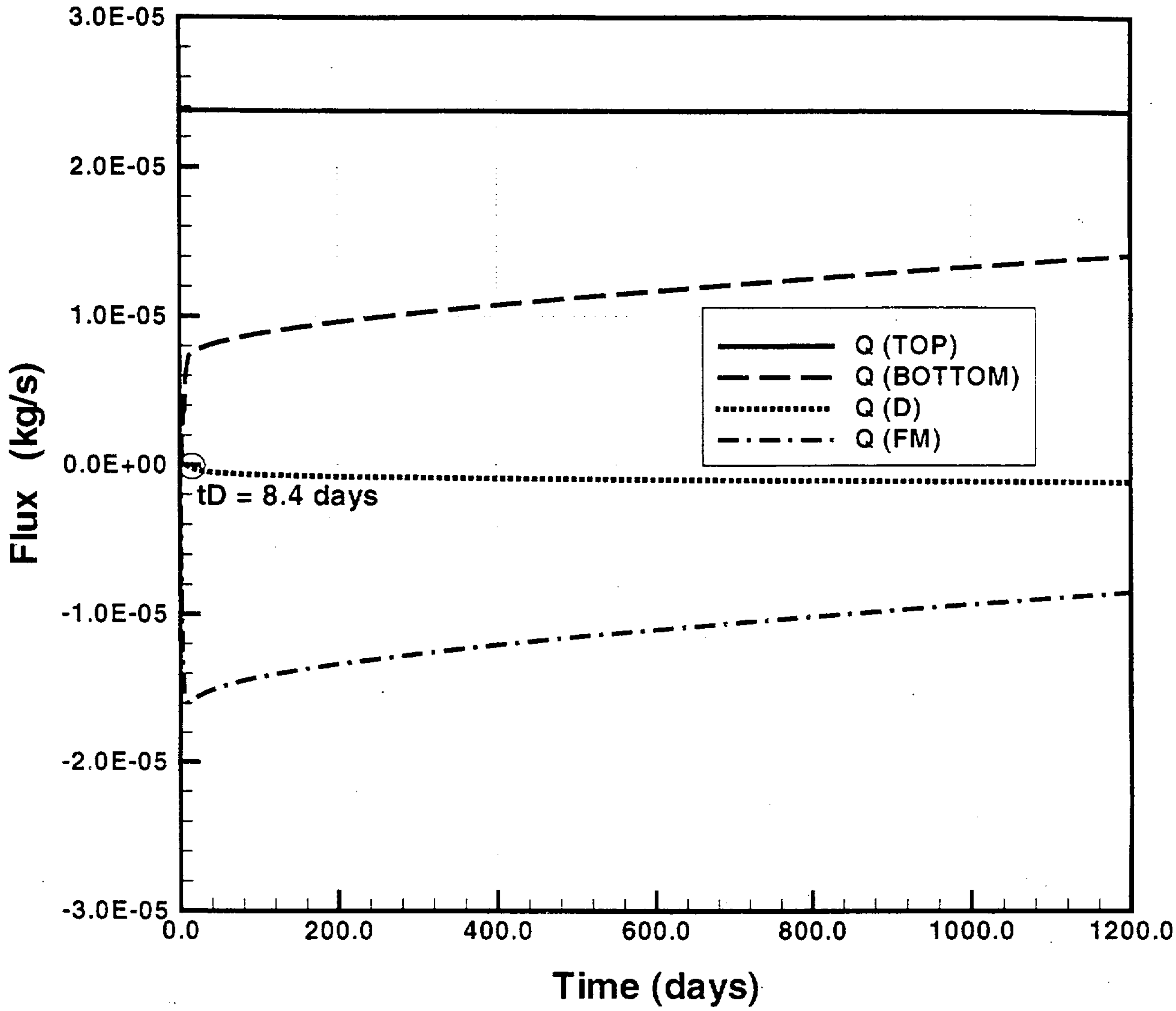

Figure 2-59b. Q_{Top}, Q_{Bottom}, Q_D and Q_{FM} as a function of time for slice 1 of the 3-D block, Q_p = 50 mm/yr and IF = 10%. Q_D and Q_{FM} are plotted as negative values for clarity in presentation.

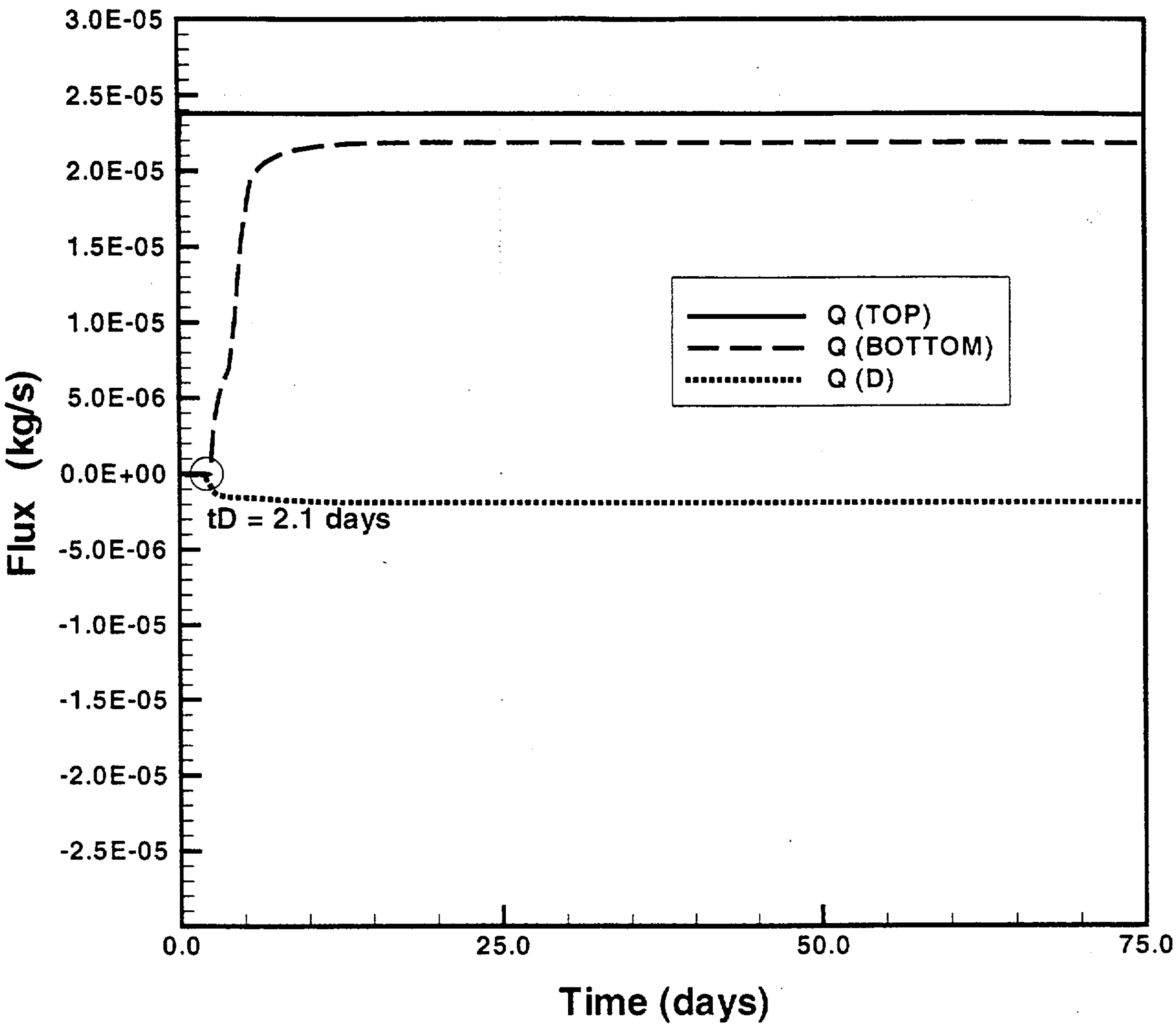

Figure 2-59c. Q_{Top}, Q_{Bottom}, Q_D and Q_{FM} as a function of time for slice 1 of the 3-D block, Q_p = 50 mm/yr and IF = 0%. Q_D and Q_{FM} are plotted as negative values for clarity in presentation.

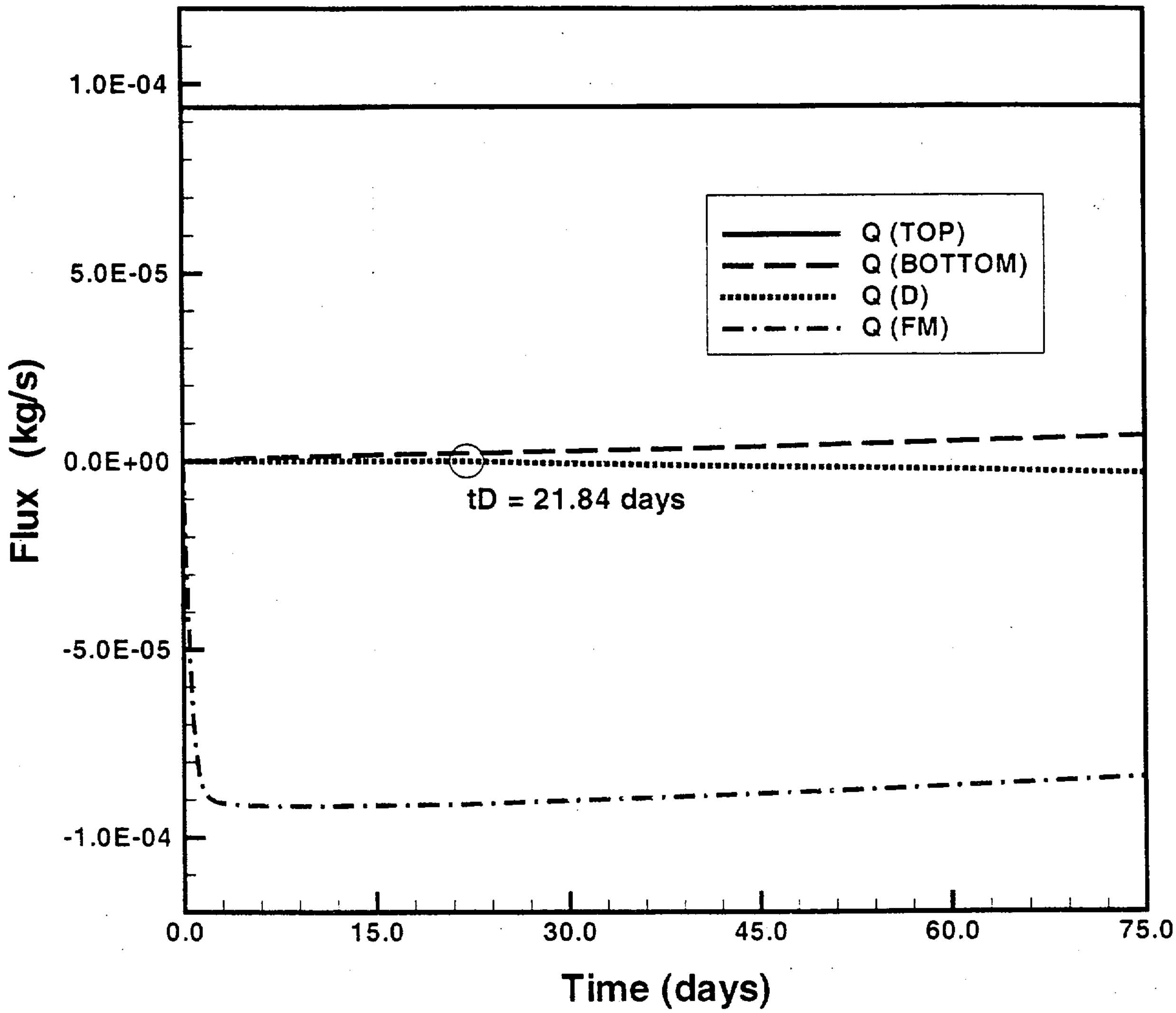

Figure 2-60a. Q_{Top}, Q_{Bottom}, Q_D and Q_{FM} as a function of time for slice 1 of the 3-D block, Q_p = 200 mm/yr and IF = 100%. Q_D and Q_{FM} are plotted as negative values for clarity in presentation.

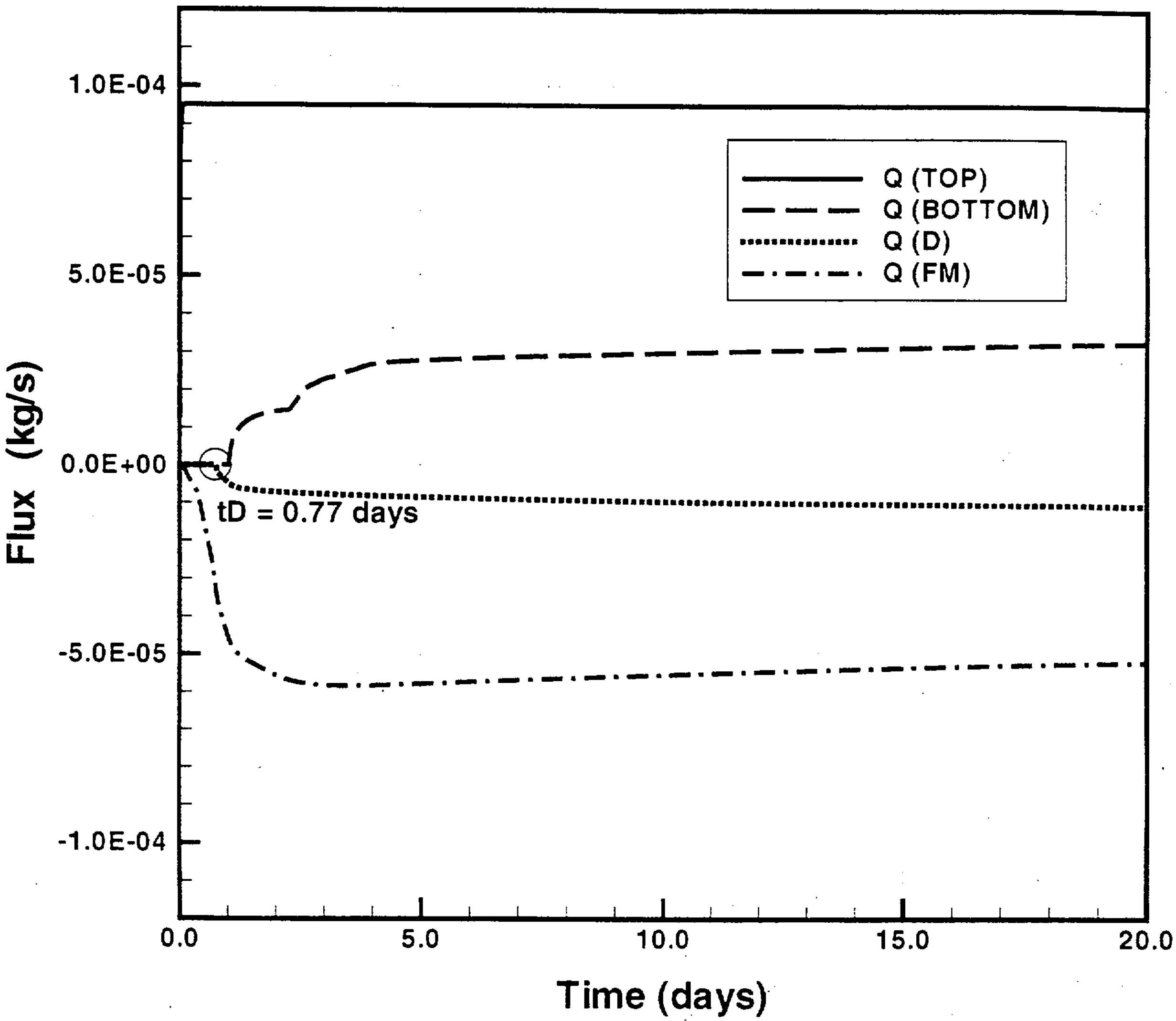

Figure 2-60b. Q_{Top}, Q_{Bottom}, Q_D and Q_{FM} as a function of time for slice 1 of the 3-D block, Q_p = 200 mm/yr and IF = 10%. Q_D and Q_{FM} are plotted as negative values for clarity in presentation.

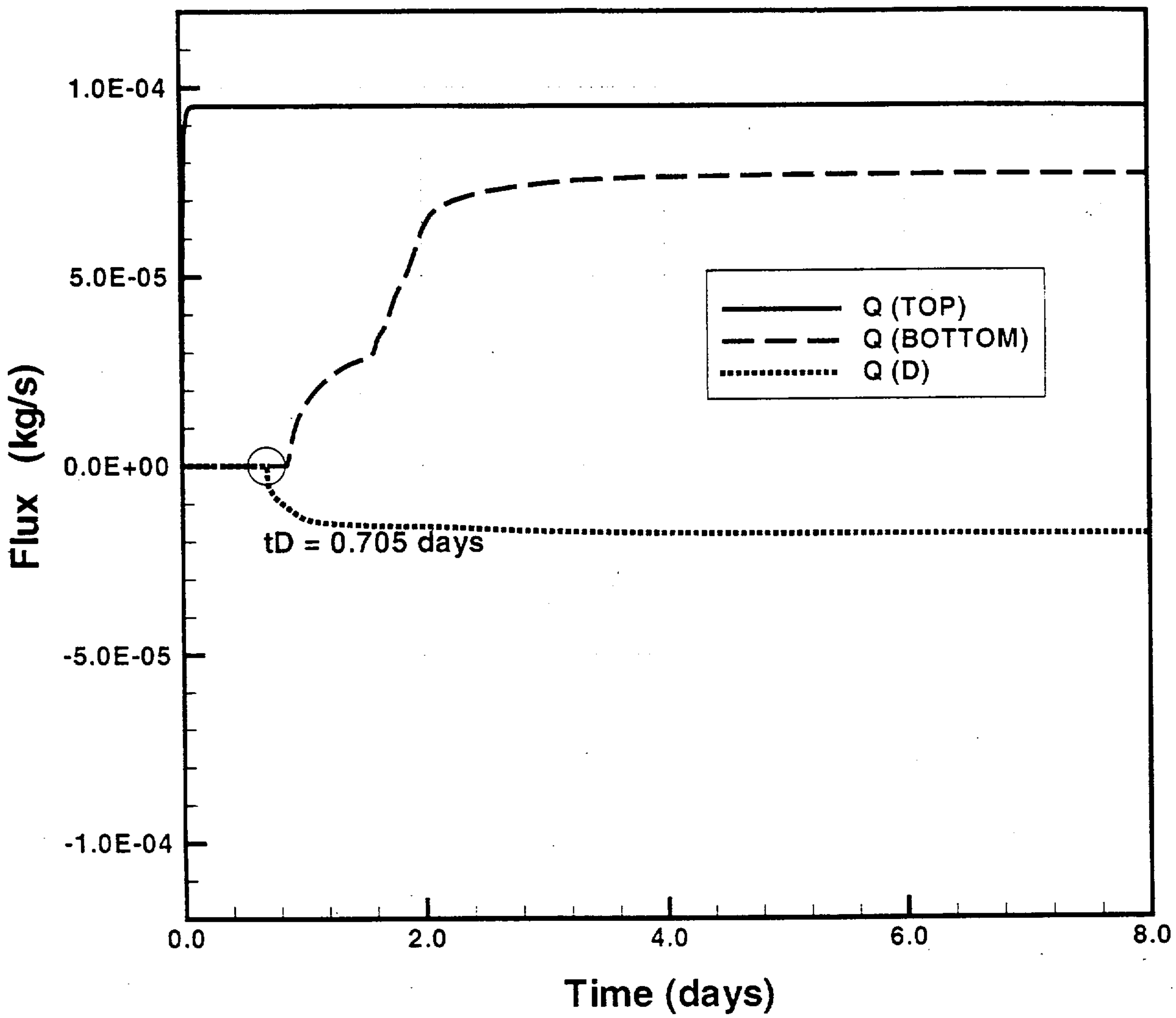

Figure 2-60c. Q_{Top}, Q_{Bottom}, Q_D and Q_{FM} as a function of time for slice 1 of the 3-D block, Q_p = 200 mm/yr and IF = 0%. Q_D and Q_{FM} are plotted as negative values for clarity in presentation.

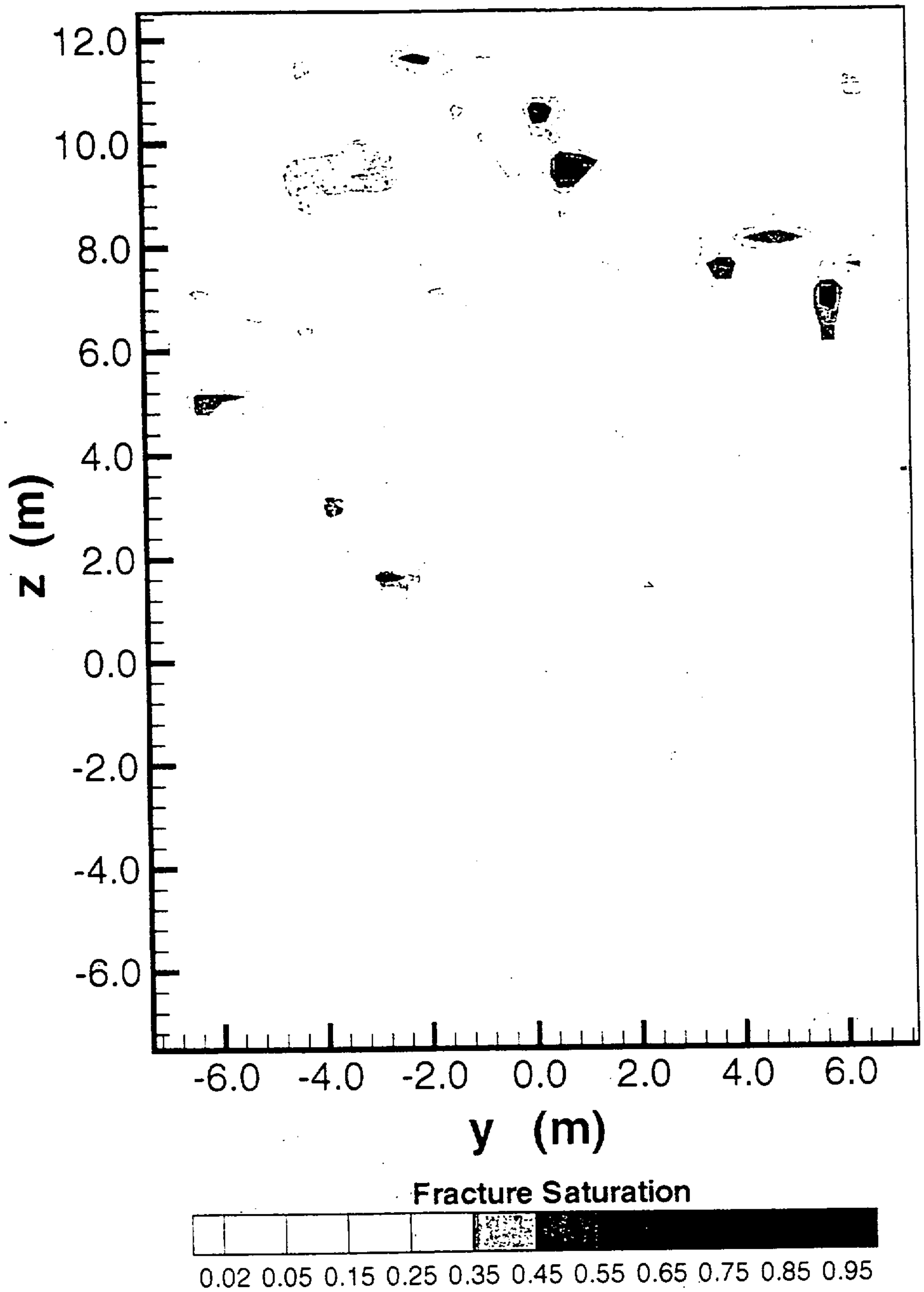

Figure 2-61a. Saturation contours in fracture continuum on slice 1 of the 3-D block for Q_p = 50 mm/yr and IF = 100% at t = 5 days.

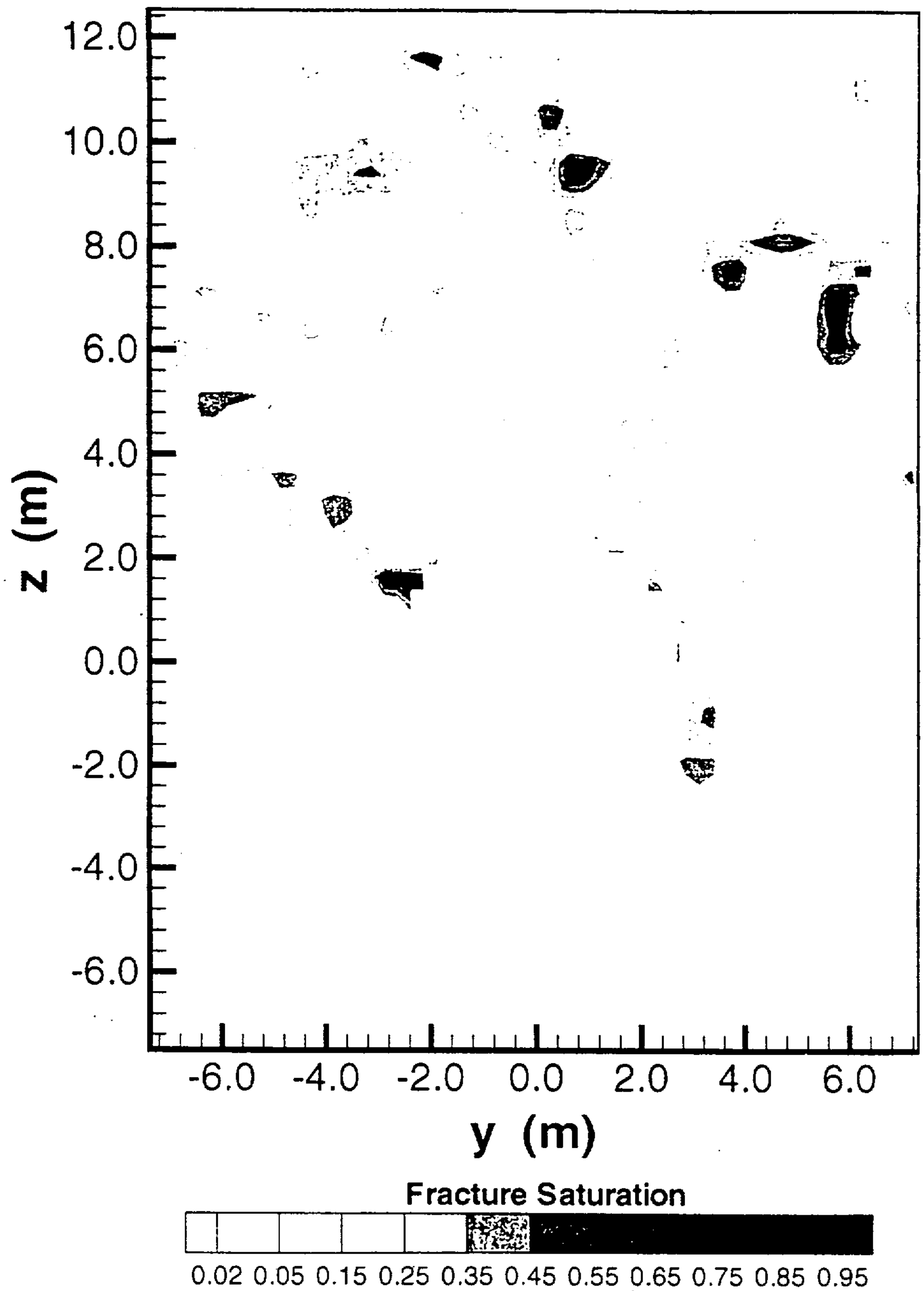

Figure 2-61b. Saturation contours in fracture continuum on slice 1 of the 3-D block for Q_p = 50 mm/yr and IF = 100% at t = 100 days.

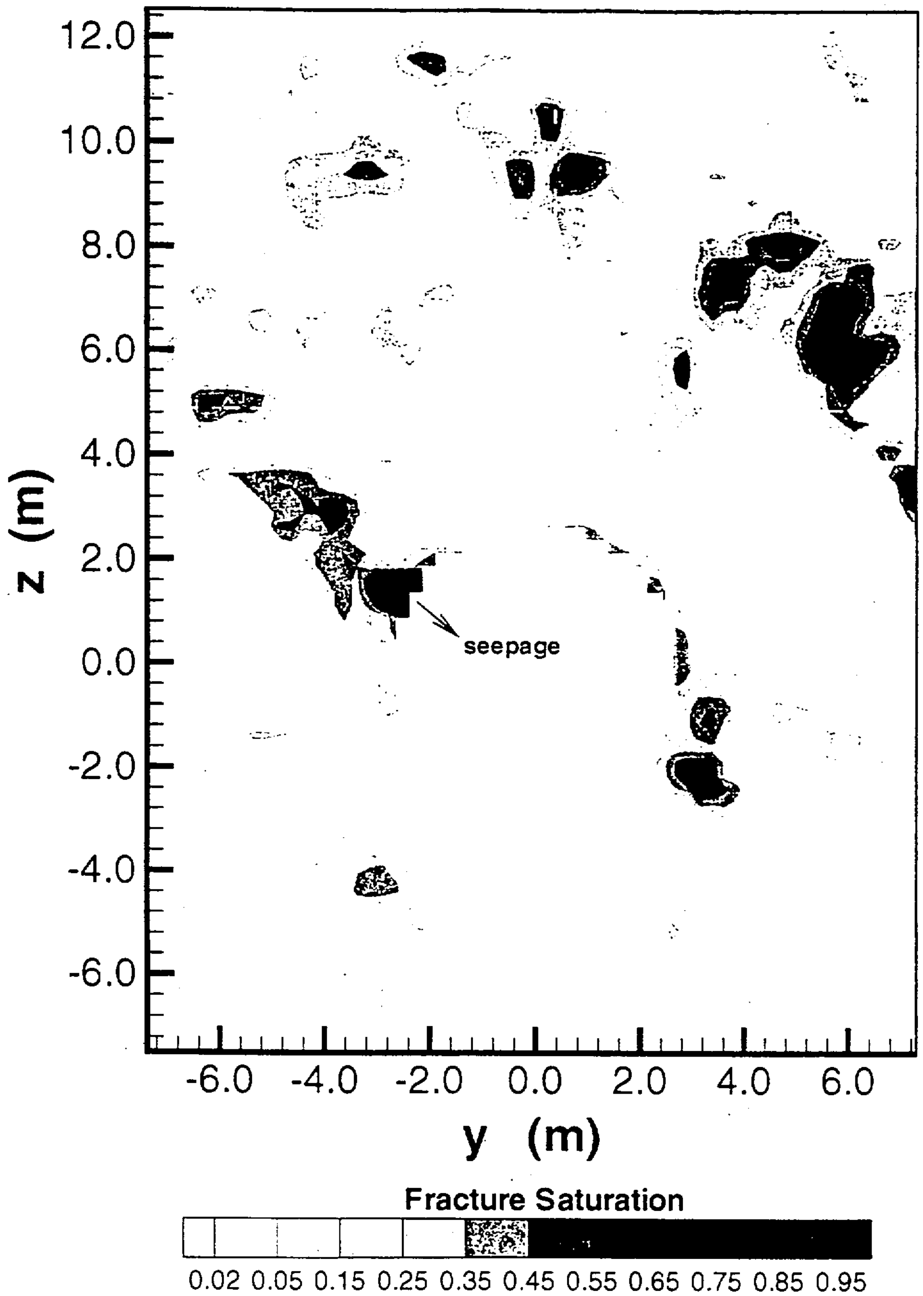

Figure 2-61c. Saturation contours in fracture continuum on slice 1 of the 3-D block for Q_p = 50 mm/yr and IF = 100% at $t = t_D$ = 534 days.

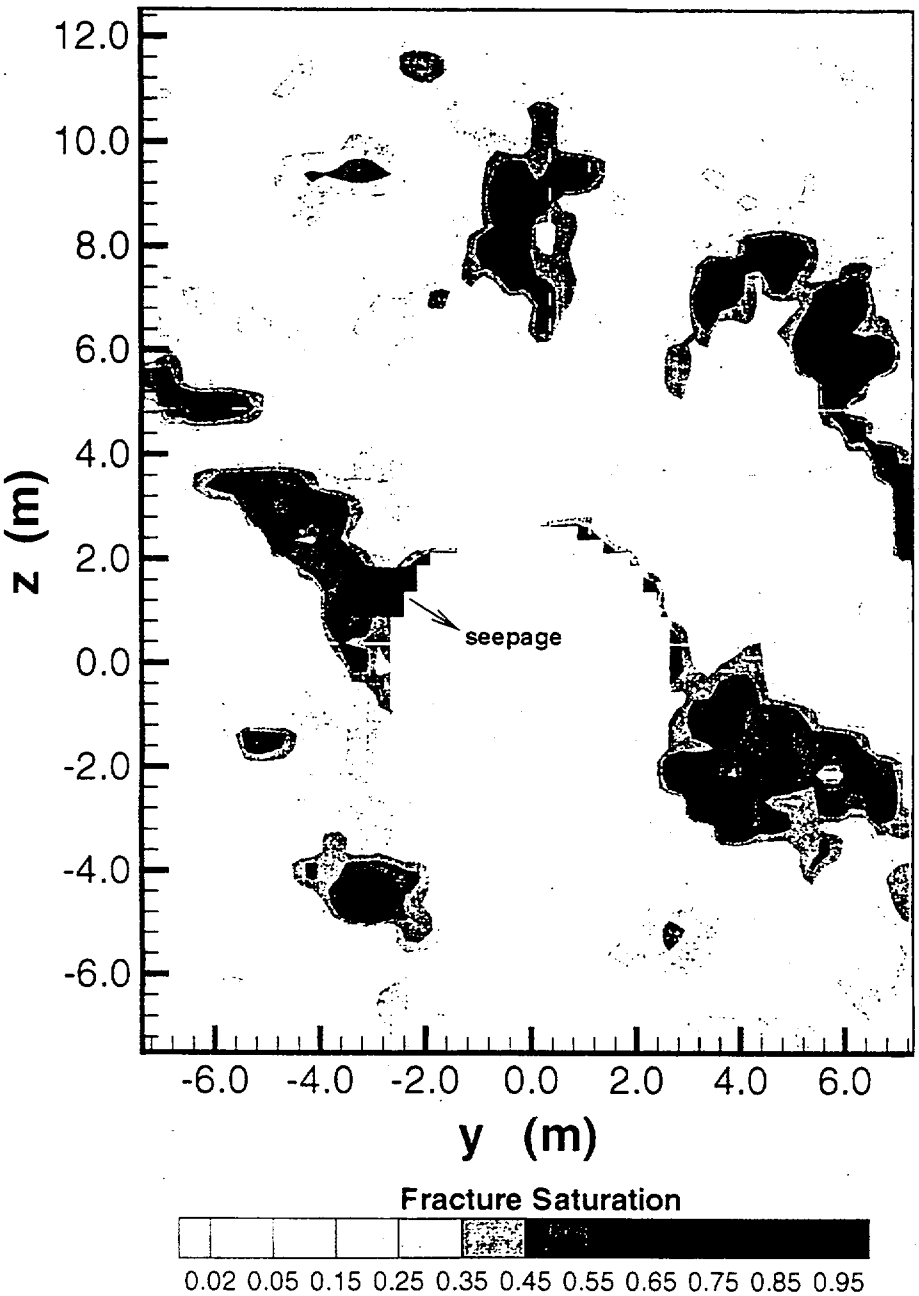

Figure 2-61d. Saturation contours in fracture continuum on slice 1 of the 3-D block for Q_p = 50 mm/yr and IF = 100% at t = 1217 days.

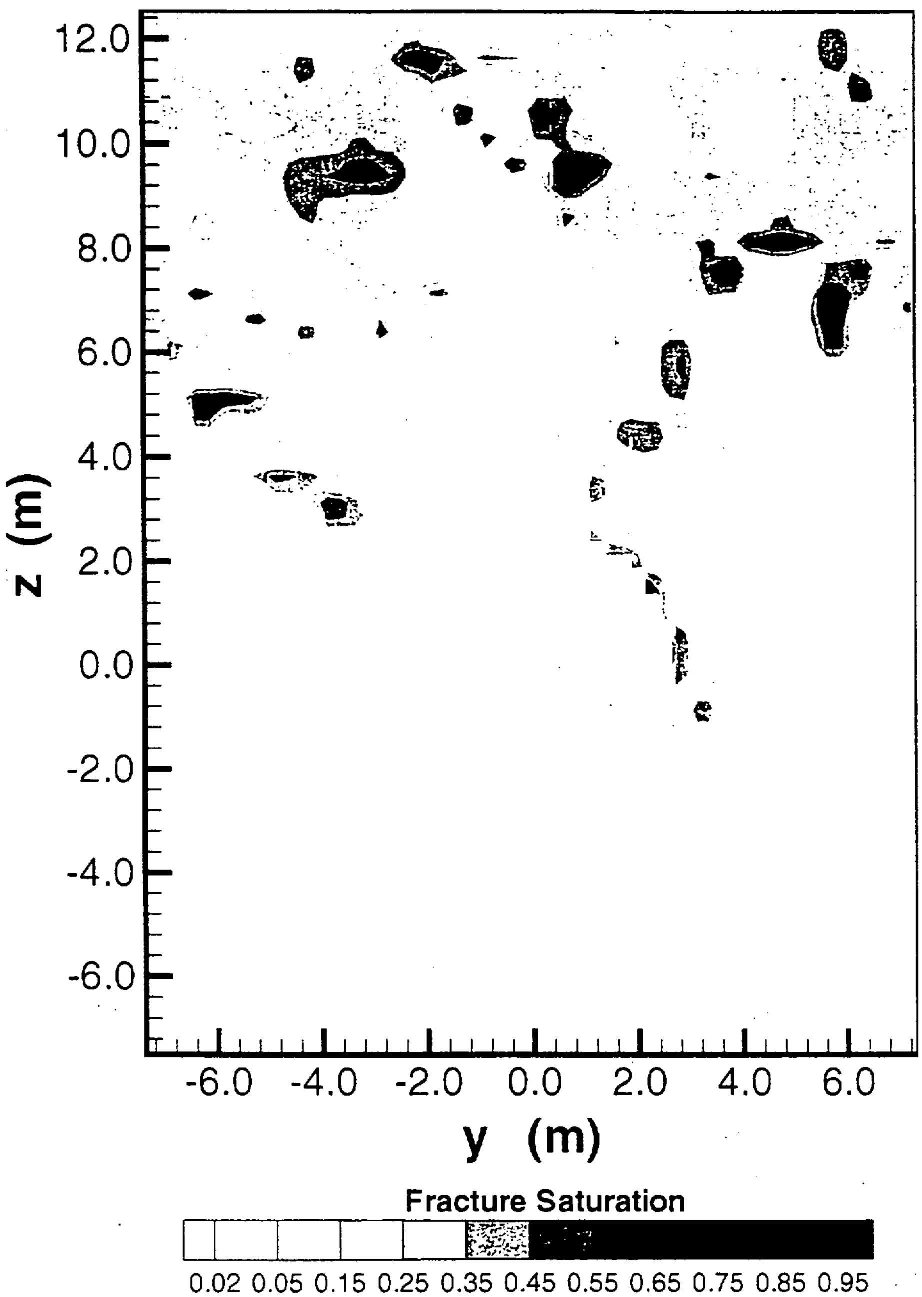

Figure 2-62a. Saturation contours in fracture continuum on slice 1 of the 3-D block for Q_p = 200 mm/yr and IF = 100% at t = 1 day.

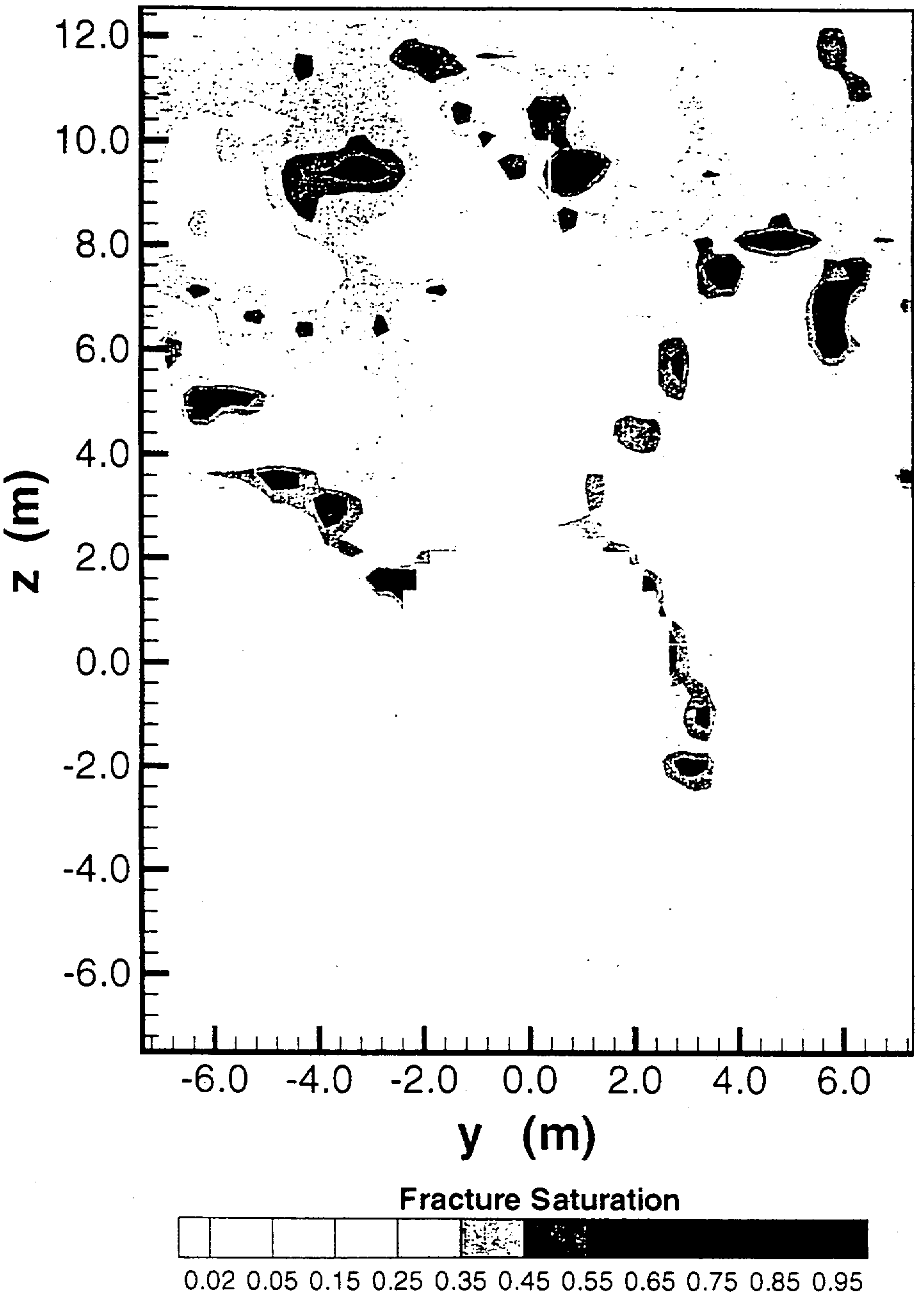

Figure 2-62b. Saturation contours in fracture continuum on slice 1 of the 3-D block for Q_p = 200 mm/yr and IF = 100% at t = 5 days.

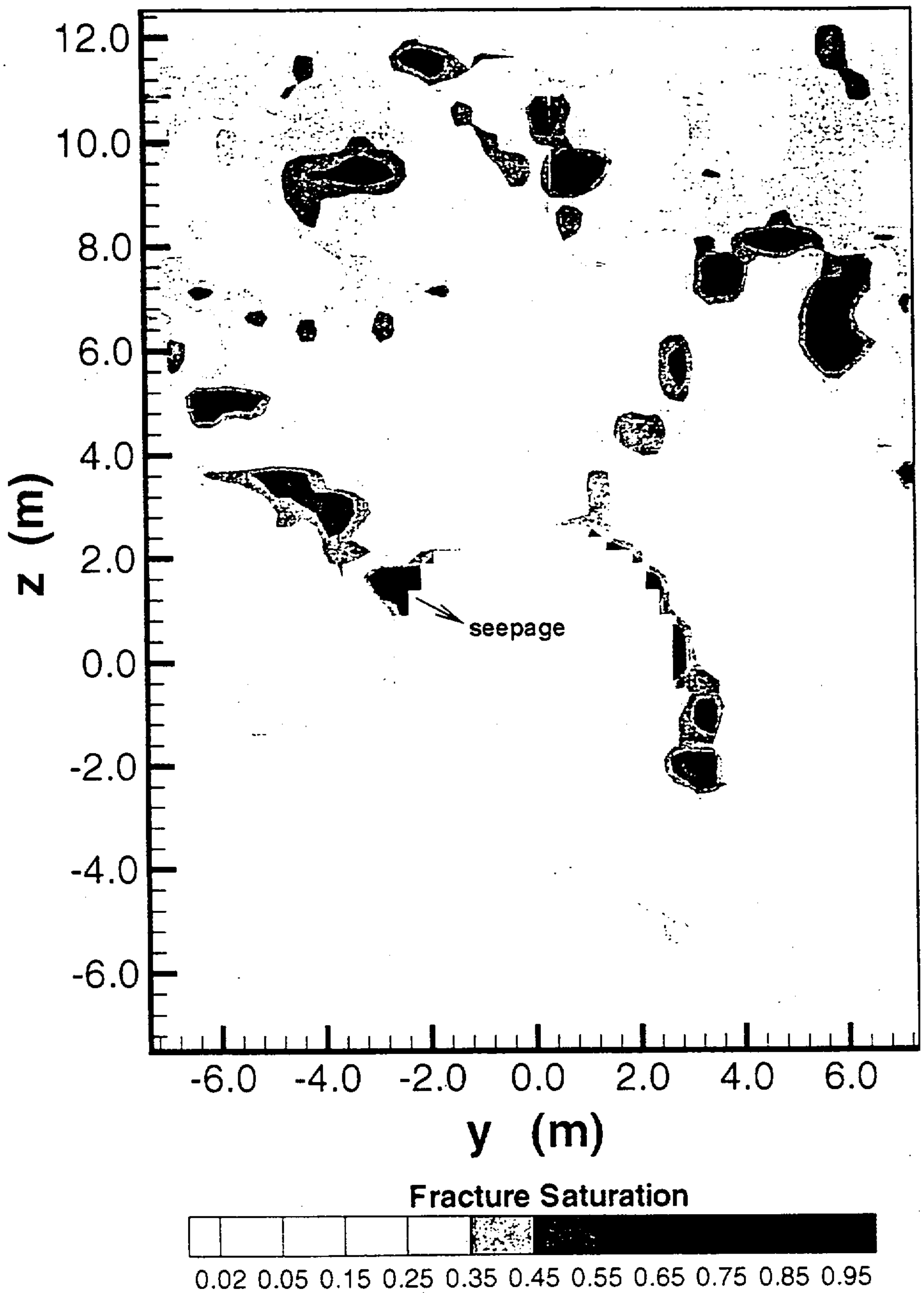

Figure 2-62c. Saturation contours in fracture continuum on slice 1 of the 3-D block for Q_p = 200 mm/yr and IF = 100% at $t = t_D$ = 21 days.

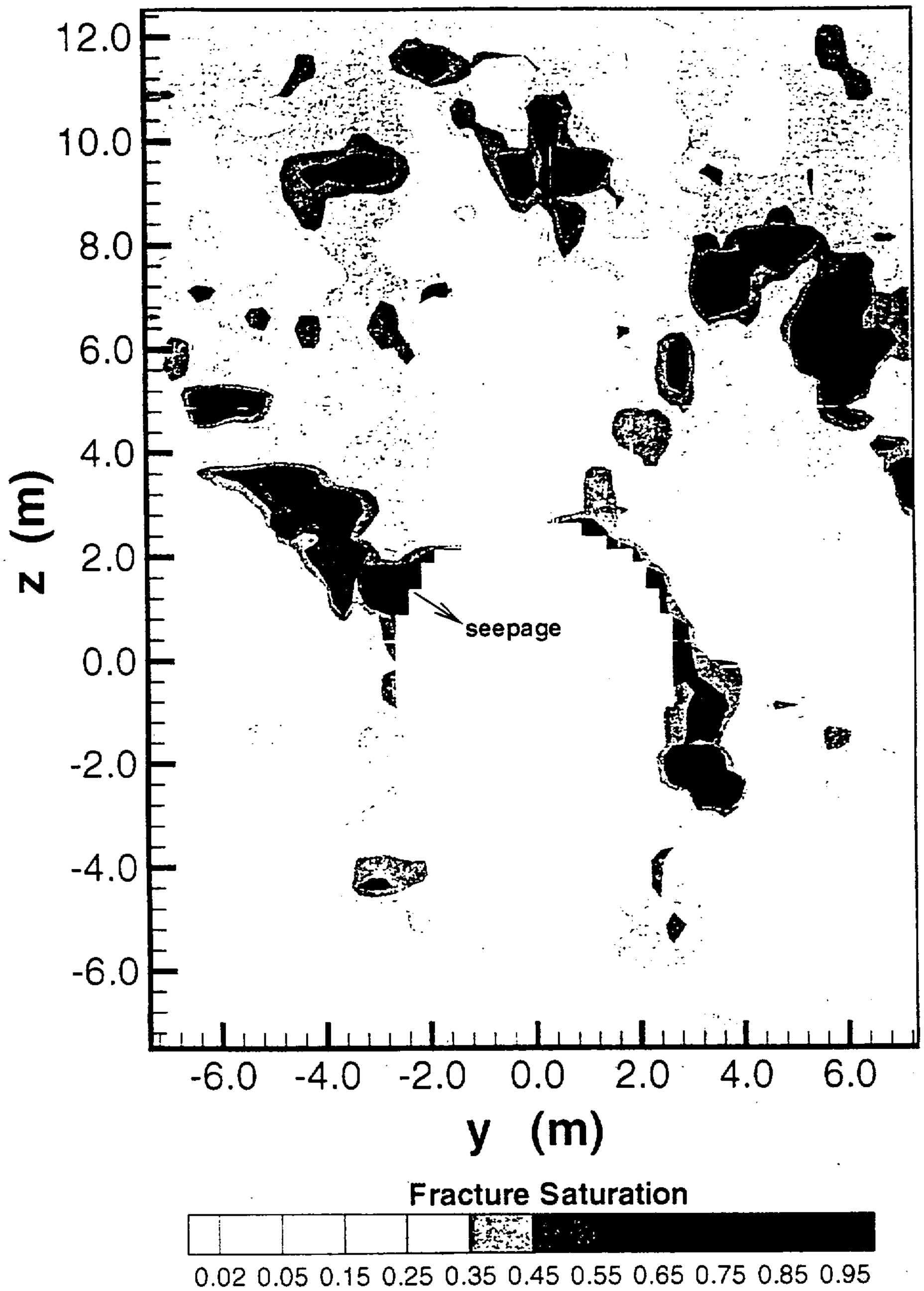

Figure 2-62d. Saturation contours in fracture continuum on slice 1 of the 3-D block for Q_p = 200 mm/yr and IF = 100% at t = 76 days.

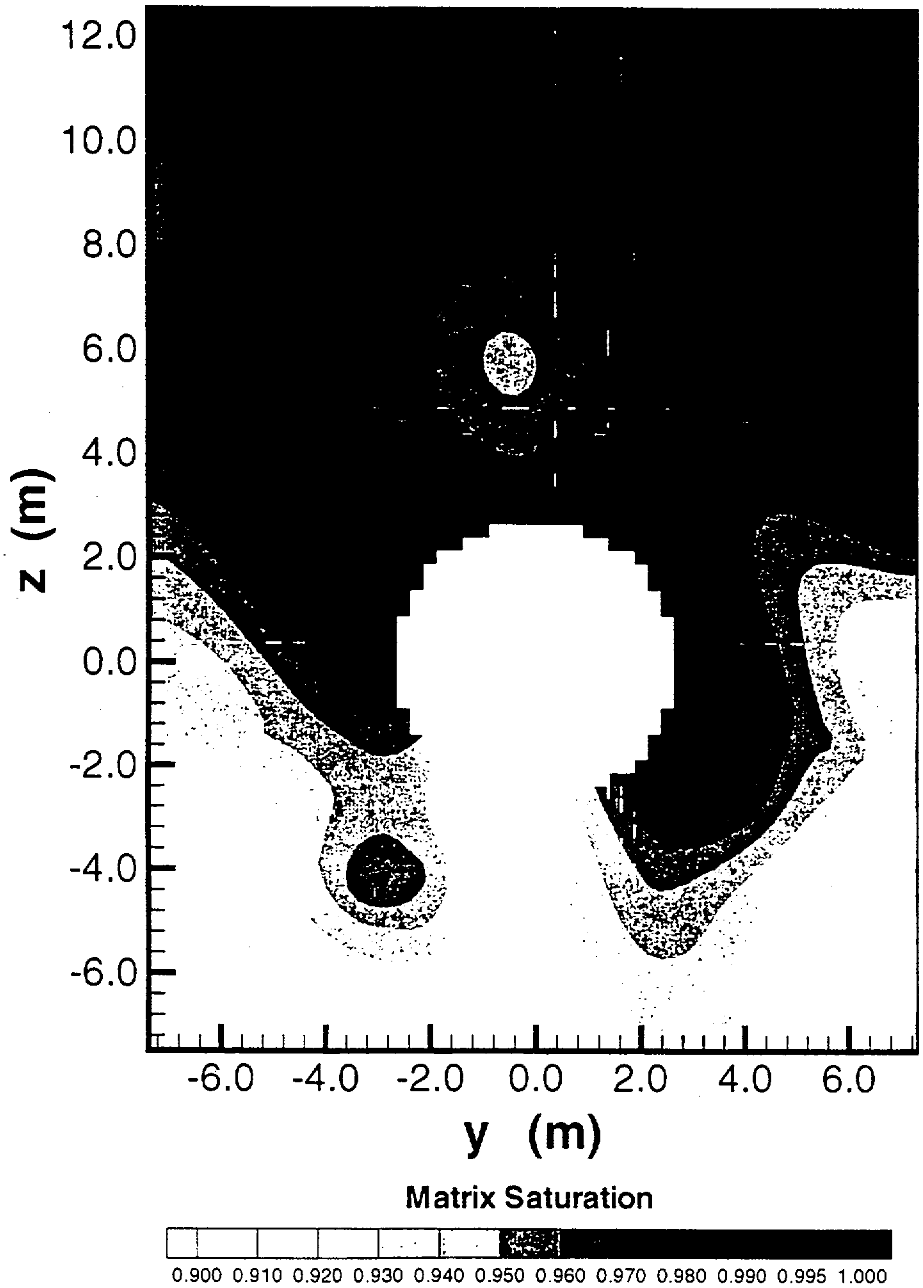

Figure 2-63a. Saturation contours in matrix continuum on slice 1 of the 3-D block for Q_p = 50 mm/yr and IF = 100% at t = t_D = 534 days.

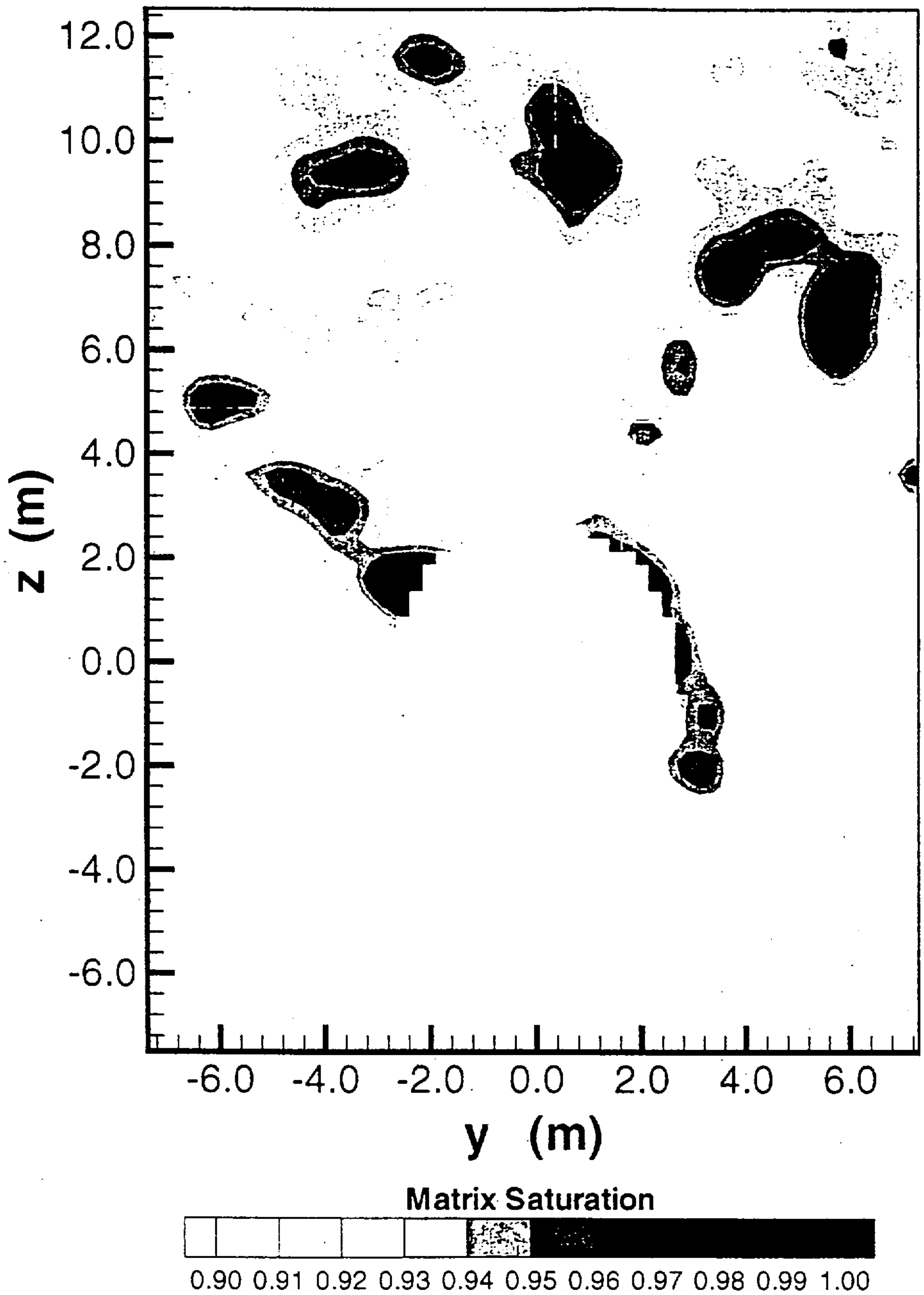

Figure 2-63b. Saturation contours in matrix continuum on slice 1 of the 3-D block for Q_p = 200 mm/yr and IF = 100% at t = t_D = 21 days.

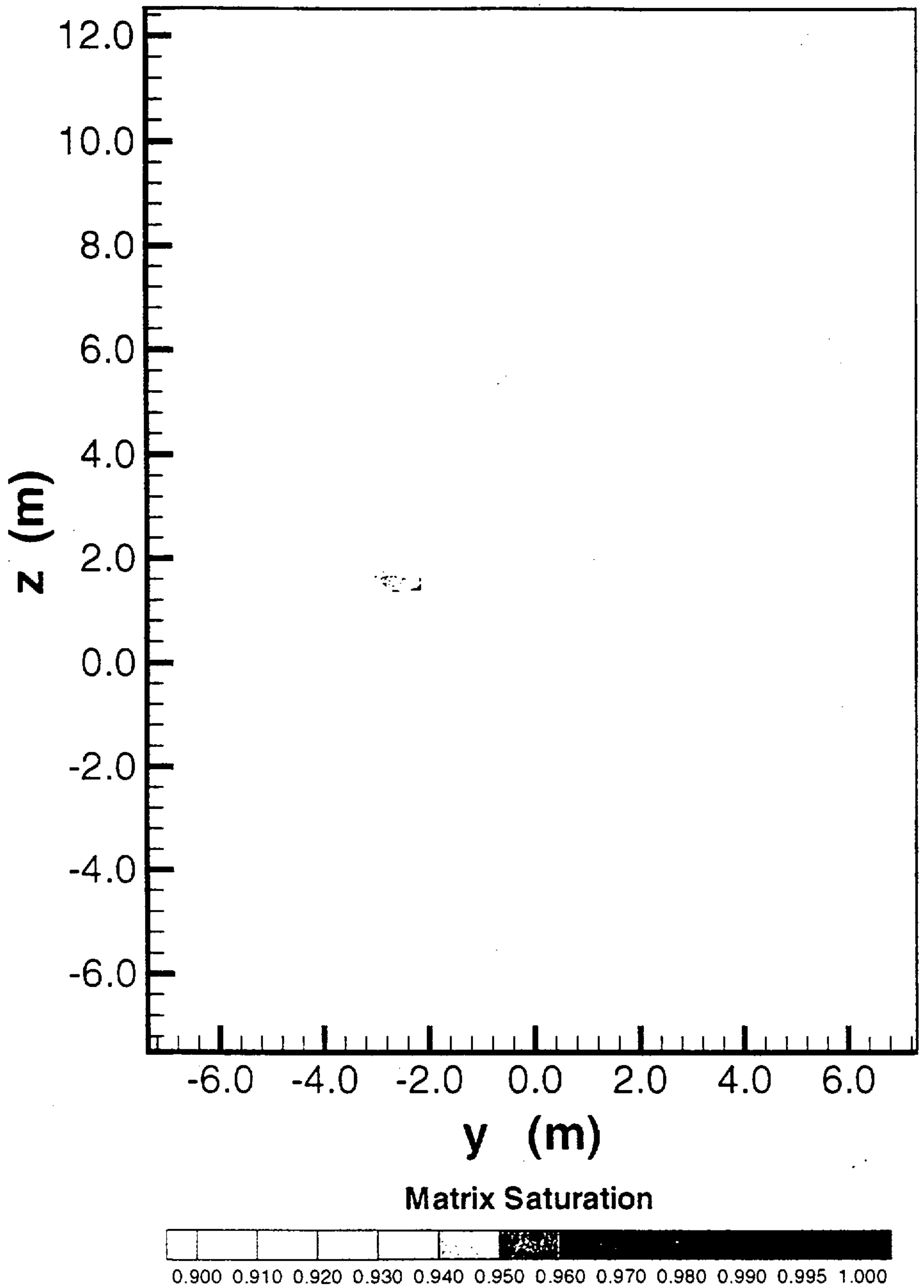

Figure 2-64a. Saturation contours in matrix continuum on slice 1 of the 3-D block for Q_p = 50 mm/yr and IF = 10% at t = t_D = 8.4 days.

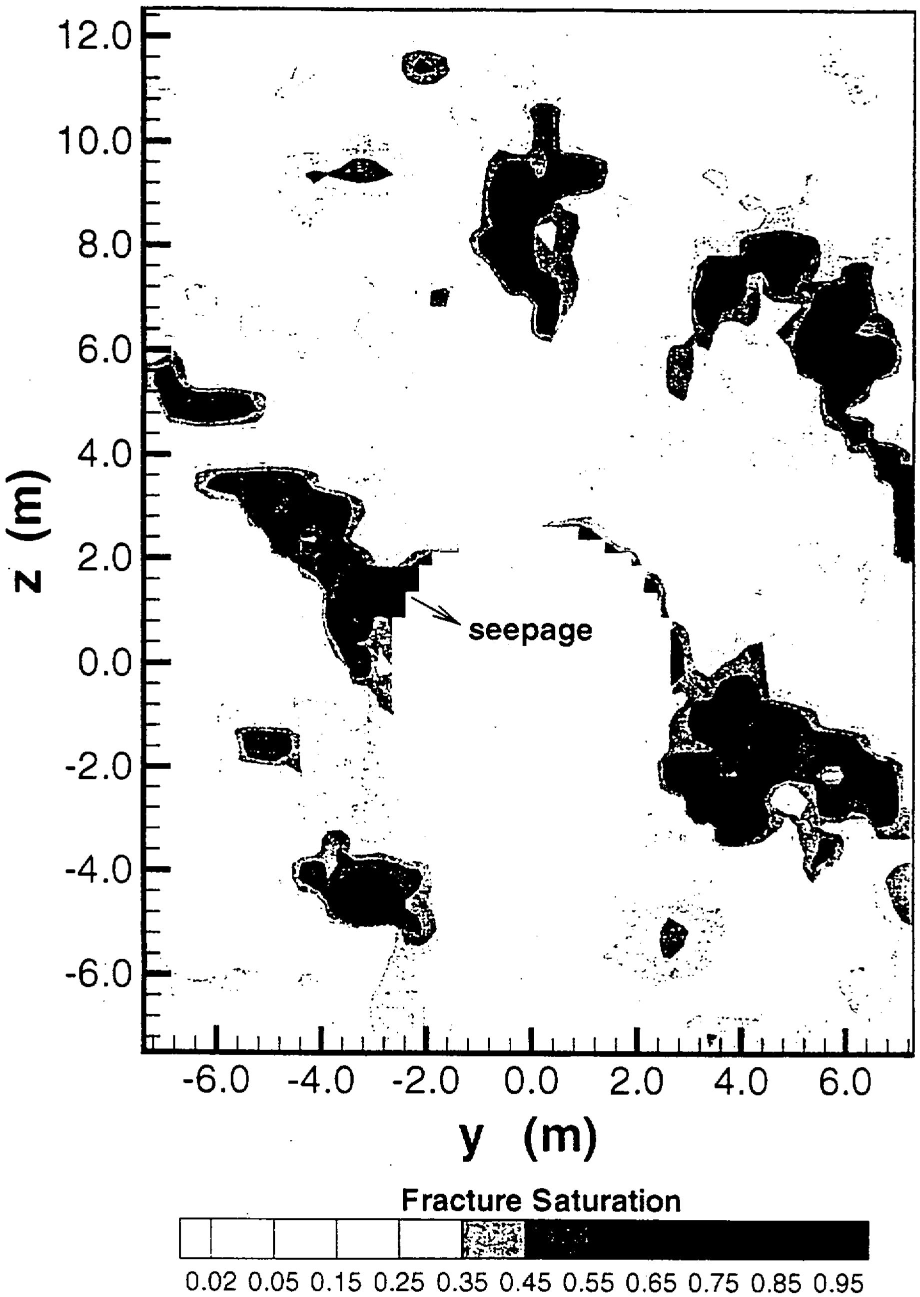

Figure 2-64b. Saturation contours in fracture continuum on slice 1 of the 3-D block for Q_p = 50 mm/yr and IF = 10% at t = t_D = 8.4 days.

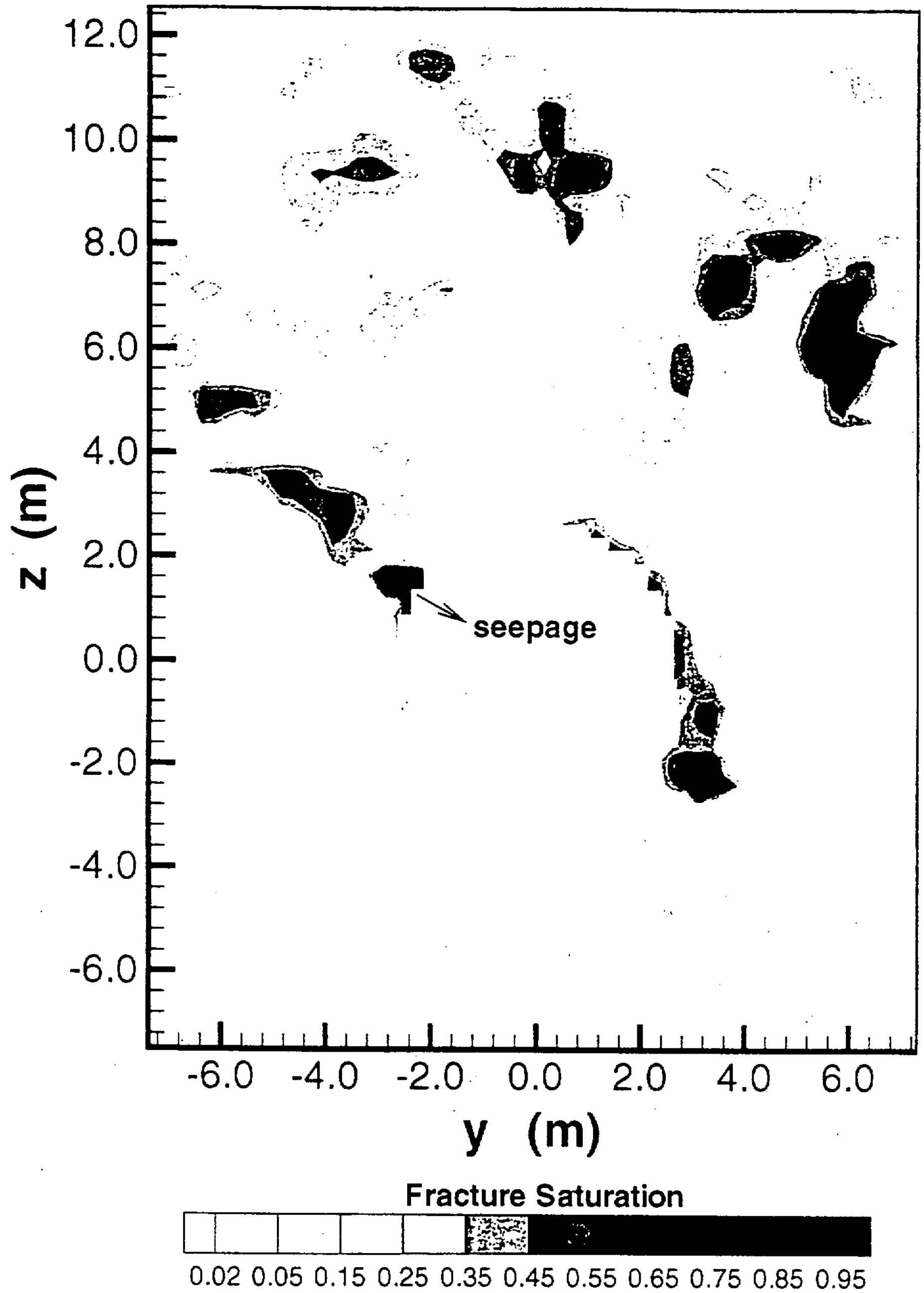

Figure 2-64c. Saturation contours in fracture continuum on slice 1 of the 3-D block for Q_p = 50 mm/yr and IF = 0% at $t = t_D = 2.1$ days.

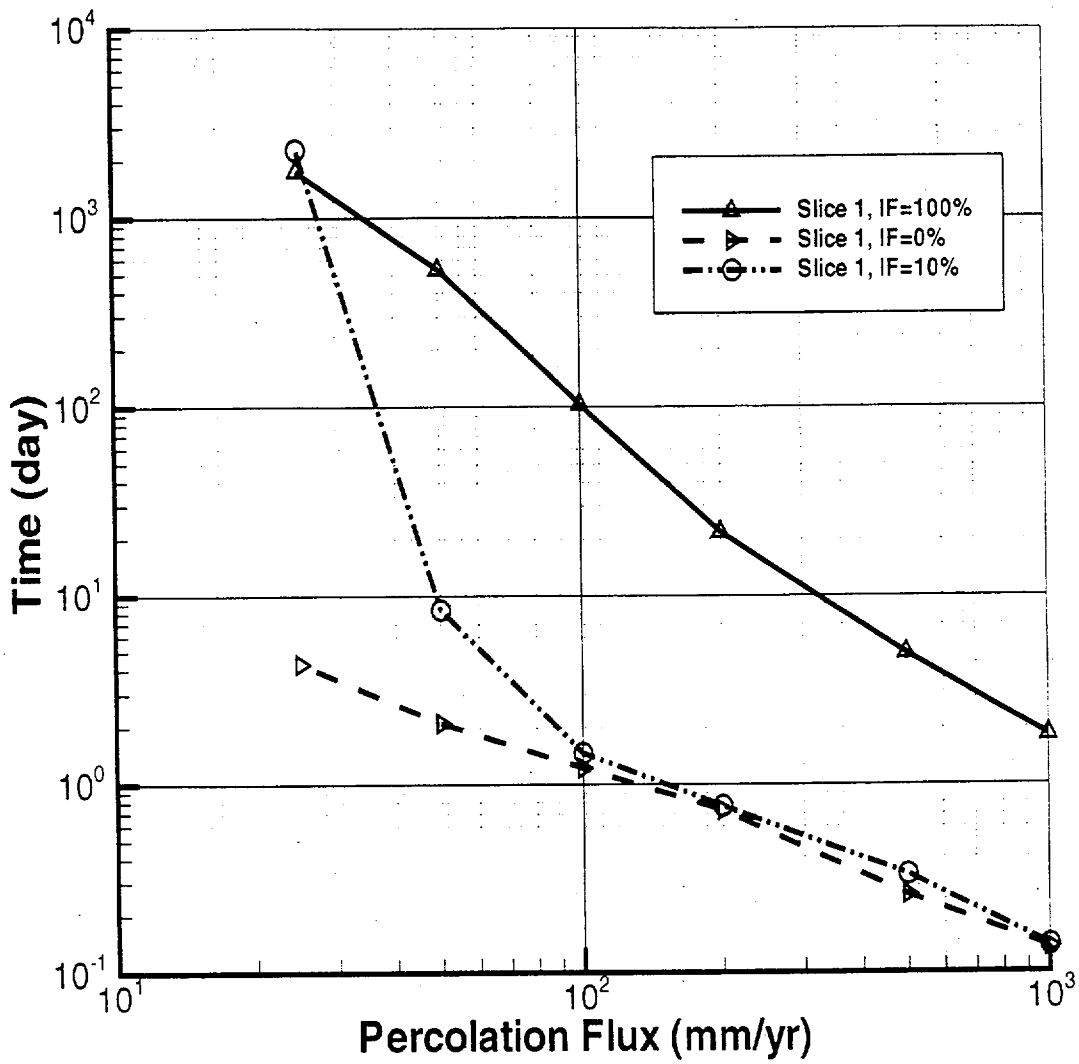

Figure 2-65. Time of seepage into drift as a function of Q_p for slice 1 of the 3-D block and different interface factors IF (IF = 100%, IF = 10% and IF = 0%).

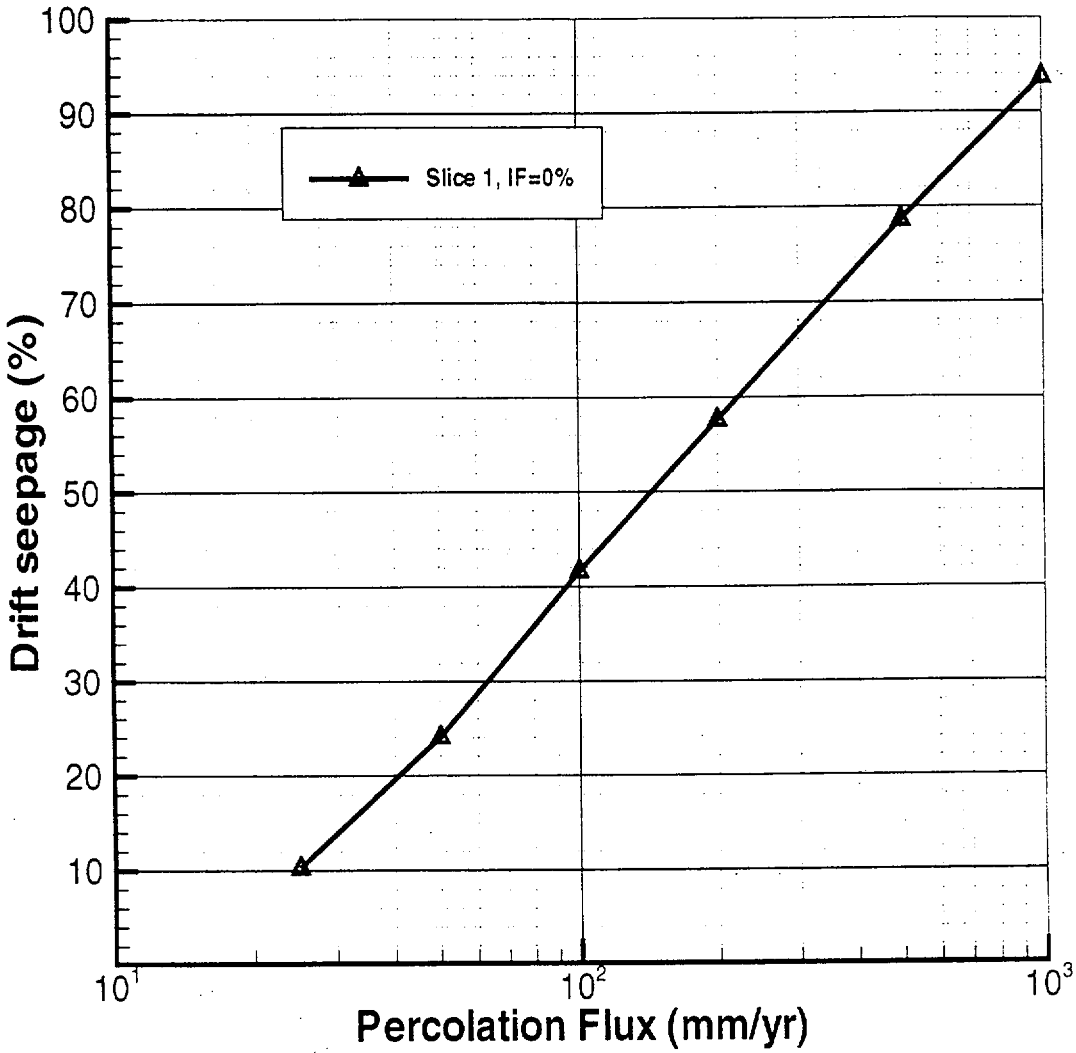

Figure 2-66. Rate of seepage into drift as a function of Q_p for slice 1 of the 3-D block and IF = 0%.

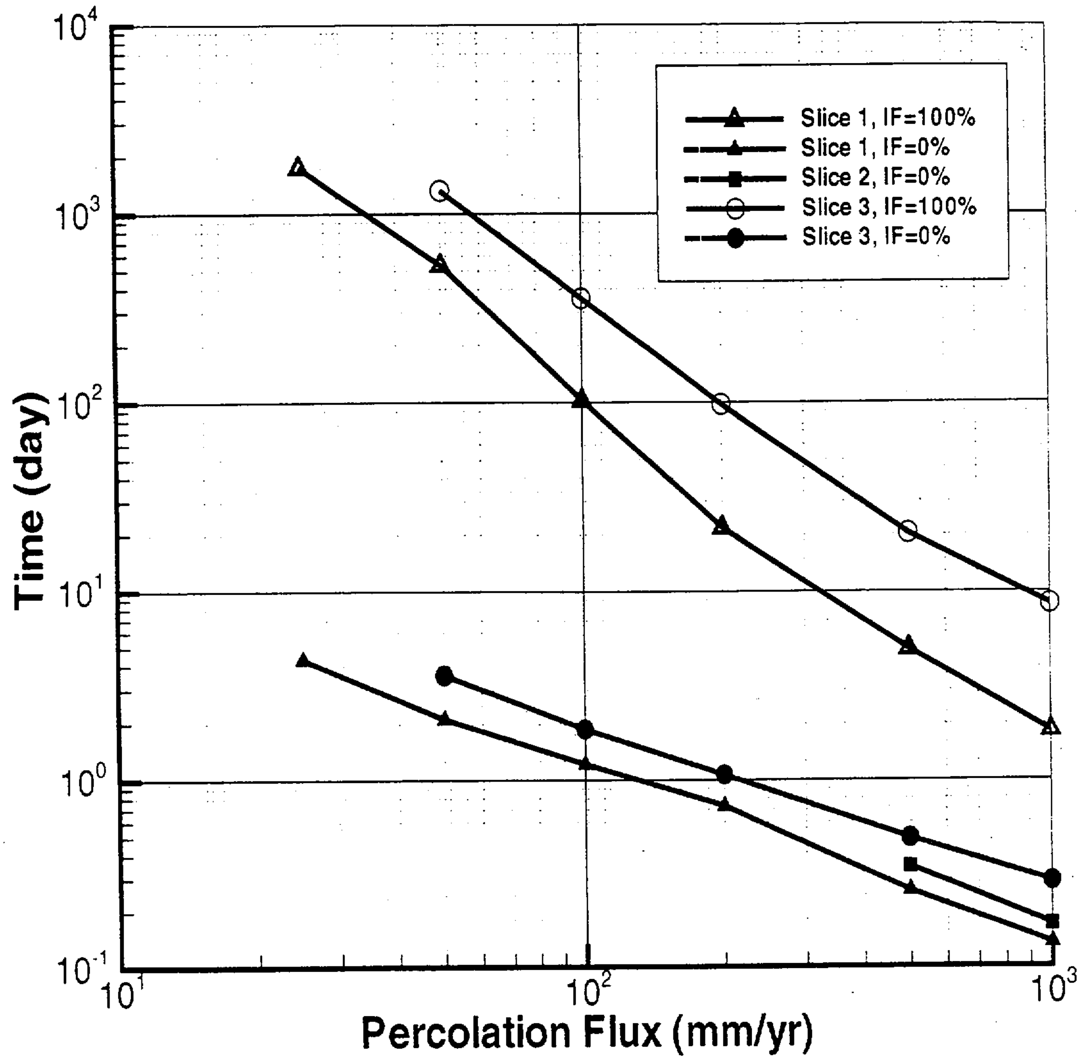

Figure 2-67. Time of seepage into drift as a function of Q_p for slices 1, 2, and 3 of the 3-D block. Fo slice 2, simulations have only been performed for the IF = 0% case.

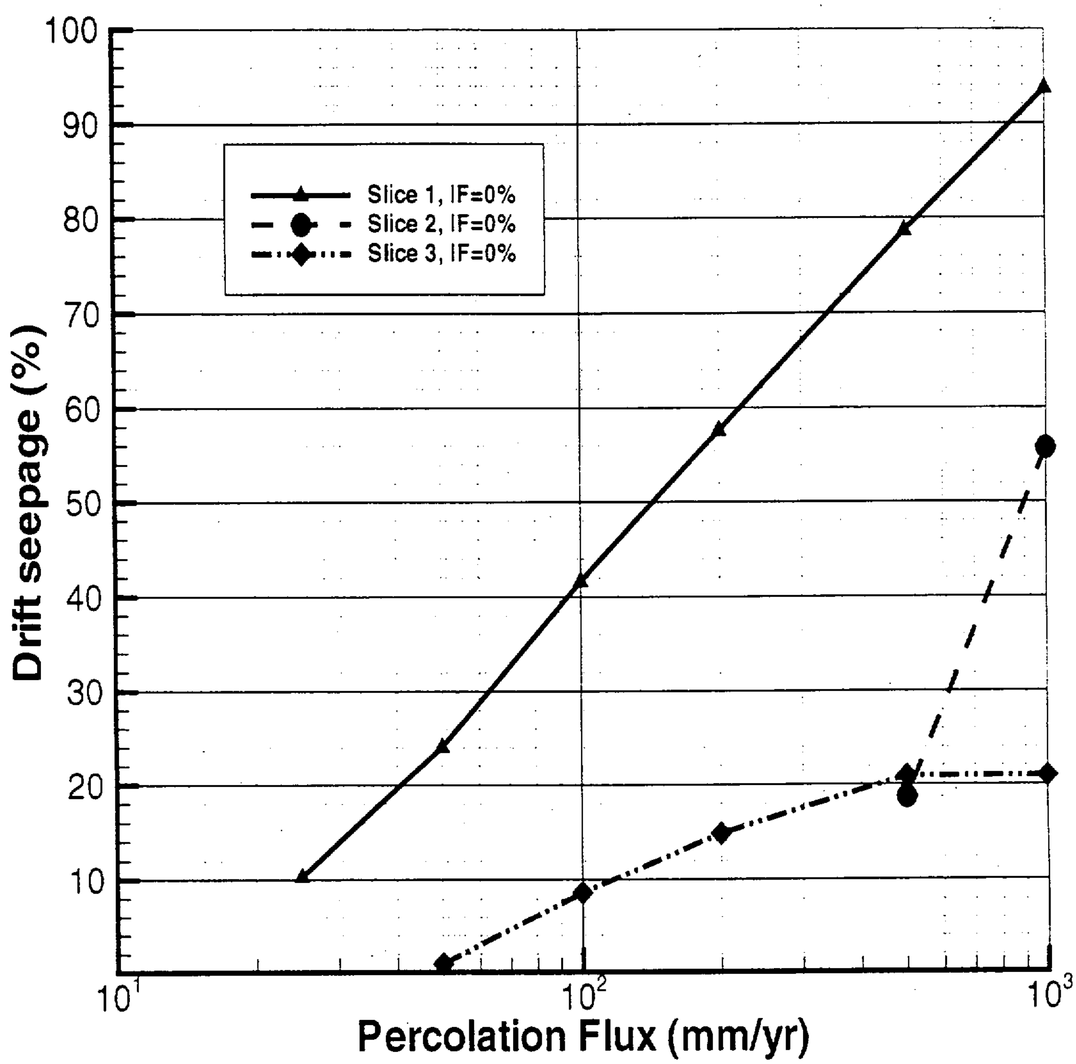

Figure 2-68. Rate of seepage into drift as a function of Q_p for slices 1, 2, and 3 of the 3-D block.

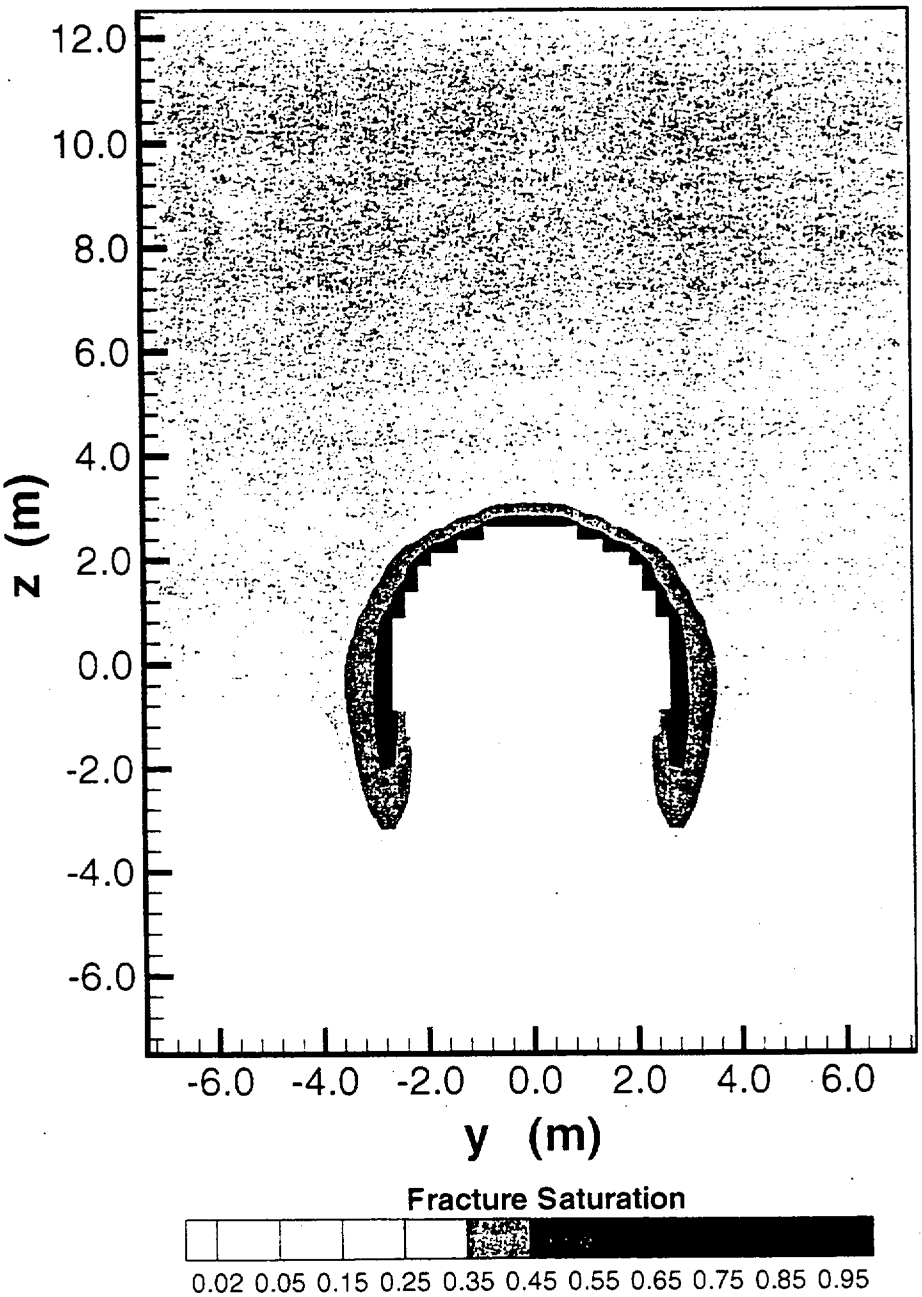

Figure 2-69a. Homogeneous case: saturation contours in fracture continuum for Q_p = 200 mm/yr and IF = 0% at t = 1 day.

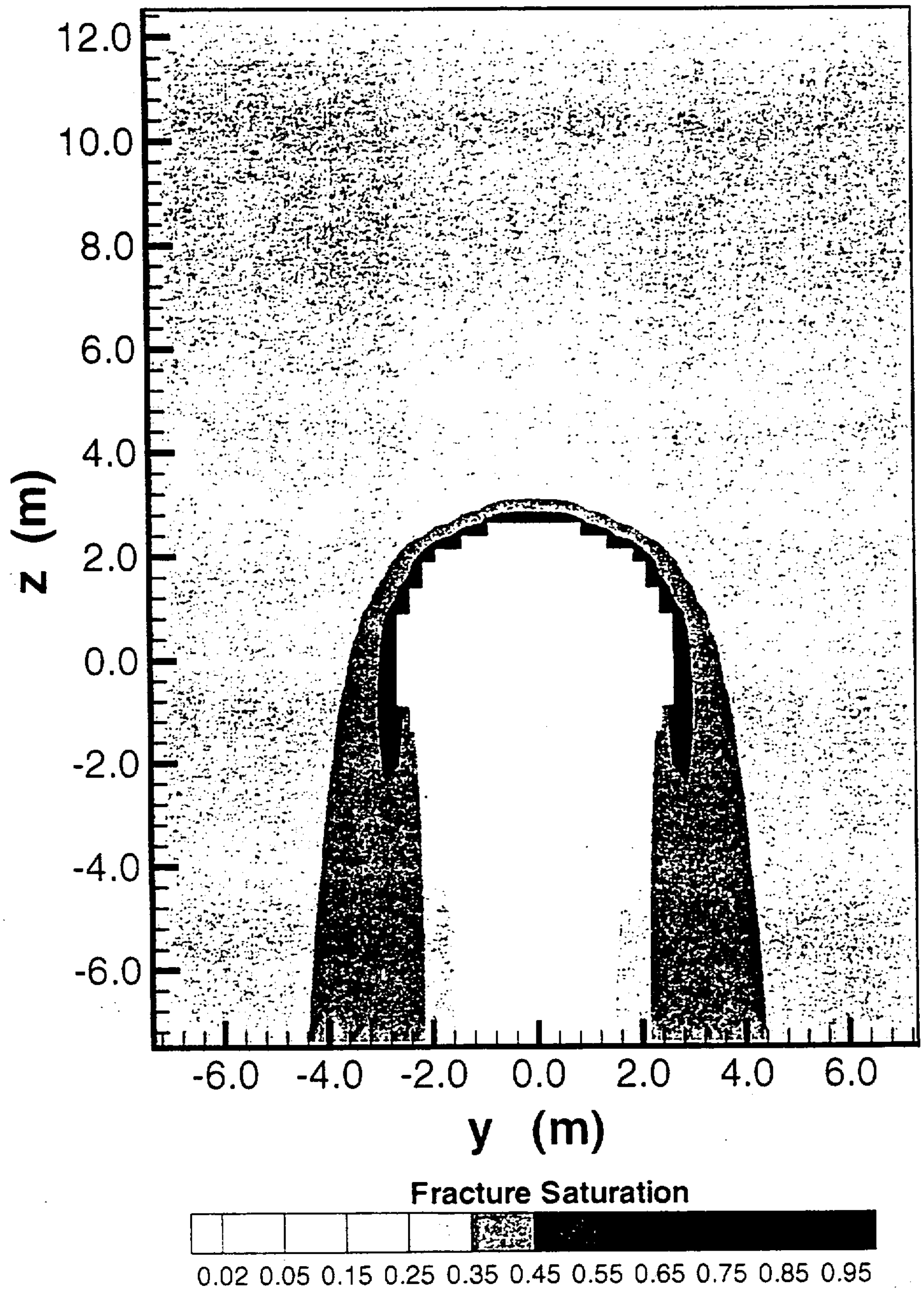

Figure 2-69b. Homogeneous case: saturation contours in fracture continuum for Q_p = 200 mm/yr and IF = 0% at t = 2 days.

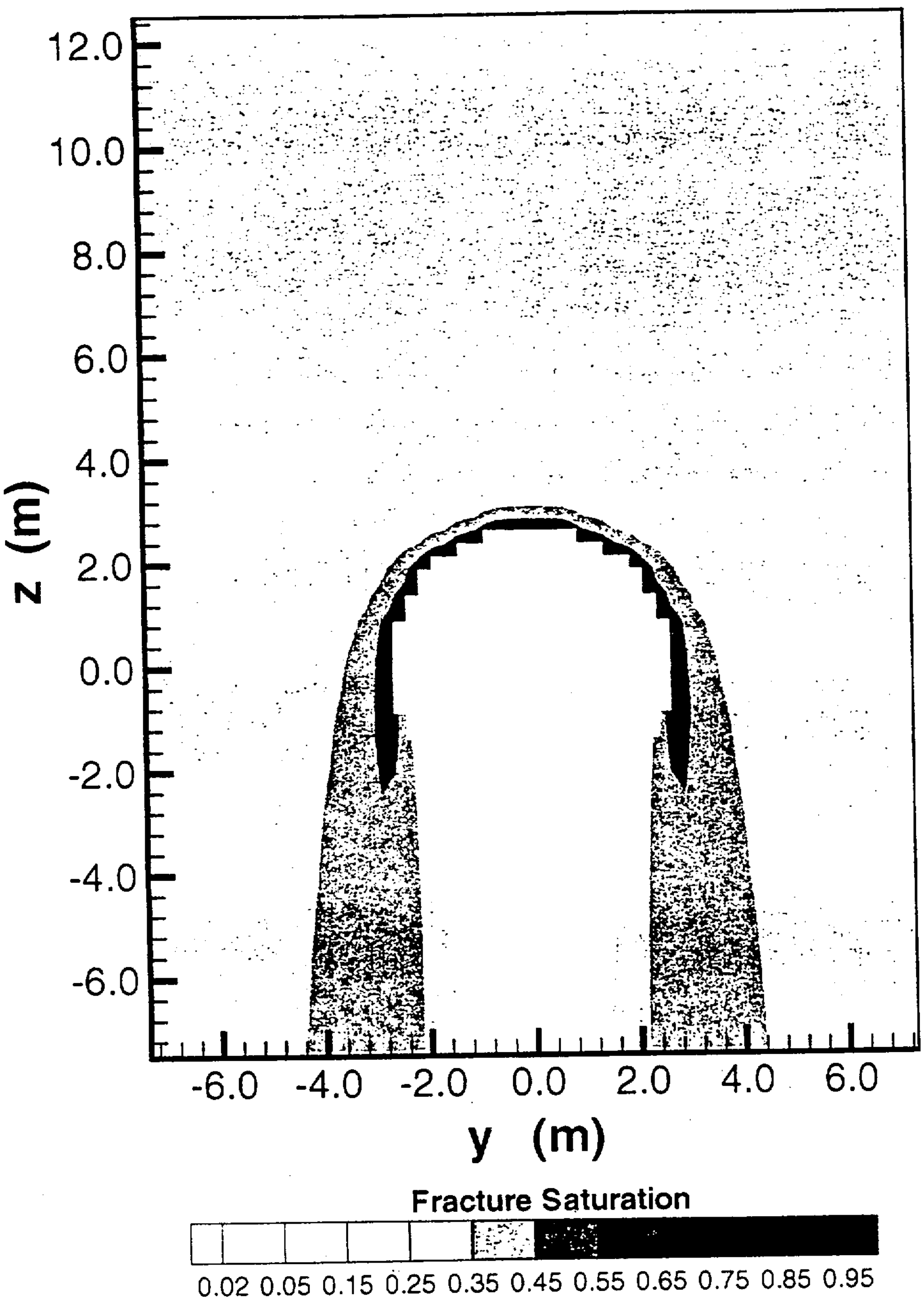

Figure 2-69c. Homogeneous case: saturation contours in fracture continuum for Q_p = 200 mm/yr and IF = 0% at t = 900 days.

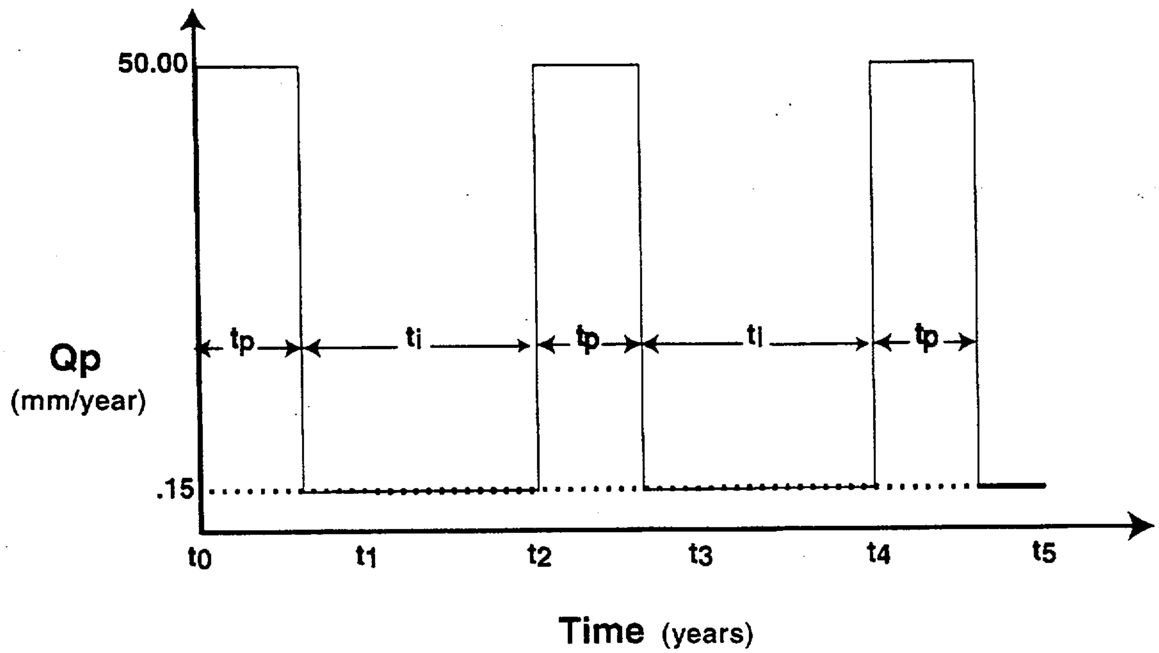

Figure 2-70. Schedule for successive pulses.

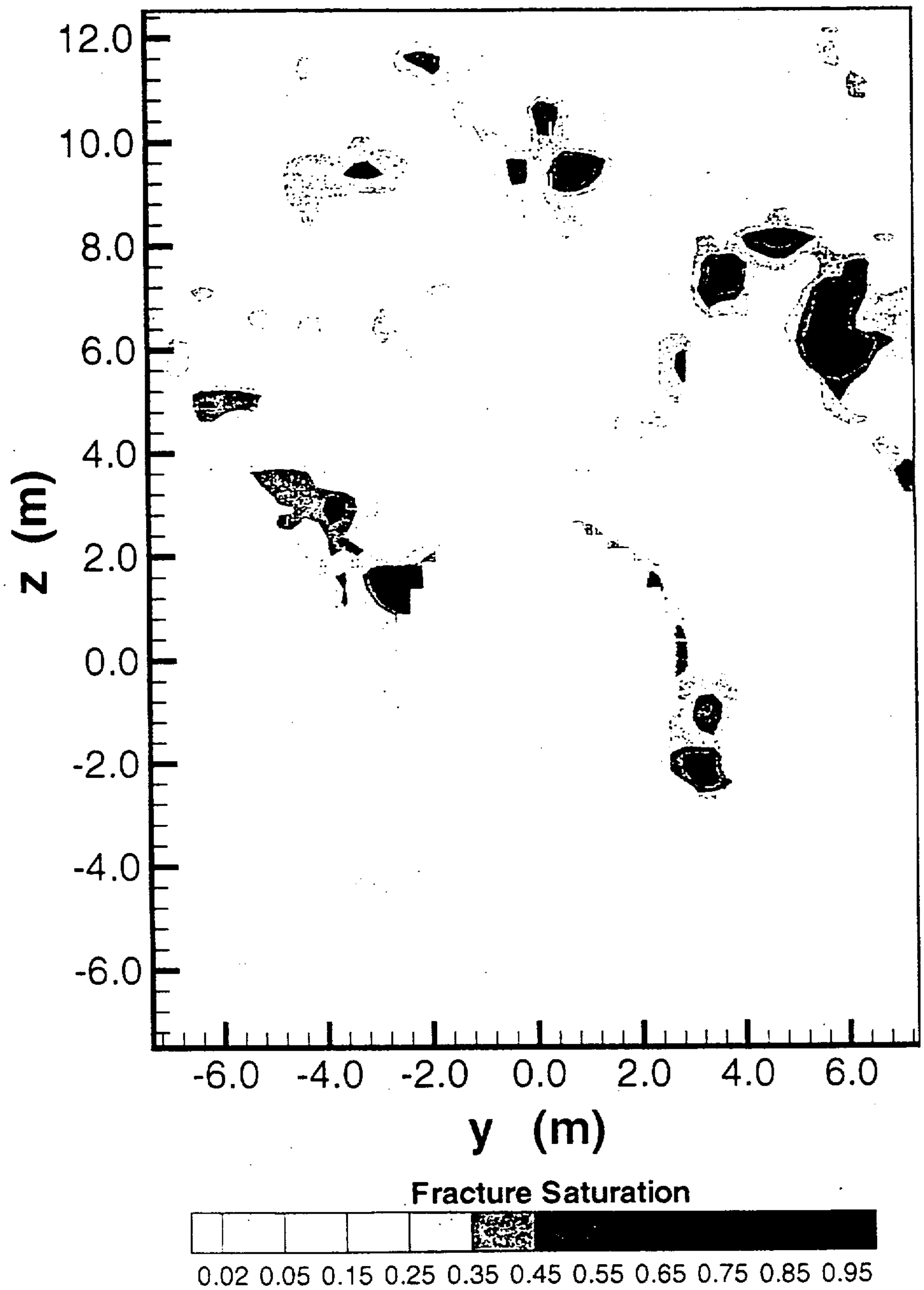

Figure 2-71a. Saturation profiles in fracture continuum on slice 1 of the 3-D block at $t = t_p = 1$ year.

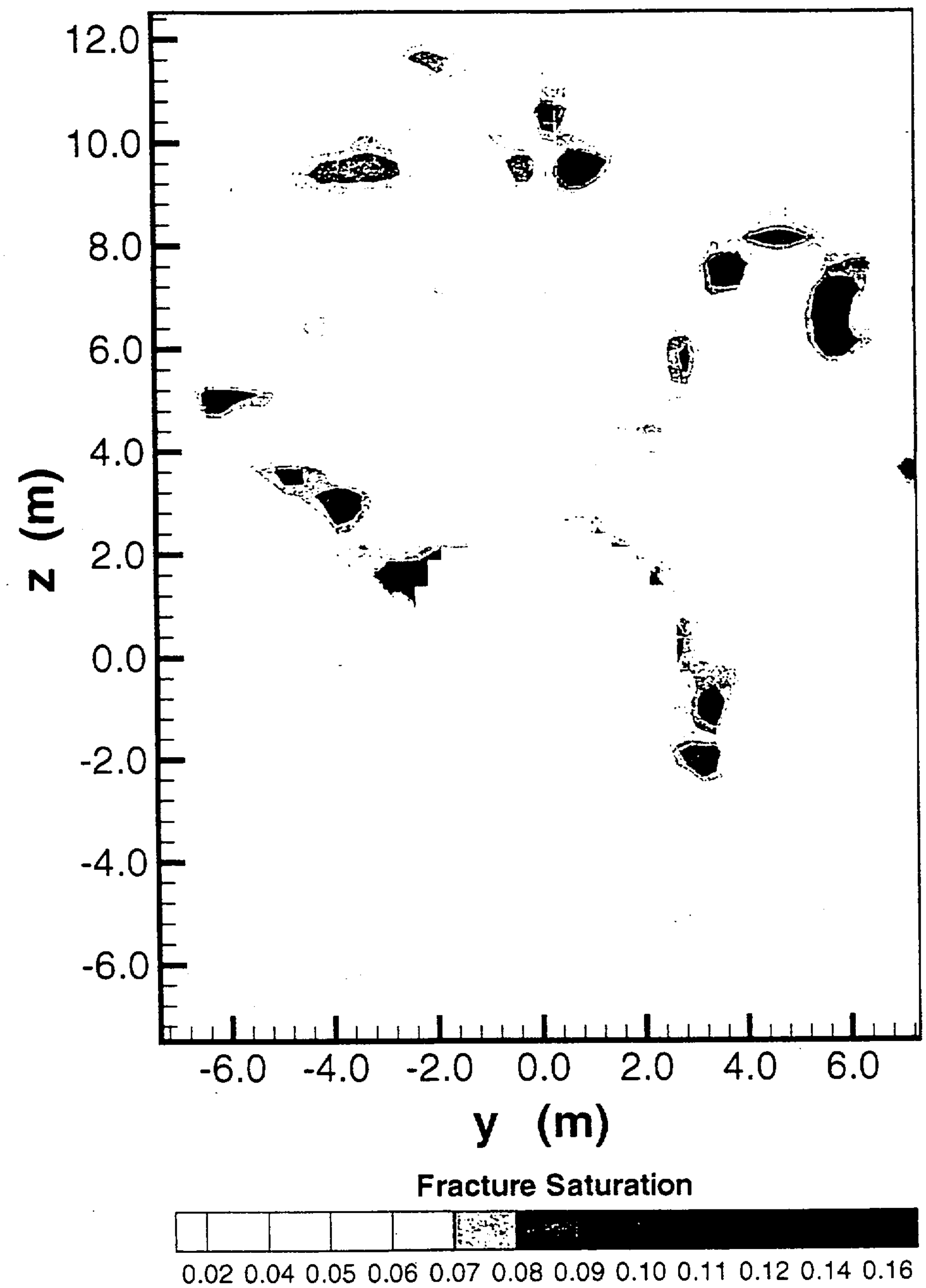

Figure 2-71b. Saturation profiles in fracture continuum on slice 1 of the 3-D block at $t = t_p + 9 = 10$ years.

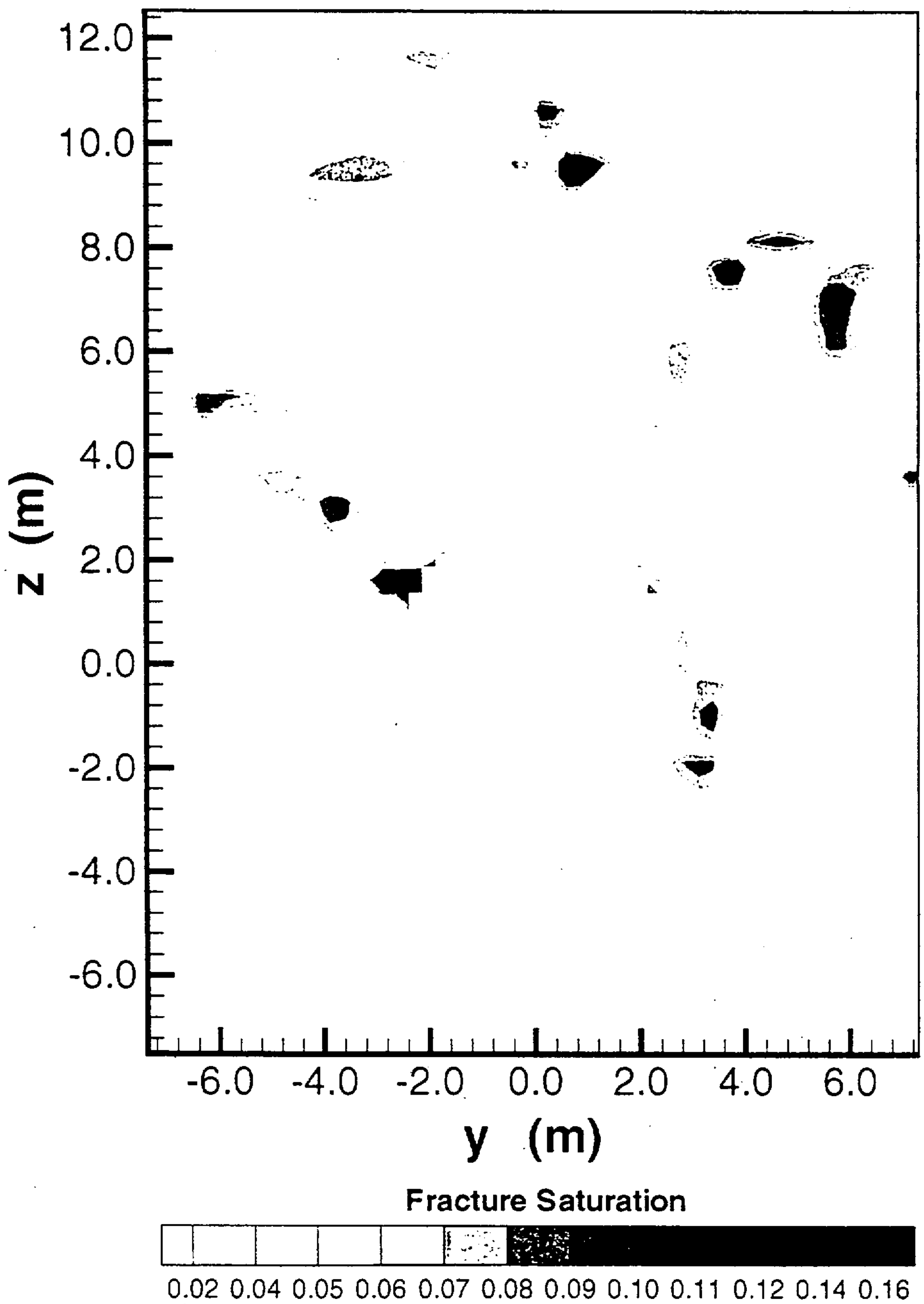

Figure 2-71c. Saturation profiles in fracture continuum on slice 1 of the 3-D block at $t = t_p + 999 = 1{,}000$ years.

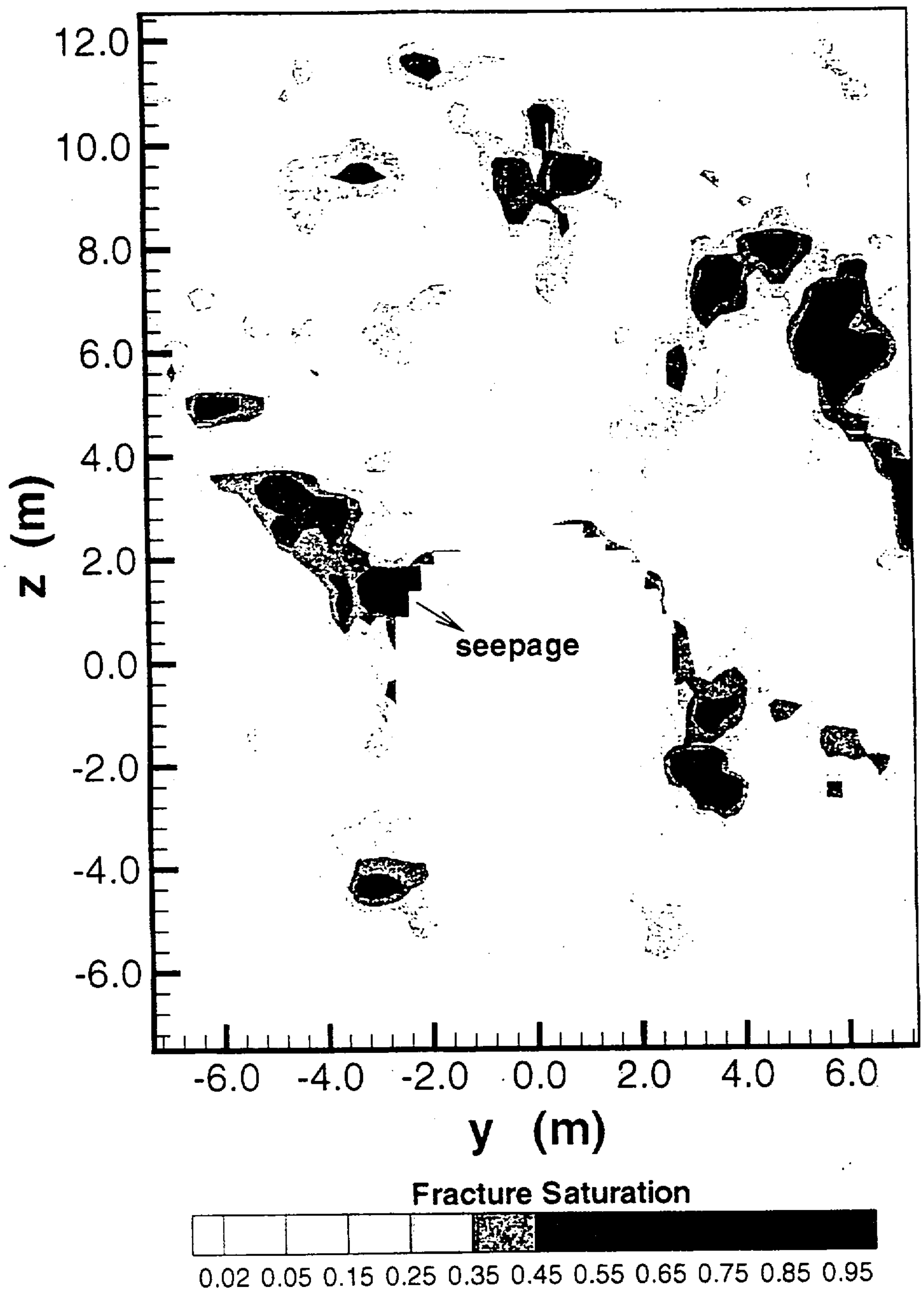

Figure 2-72a. Effect of second pulse: saturation contours in fracture continuum on slice 1 of the 3-D block at the end of second pulse $t = 2\ t_p + t_i = 11$ years.

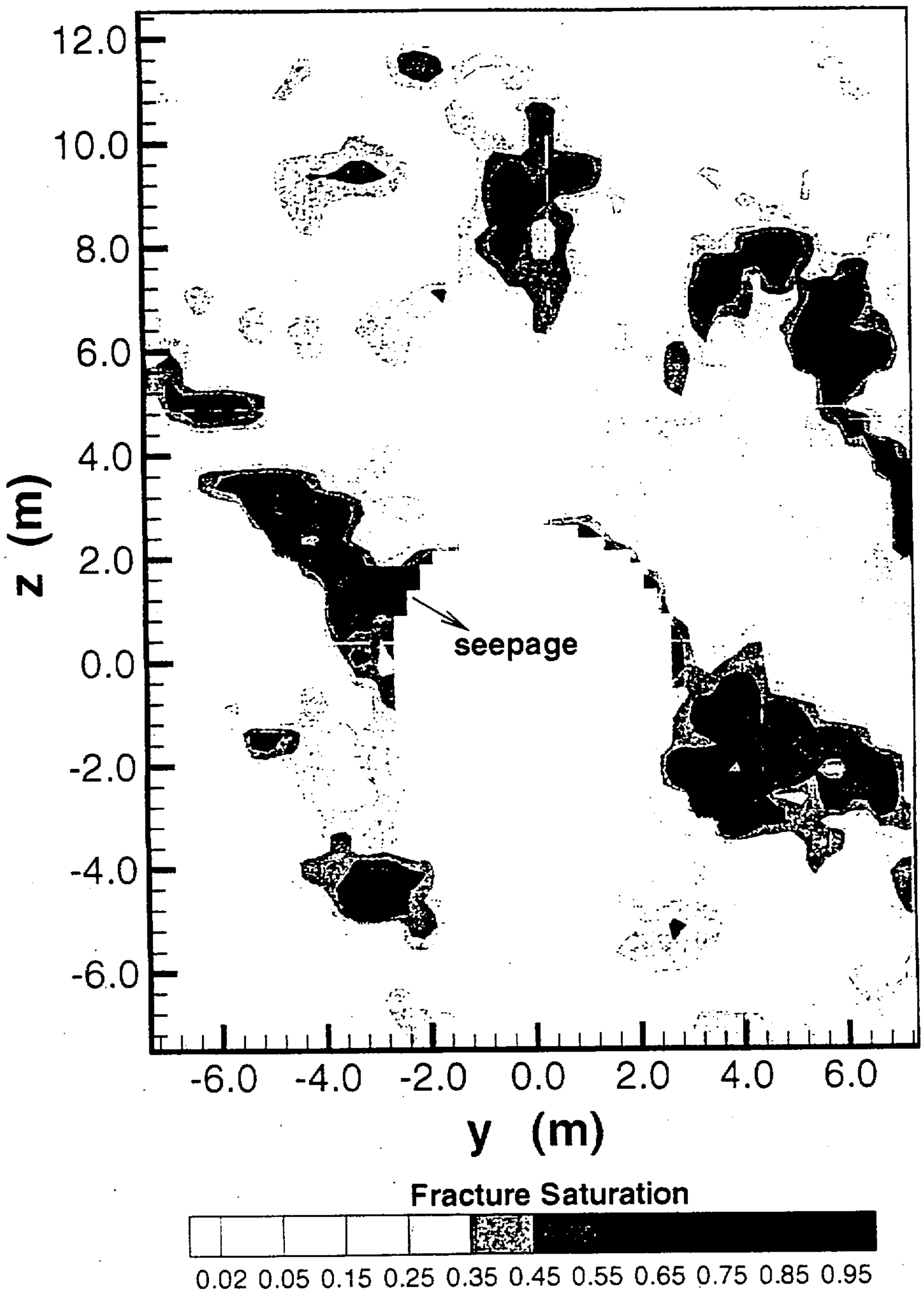

Figure 2-72b. Effect of third pulse: saturation contours in fracture continuum on slice 1 of the 3-D block at the end of second pulse $t = 3\ t_p + 2\ t_i = 21$ years.

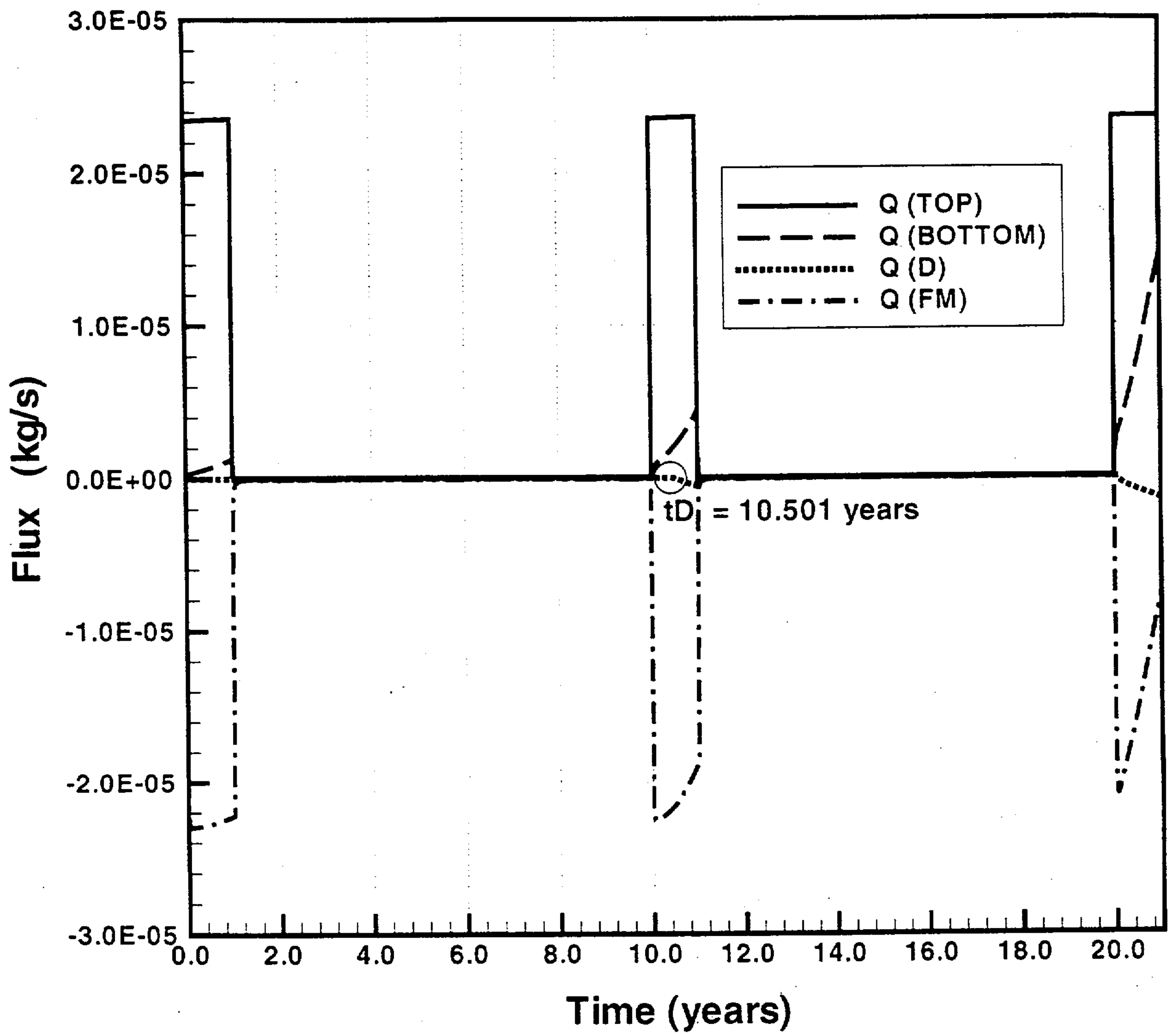

Figure 2-72c. Q_{Top}, Q_{Bottom}, Q_D, and Q_{FM} as a function of time for three successive pulses. Note that $Q_D = 0$ for the first pulse, but Q_D becomes non-zero for the second and third pulses. Simulations are performed for slice 1 of the 3-D block.

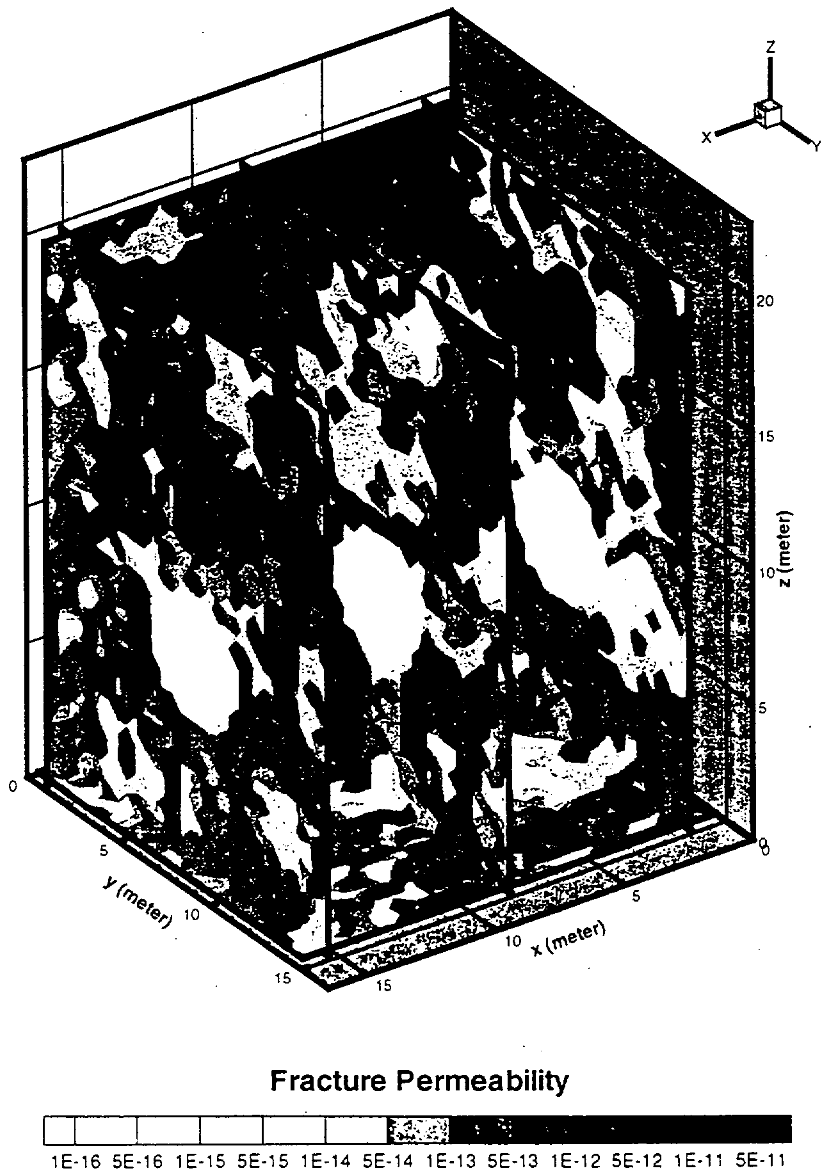

Figure 2-73. Heterogeneous-permeability field for three-vertical planes along y-direction in part 1 of the 3-D block.

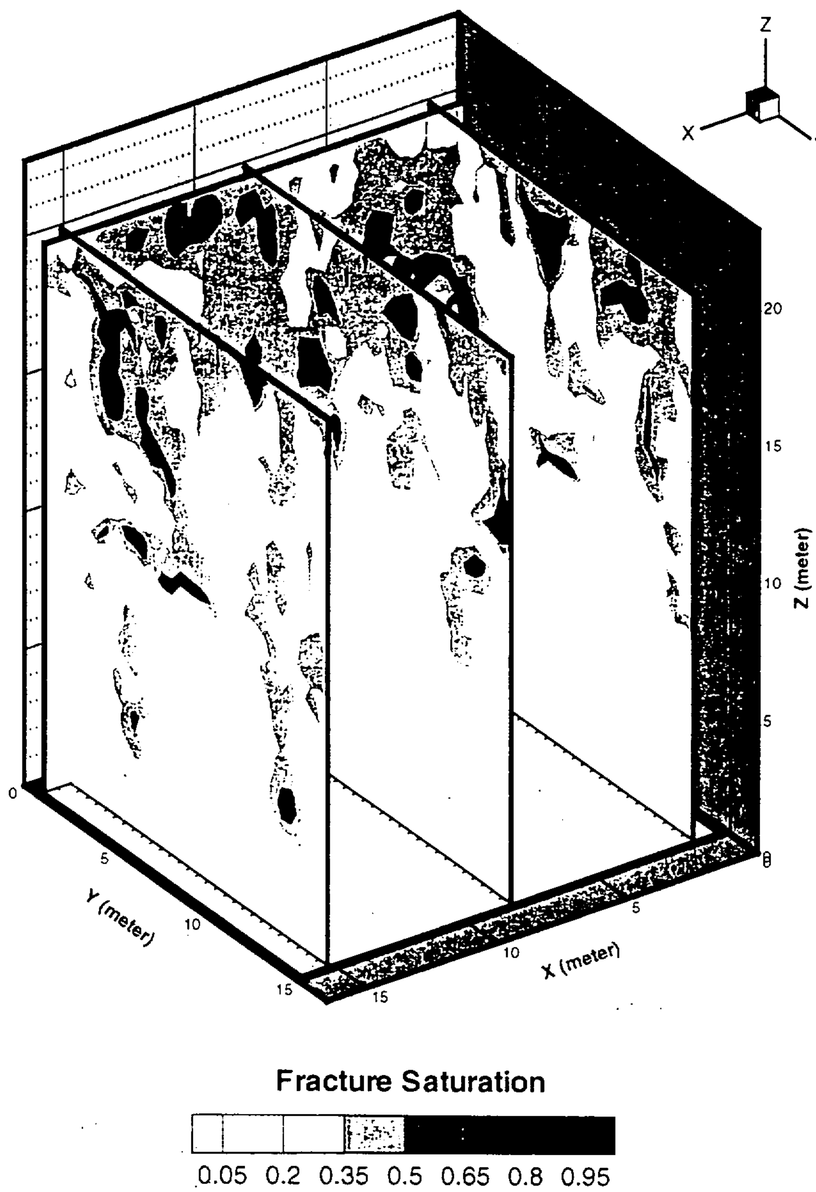

Figure 2-74. Saturation contours in fracture continuum on three vertical planes along y-direction in part 1 of the 3-D block for Qp = 1,000 mm/yr and IF=100% at t=1 day.

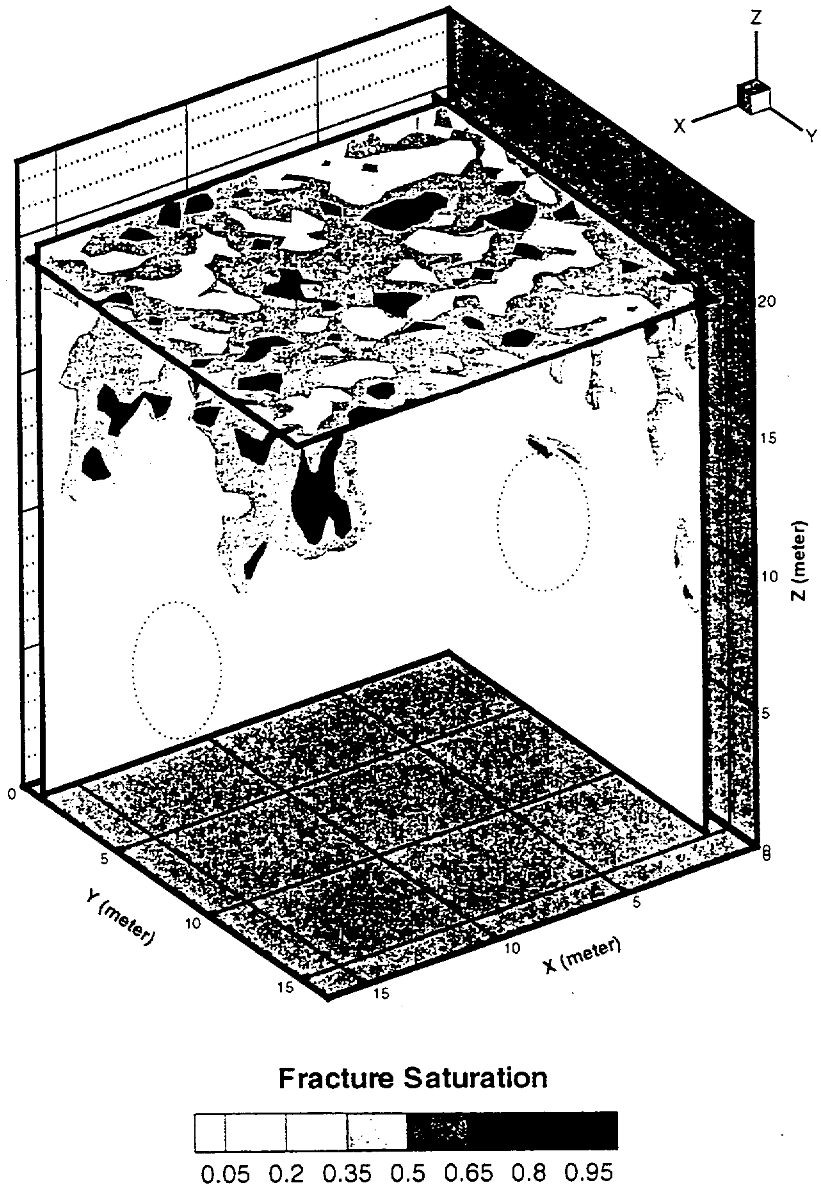

Figure 2-75a. Saturation contours in fracture continuum on horizontal plane chosen close to the top boundary in part 1 of the 3-D block for Qp=1,000 mm/yr and IF=100% at t=1 day.

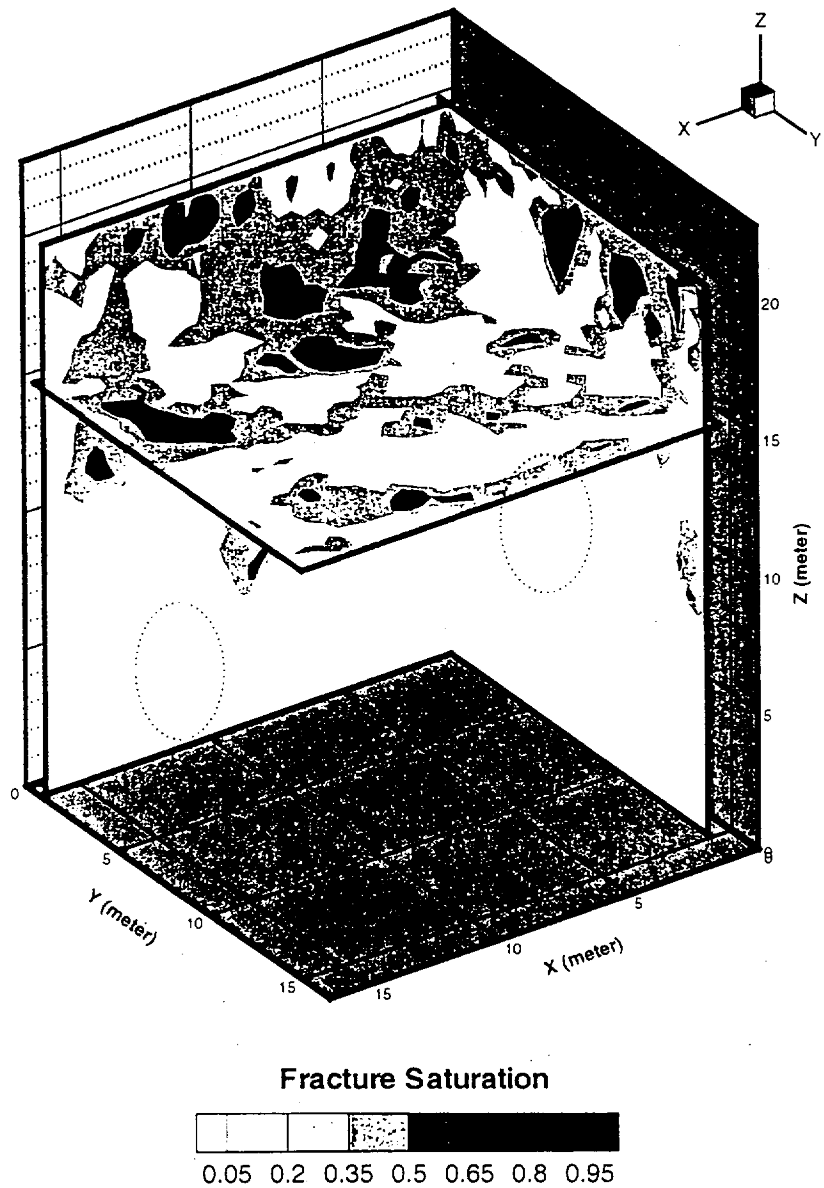

Figure 2-75b. Saturation contours in fracture continuum on horizontal plane chosen between the top boundary and the drift in part 1 of the 3-D block for Qp=1,000 mm/yr and IF=100% at t=1 day.

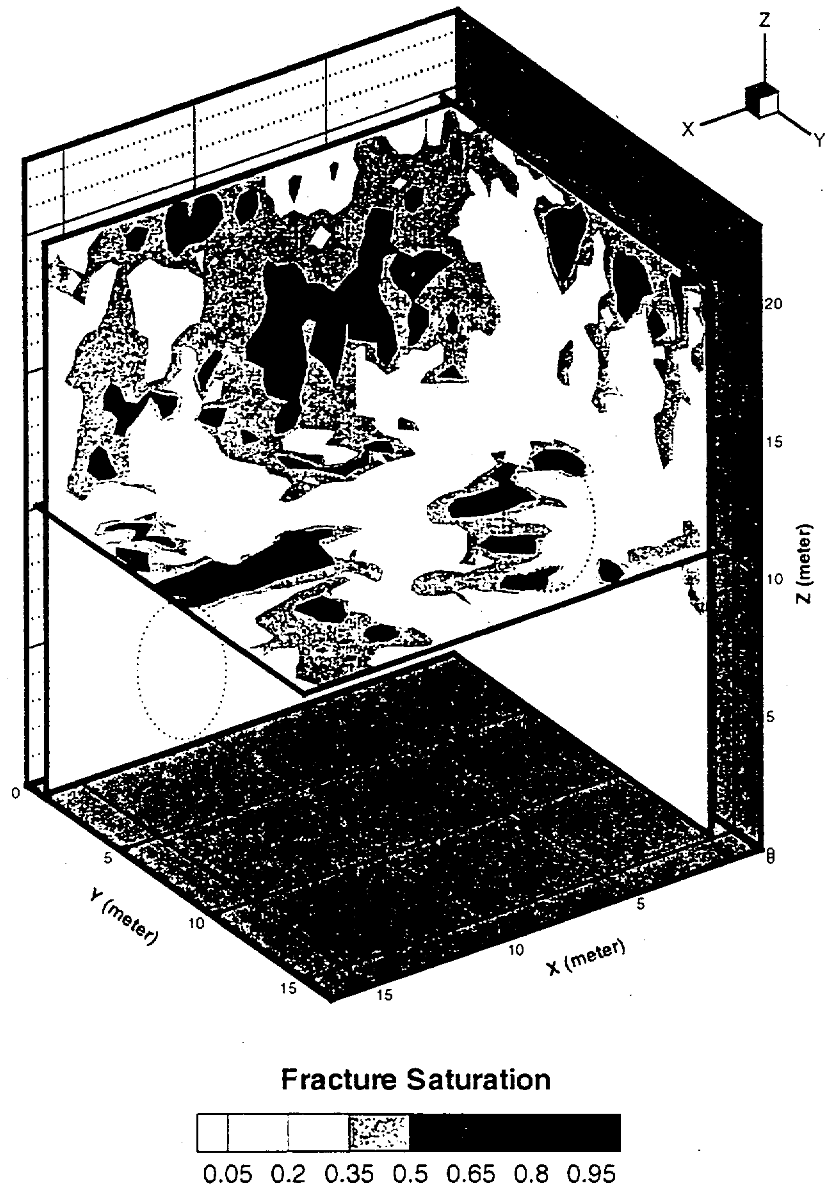

Figure 2-75c. Saturation contours in the fracture continuum on horizontal plane chosen just above the drift in part 1 of the 3-D block for Qp=1,000 mm/yr and IF=100% at t=1day.

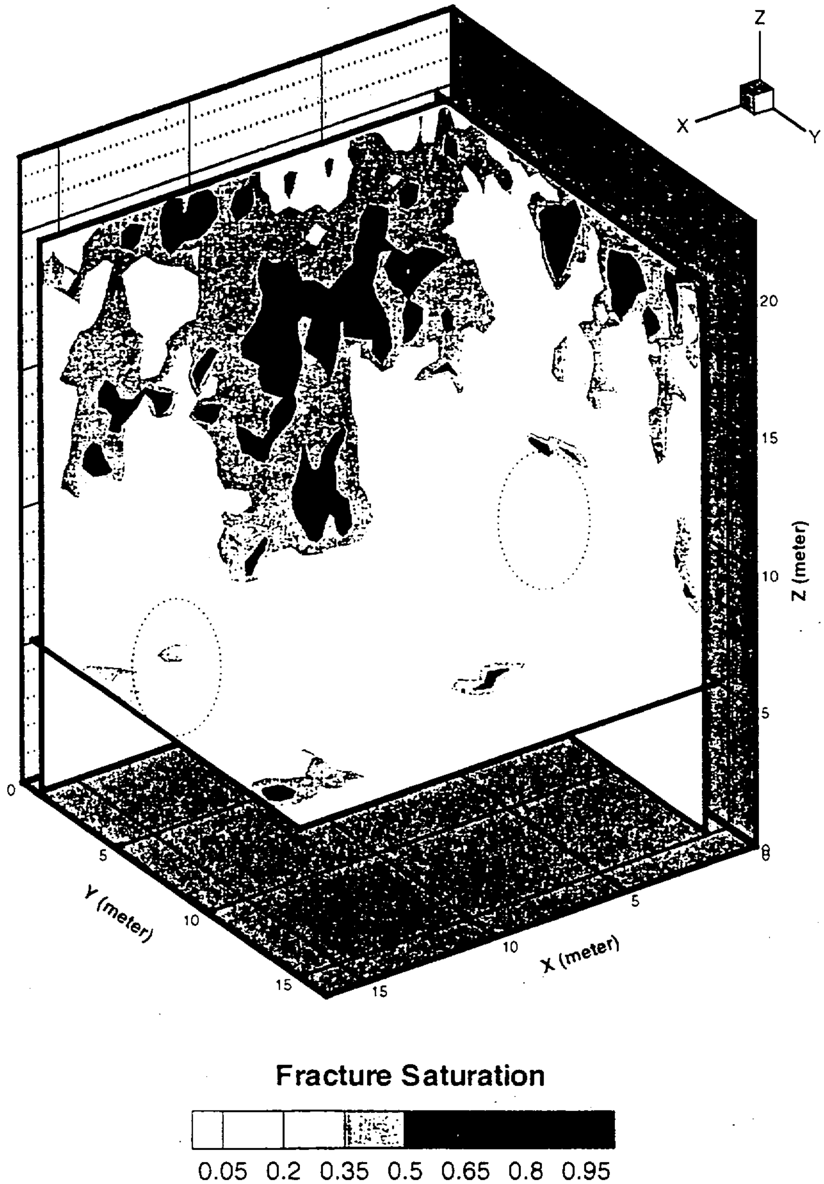

Figure 2-75d. Saturation contours in the fracture continuum on horizontal plane chosen just below the drift in part 1 of the 3-D block for Qp=1,000 mm/yr and IF=100% at t=1day.

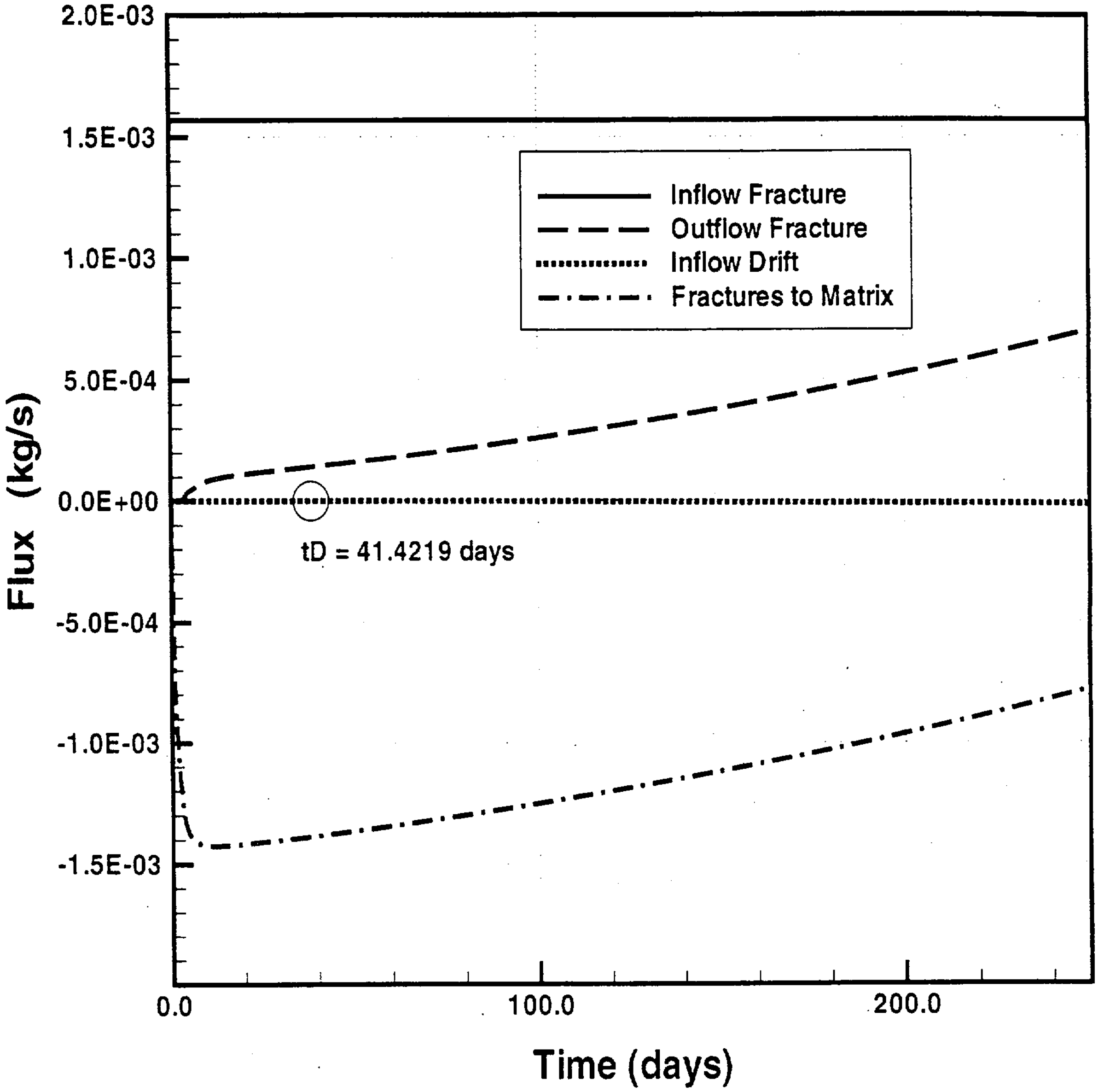

Figure 2-76a. Q_{Top}, Q_{Bottom}, Q_D, and Q_{FM} as a function of time for part 3 of the 3-D block for Q_p = 200 mm/yr and IF = 100%.

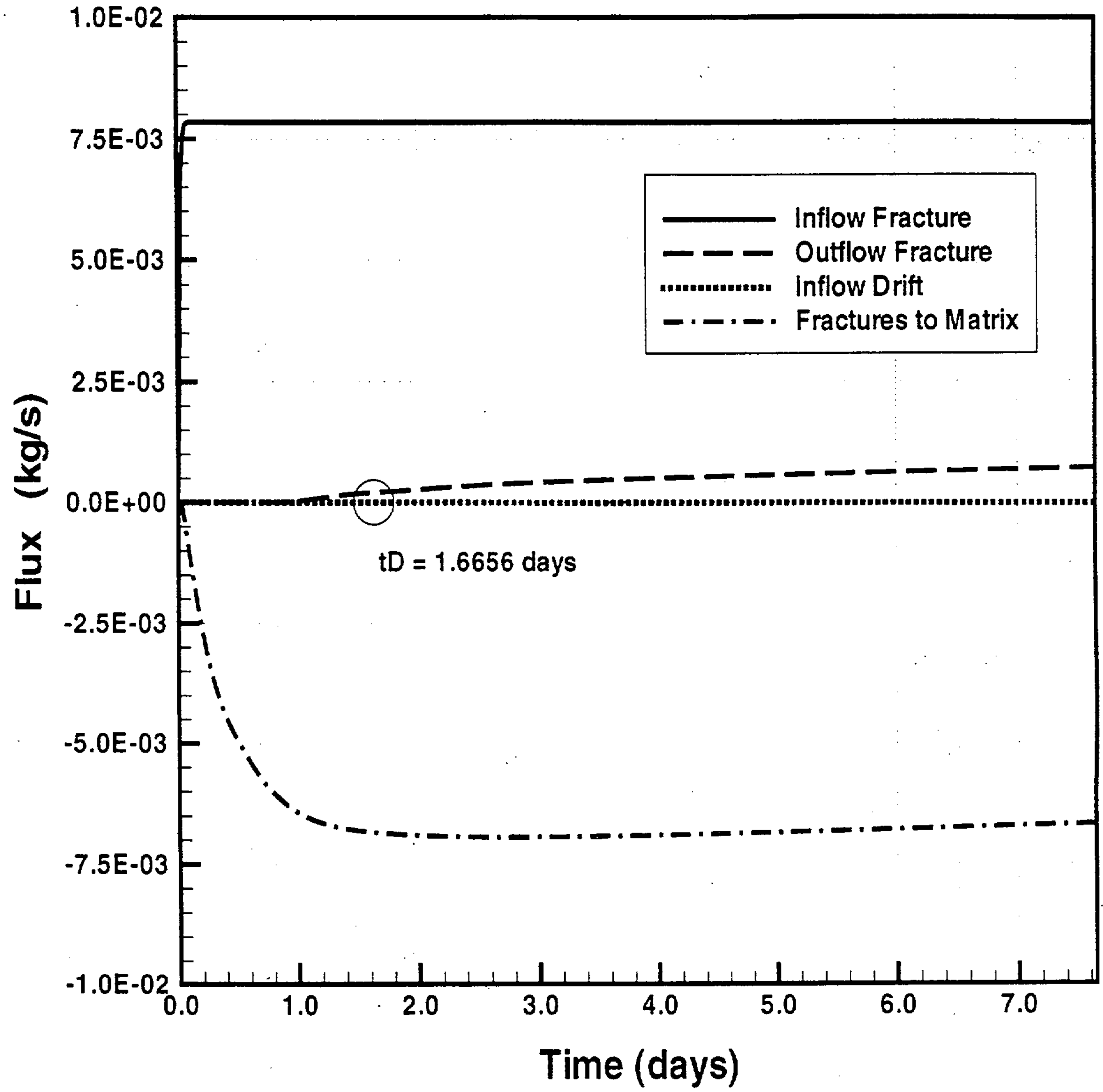

Figure 2-76b. Q_{Top}, Q_{Bottom}, Q_D, and Q_{FM} as a function of time for part 3 of the 3-D block for Q_p = 1000 mm/yr and IF = 100%.

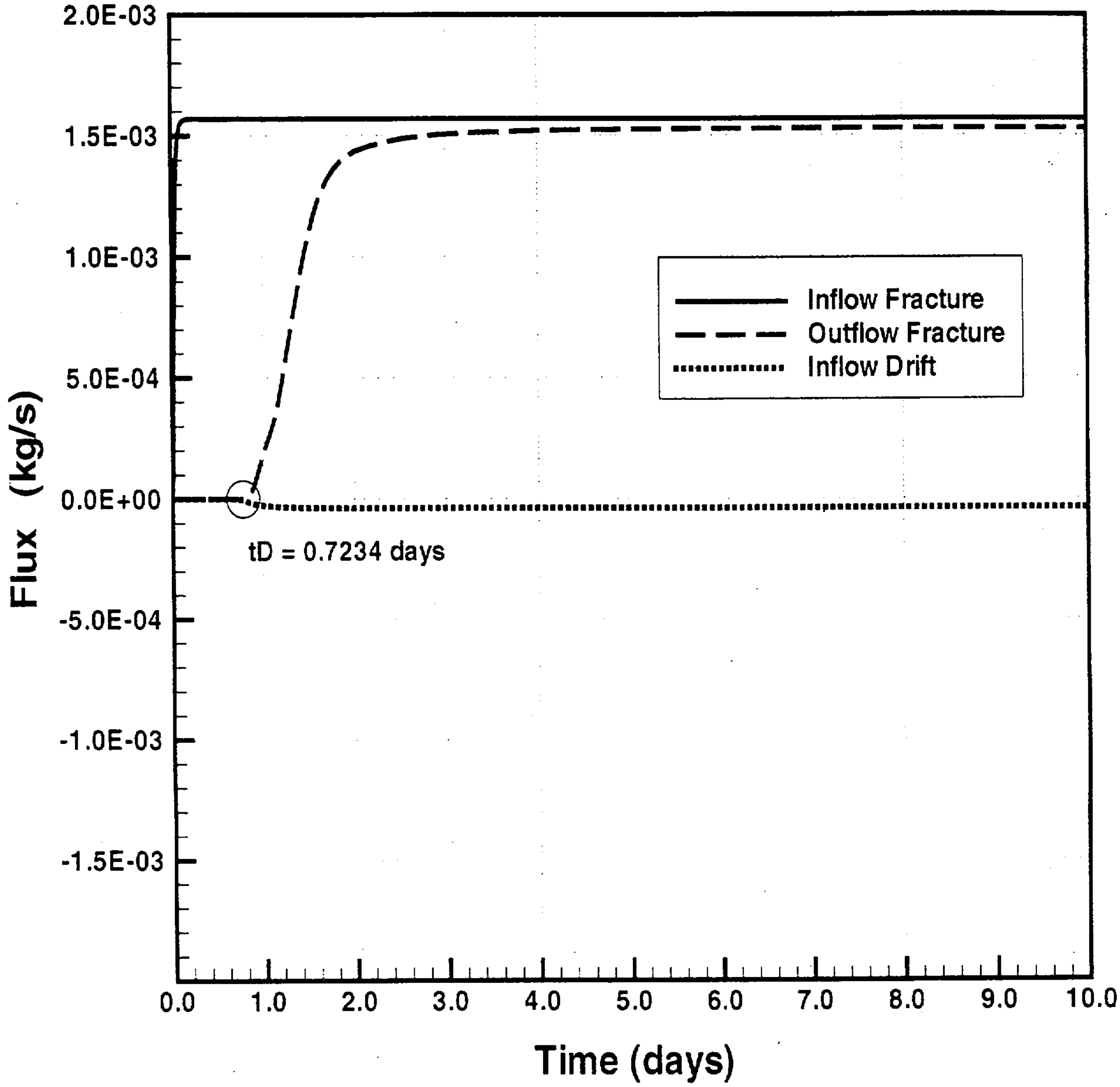

Figure 2-77a. Q_{Top}, Q_{Bottom}, Q_D, and Q_{FM} as a function of time for part 3 of the 3-D block for Q_p = 200 mm/yr and IF = 0%.

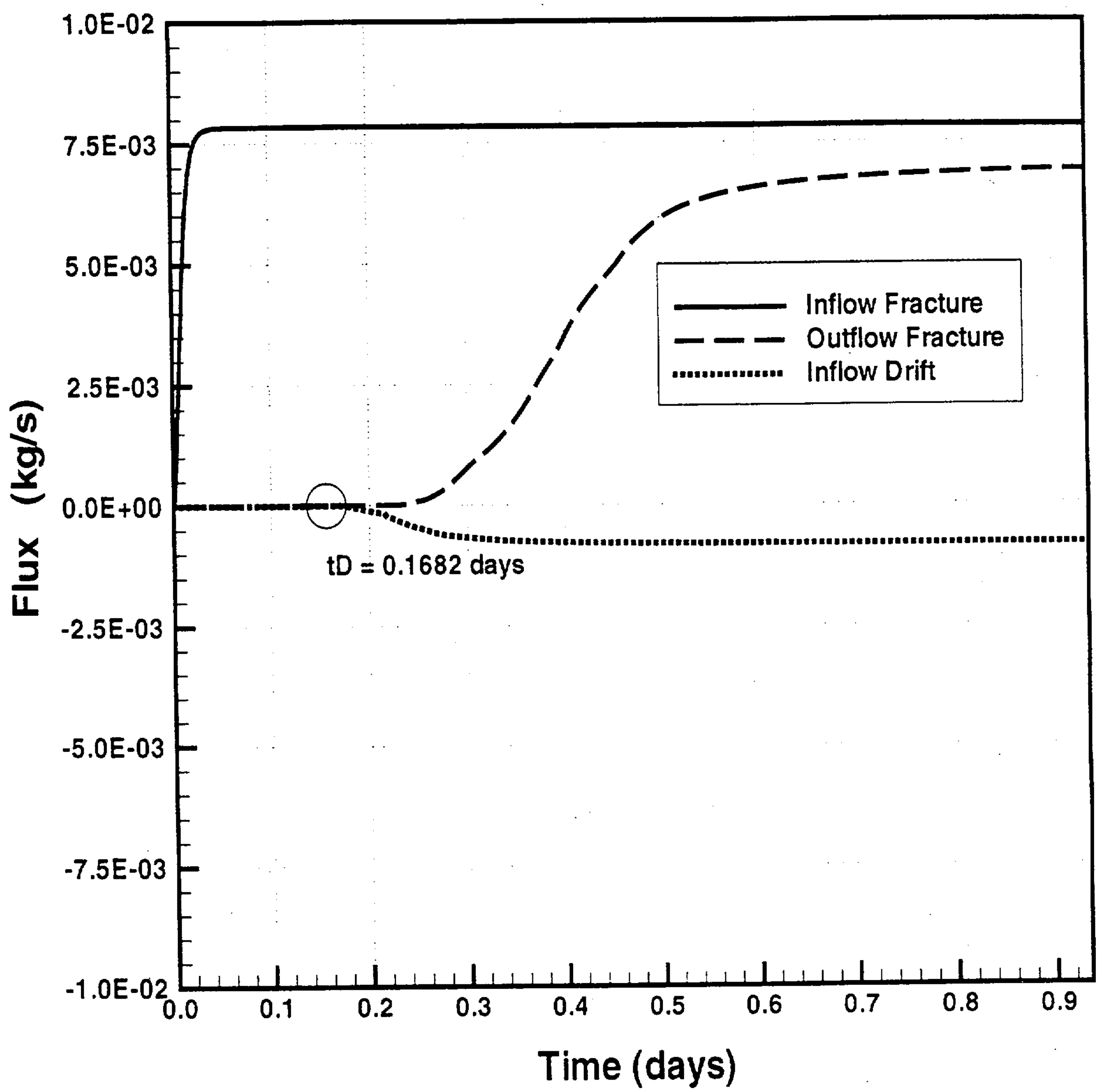

Figure 2-77b. Q_{Top}, Q_{Bottom}, Q_D, and Q_{FM} as a function of time for part 3 of the 3-D block for Q_p = 1000 mm/yr and IF = 0%.

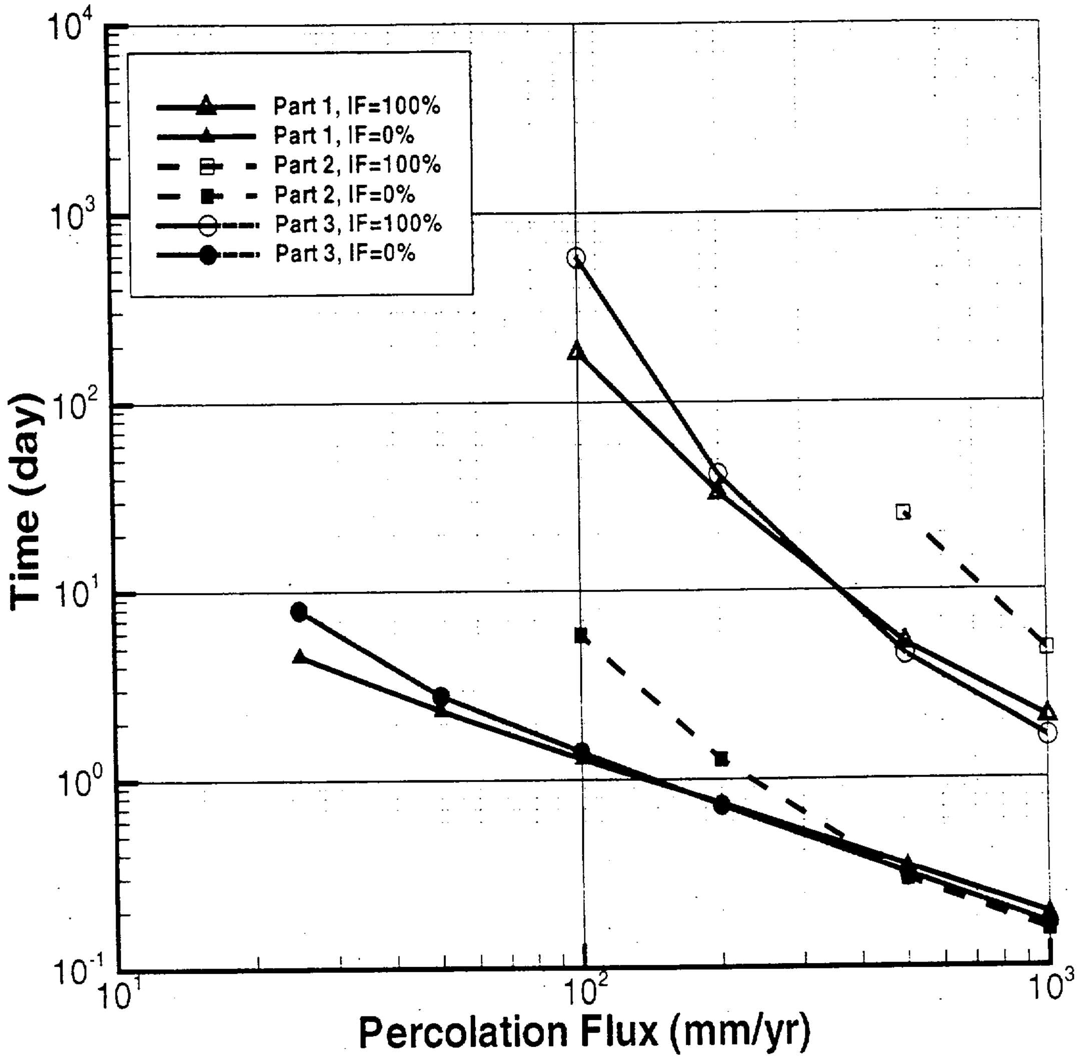

Figure 2-78. Time of seepage into drift as a function of Q_p for parts 1, 2, and 3 of the 3-D block.

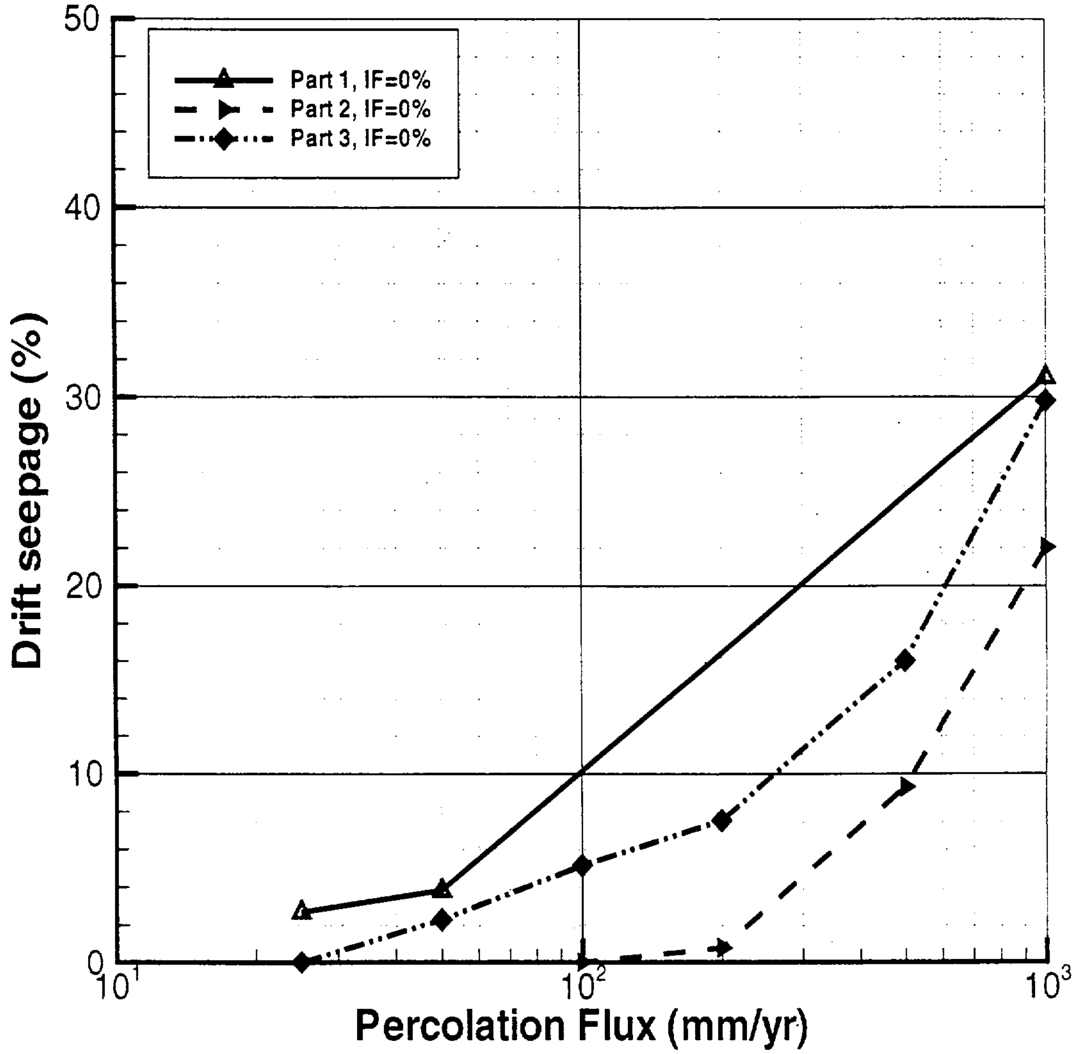

Figure 2-79. Rate of seepage into drift as a function of Q_p for parts 1, 2, and 3 of the 3-D block. Note that because there are computational limitations, no steady-state solution was obtained for part 1 with percolation fluxes of 100 mm/yr, 200 mm/yr and 500 mm/yr.

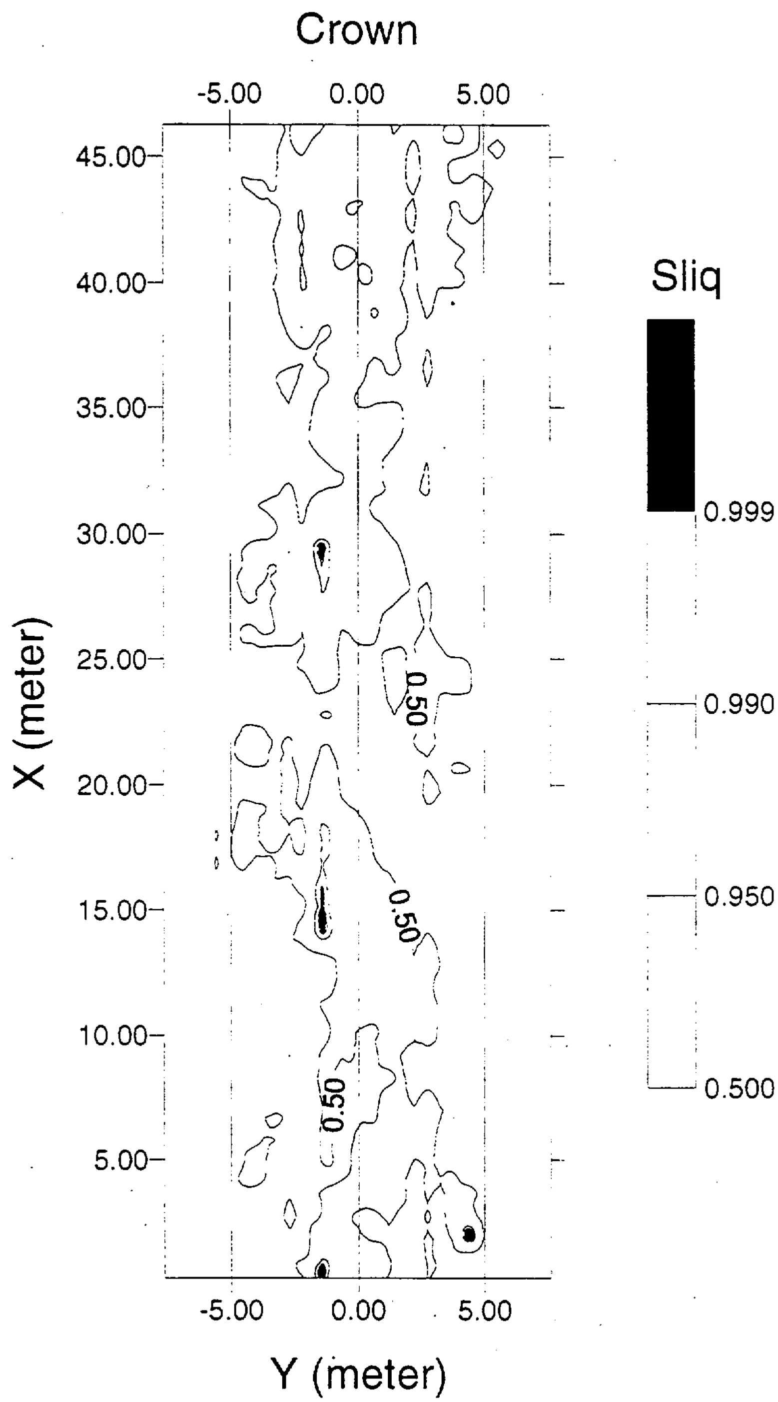

Figure 2-80. Saturation contours in fracture continuum along drift wall for Q_p = 1,000 mm/yr and IF = 100% at t = 5.0 days.

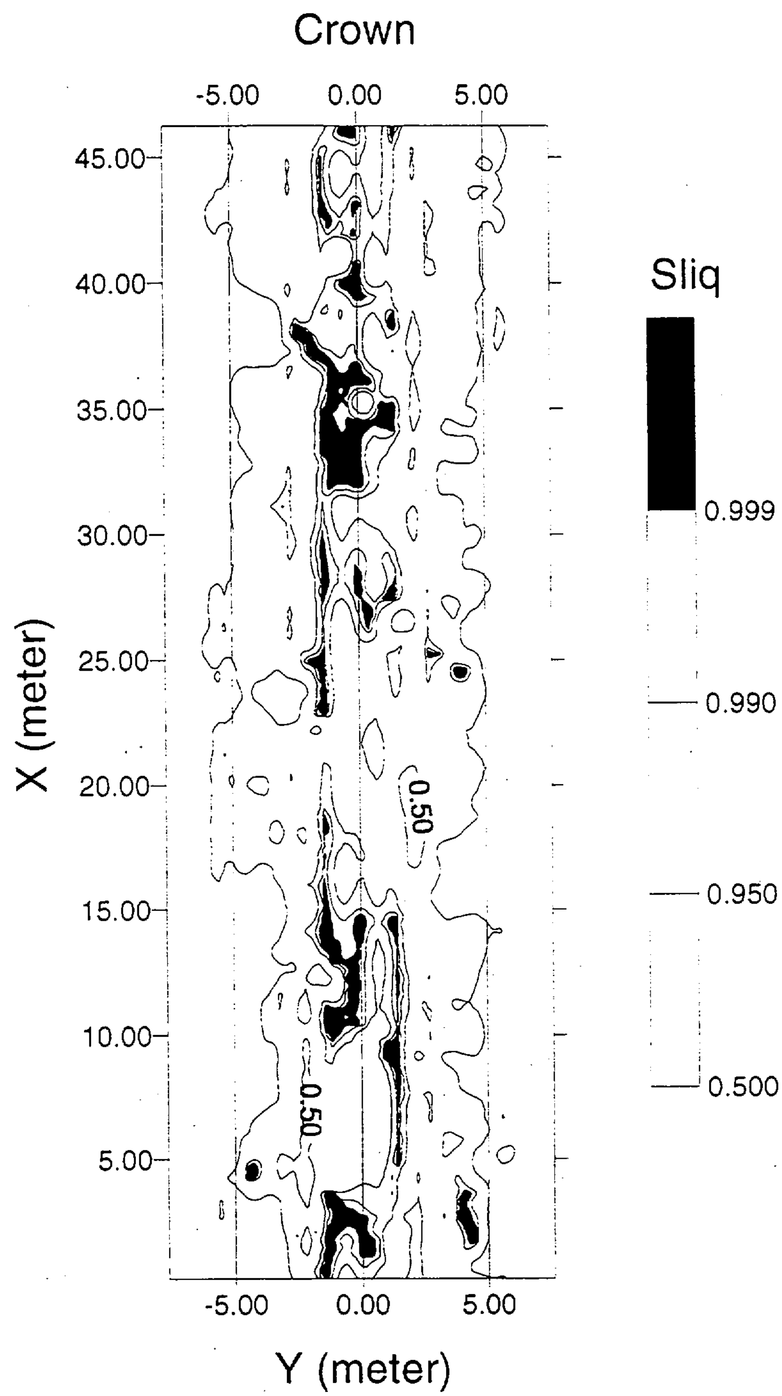

Figure 2-81. Saturation contours in fracture continuum along drift wall for Q_p = 1,000 mm/yr and IF = 0% at t = 0.42 days.

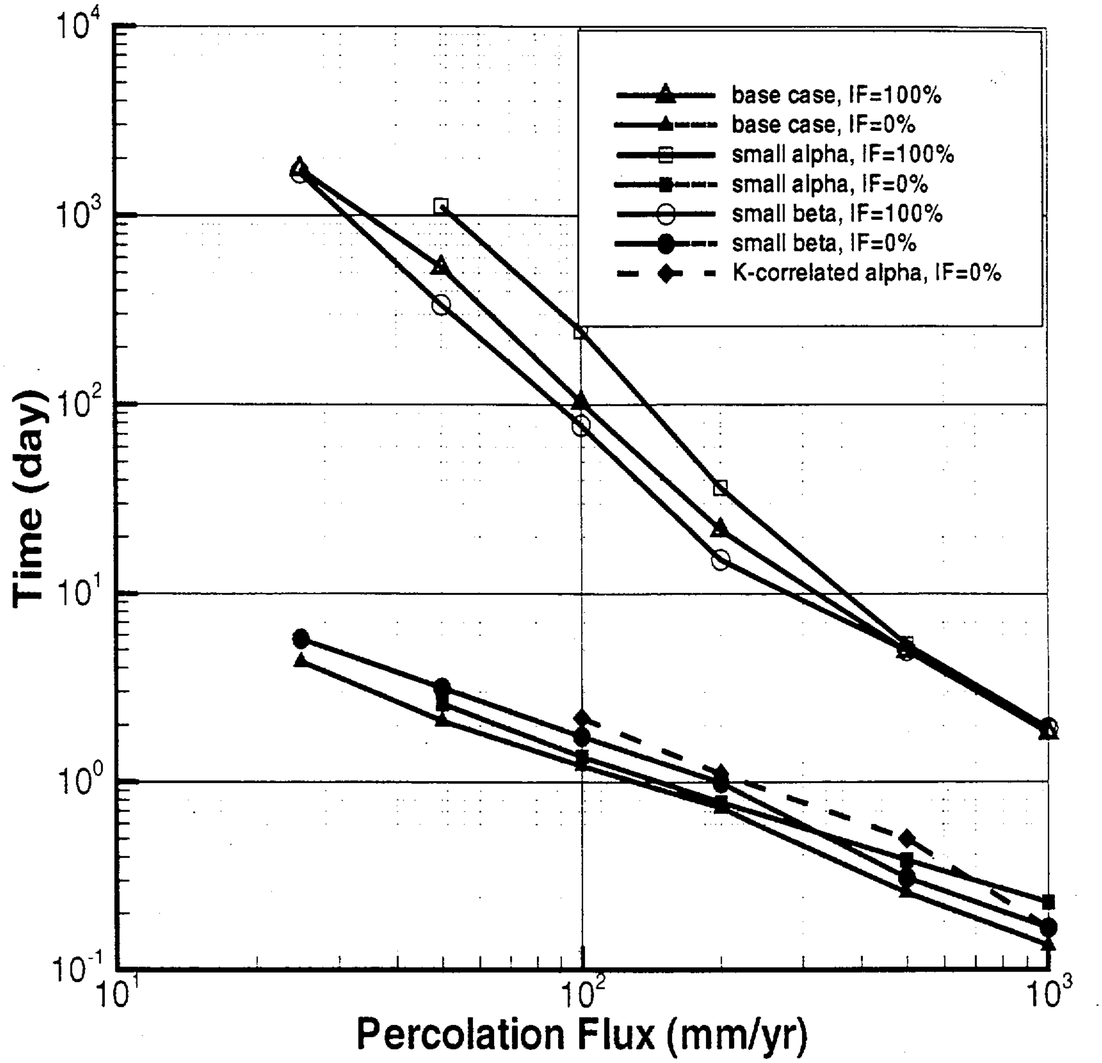

Figure 2-82. Time of seepage into drift as a function of Q_p showing sensitivity to fracture van Genuchten α and β for slice 1 of the 3-D block.

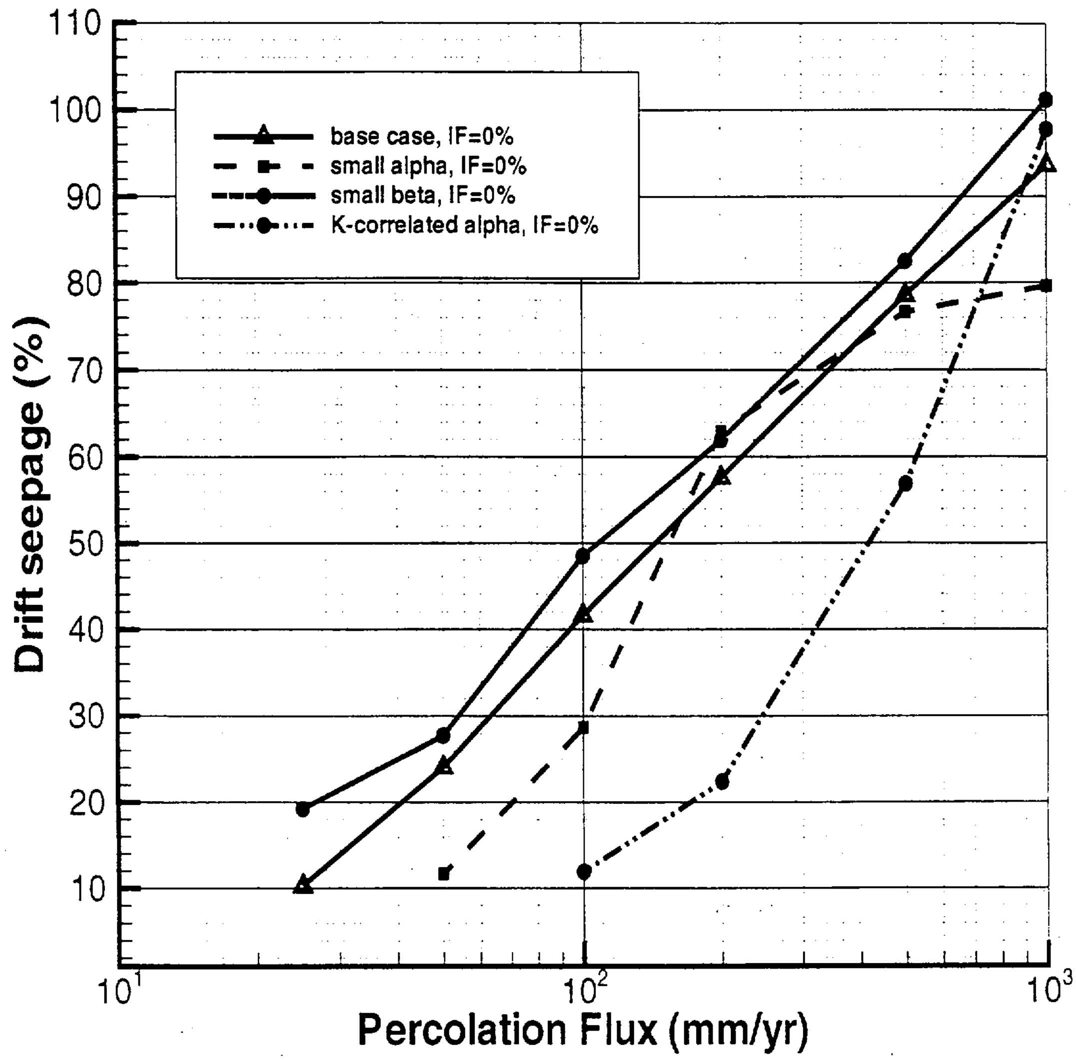

Figure 2-83. Rate of seepage into drift as a function of Q_p showing sensitivity to fracture van Genuchten α and β for slice 1 of the 3-D block.

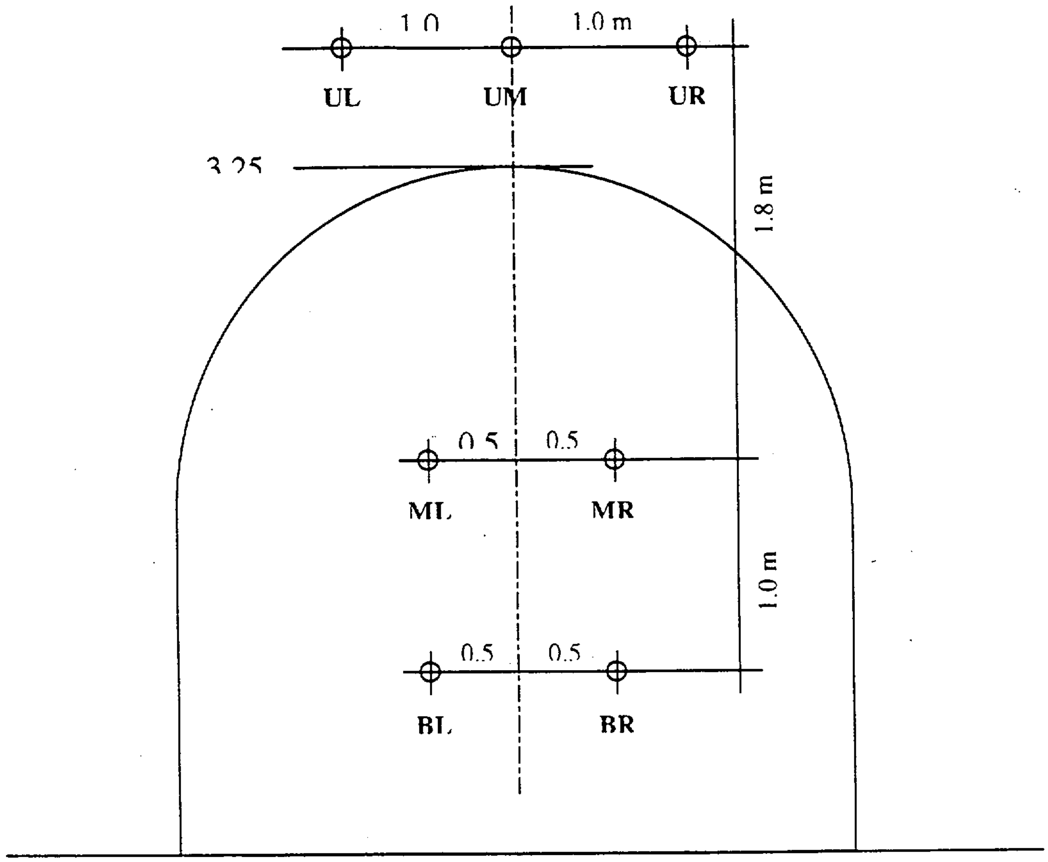

Figure 2-84. End view of boreholes on the wall of ESF Main Drift before the niche at CS 3560 was excavated.